Three-Dimensional Nonlinear Finite Element Modeling of Mammalian Cornea to Study Mechanics of Spiraling

TALISA MOHAMMAD NEJAD
B.S., Sharif University of Technology, 2009

THESIS

Submitted as partial fulfillment of the requirements

for the degree of Doctor of Philosophy in Civil Engineering

in the Graduate College of the

University of Illinois at Chicago, 2014

Chicago, Illinois

Defense Committee:

Craig D. Foster, Chair and Advisor

Didem Ozevin

Eduard Karpov

Thomas Royston, Mechanical Engineering and Bioengineering

Philip M. Iannaccone, Northwestern University's Feinberg School of Medicine

Acknowledgements

I owe my deepest gratitude to my advisor, Professor Craig Foster, for being such a tremendous advisor and mentor for me. He provided me with every bit of guidance, assistance, advice, and encouragement from the very beginning of my Ph.D. career. His joy and enthusiasm for research was definitely motivational for me. I am also very thankful for the excellent example he has provided as a researcher and as a person.

I would also like to express my great gratitude to my committee members, Professors Eduard Karpov, Didem Ozevin, Thomas Royston, and Phillip Iannaconne for their time and valuable feedback.

I am greatly thankful to our collaborators at Children's Hospital of Chicago Research Center, Professor Phillip Iannaconne, Steve Iannaconne, and Dr. Jerry Rhee for our fruitful collaboration.

Many thanks go to my colleagues, David Weed, Ahmed Alghandour, Hosein Motamedi, Milad Parvaneh, Dipika Gongal, and Adam Tenant for providing a supportive and friendly research environment. I would like to thank David Weed, who was always willing to help.

I express my kindest thanks to my close friends and relatives. I am so lucky to have such wonderful people in my life. Special thanks go to Farzan Kazemifar for his continuous support, help, and optimistic attitude.

Last but not least, I would like to deeply thank my family members for the never-ending love and encouragement I have received over the years. I am specially greatly indebted to my amazing parents, who constantly encouraged and supported me at every stage of my personal

and academic life. Without them, I would not have been able to achieve this. Finally, I would like to dedicate this dissertation to my wonderful parents.

Table of Contents

List of Figures

List of Tables

Summary

The cornea is a transparent tissue in front of the eye that refracts the light and makes vision possible. A slight change in the geometry of cornea remarkably affects the optical power. Biomechanical study of cornea can reveal much about its performance and function. In vivo and in vitro studies have been conducted to investigate the mechanics of cornea and to determine its characteristics. Numerical techniques such as the finite element method (FEM) have been extensively implemented as effective and non-invasive methods for analyzing corneal mechanics and possible disorders. The focus of this dissertation is to use finite element analysis for studying biomechanical behavior of the cornea. This work also allows reviewing different applications of FEM in studying corneal diseases, surgery predictions, impact simulations and clinical applications.

The cornea is nearly incompressible and can undergo large deformation with very little change in volume. Nearly incompressible materials require special treatment in finite element analysis to relieve volumetric locking, an inaccuracy that arises from the incompressibility constraints. Of the several methods to relieve locking, the $\bar{\boldsymbol{B}}$ method is popular as no extra variables or degrees of freedom need to be added. However, the literature is incomplete in the details of the $\bar{\boldsymbol{B}}$ method for large deformations. In the large deformation regime, the incompressibility is treated by using an averaged value of the volumetric part of the deformation gradient, and hence is often termed the $\bar{\boldsymbol{F}}$ approach. In this dissertation, an $\bar{\boldsymbol{F}}$ method is presented to treat volumetric locking in the large deformation regime. A framework for relating the choice of $\bar{\boldsymbol{F}}$ to the resulting $\bar{\boldsymbol{B}}$ is developed and stiffness matrices are proposed.

In some mammalian corneas such as mice and rats, the epithelial cells assort themselves into patterns that resemble spirals [1], [2]. The patterned arrangement of the corneal epithelial cells implies existence of some global processes or forces. However, a definitive explanation of the cause of these spiral patterns has not been determined. Studying the generation of these patterns is important as it may lead to greater understanding of corneal development and possible disorders. We propose here that the stresses and strains on the cornea surface facilitate sliding of epithelial cells into spiral patterns. In this dissertation, a framework for explaining the generation of this poorly understood phenomenon is presented.

To this end, a finite element computer code is developed to perform three-dimensional and large deformation modeling of mammalian cornea. The cornea model includes the effect of preferentially oriented and dispersed collagen fibrils embedded in nearly incompressible matrix. The deformation, stresses and strain distribution in the cornea subjected to pressure (intraocular pressure) is investigated. An algorithm is devised to track the pathlines of critical strain directions that tend to form spiral pattern. These patterns are finally matched with logarithmic spirals obtained from confocal images of the rat cornea. We conclude that the mechanical behavior of the cornea may cause the observed spiral patterns.

1 Introduction

1.1 Background

The eye helps us process a great deal of information from the outside world to the human and ocular disorders can greatly affect human life. Therefore, studying the components of the eye and their mechanical behavior has long been an issue of interest.

The cornea is the transparent avascular tissue in front of the eye that acts like a barrier to the eye and protects its front part from external injuries and inflammations. The transparency of the cornea results from many factors, among which its cellular components have the greatest effect. Figure 1 illustrates an x-ray image of the cross section of the mouse cornea.

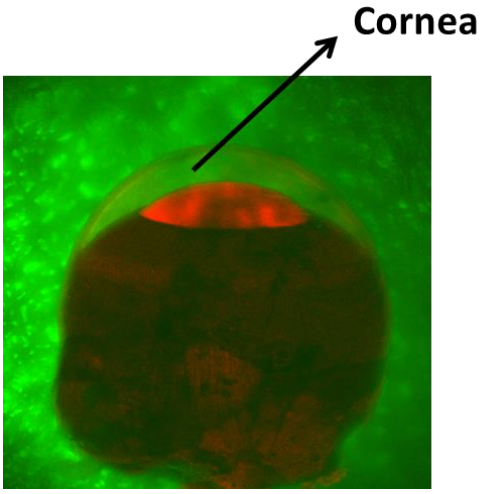

Figure 1 – It depicts an x-ray image of the cross section of the mouse eye. The illustrated mouse cornea has a thickness of 300 microns at the apex and gradually decreases toward the edge. There is a liquid behind the cornea (aqueous humor) that applies pressure to the corneal inner surface.

The cornea in many mammals (including human, mice and rats) consists of five recognized layers. Three of the layers are thicker (epithelium, stroma, endothelium) and two other layers are interfaces (Bowman's membrane, Descemet's membrane). Figure 2 depicts different layers of the cornea.

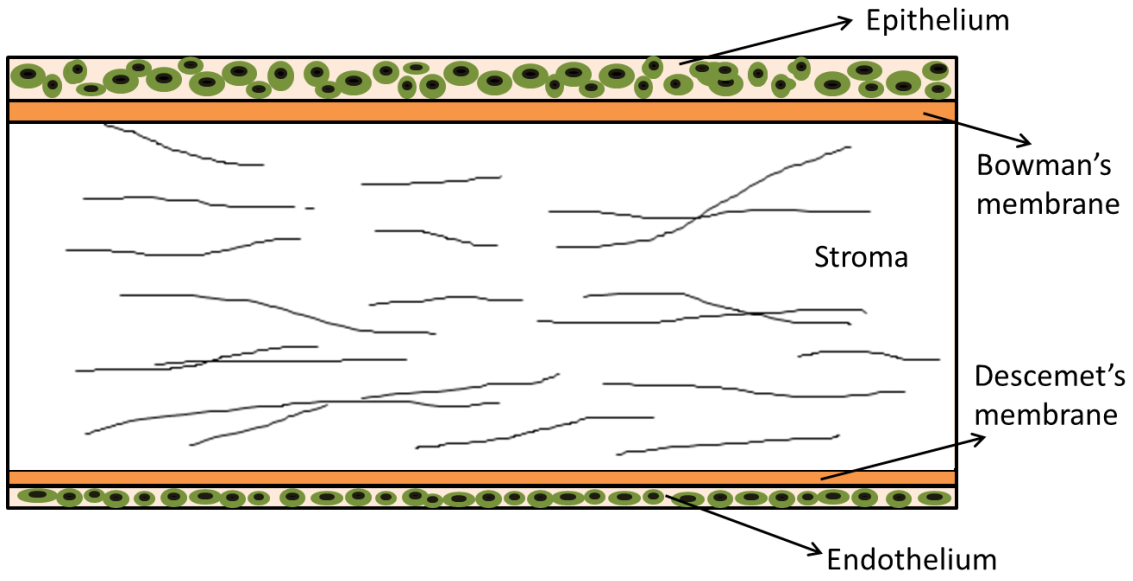

Figure 2 – The cornea in many mammals consists of five layers that from anterior to posterior are the epithelium, Bowman's membrane, stroma, Descemet's membrane and endothelium. The stroma is the thickest and stiffest layer that is composed of collagen fibers embedded in nearly incompressible matrix.

The epithelium is the outermost layer in the cornea that is covered with tear. The epithelium consists of cells that constantly reproduce and regenerate themselves. The epithelial cells, as well as the endothelial cells play role in maintaining smooth and clear optical system [3]. The epithelium lies on Bowman's layer which is a basement membrane that is responsible for adhesion of the epithelium to the anterior corneal stroma.

The stroma is the thickest layer in the cornea, and contributes most of the strength and stiffness to the cornea. It is composed of collagen fibrils that are embedded in viscoelastic matrix. The matrix is mainly composed of water and the mechanical response of the matrix is considered to be nearly incompressible. The fibrils are arranged in parallel bundles called fibers that form parallel layers called lamellae. The stromal collagen fibrils are flexible and have remarkably high tensile strength. They are distributed in preferred and dispersed orientations in the stroma. The density and orientation of collagen fibrils in the stroma influence the biomechanical behavior of the cornea, and hence studying arrangement of collagen is important [4]. In many mammals, collagen fibrils are oriented circumferentially (parallel to the edge of the cornea) in the area around the edge of the cornea. The preferred orientation of fibers is weaker in the central zone of the cornea and varies among mammalian species. For instance, collagen fibrils are oriented along the horizontal and vertical directions in the human cornea. X-ray patterns reveal vertical predominant directions for horse cornea, while showing circumferential preferred orientations in pig and rabbit, and horizontal directions in the mouse cornea [4], [5].

The endothelium is the innermost layer of the cornea that consists of endothelial cells. The density and topography of these cells continuously change throughout life. The endothelial cells keep the cornea hydrated and transparent. The transparency of the cornea is critical for its correct function. The endothelial cells have a unique function that allows pumping of fluids from the stroma back to the interior of the eye [6].

The Bowman's membrane that has a smooth anterior surface is between the epithelial basement membrane and the underlying stroma layer [7]. The layer does not regenerate and is composed of different types of collagen in an extracellular matrix. Descemet's membrane is the layer between the stroma and endothelium and is also composed of collagen.

Biomechanical study of the cornea can reveal much about its performance and function. Investigating biomechanical properties of corneal tissue are of increasing interest in disciplines such as refractive surgery. In vivo and in vitro studies have been conducted to investigate the mechanics of cornea and to determine its characteristics. In some cases, the tissue is not amenable to direct investigations, suggesting computational modeling as the preferred tool for investigating the biomechanical behavior. Numerical techniques such as the finite element method (FEM) have been extensively implemented as effective and non-invasive methods for analyzing corneal mechanics and possible disorders. The finite element method is an approximate technique for obtaining solutions for partial differential equations. It is a very useful method in solving problems involving complex material properties and irregular geometries.

In this work, the application of finite element analysis (FEA) in investigating the mechanical behavior of the cornea is studied. It is worth mentioning that finite element method can also be applied to study a wide variety of problems, for instance, thermal, electrical, ionic transport and other physical responses.

1.2 Motivation and Objective

During the generation of an organ, stem cells assort themselves into patterns as a result of cell division, cell movement and cell death [8]. These processes operate in a typical reproducible and conserved manner [9]. If two or more genetically distinct population of cells comprise the tissue, the resulting distribution of cells can be visually distinguished.

In the cornea, the allocation of epithelial cells is followed by an assortment of cells such that a distinctive pinwheel pattern is visualized in some mammal such as rats and mice [1], [2]. Also, the edges of patches of cells having similar lineages tend to form characteristic spiral

curves. These patterns have been detected on the anterior surface of the cornea under both normal and diseased conditions [10].

The absence of spiral distribution correlates with human eye disorders and abnormal cornea structure and function [2]. Hence, the possibility that biomaterial properties contribute to normal epithelial cell distribution may lead to a greater understanding of corneal diseases.

Studying the generation of spiral patterns on the epithelium is significant as it can give insight into the development of the cornea and possible disorders. Our motivation in this work is to investigate and explain this natural phenomenon that has not yet been fully understood.

The patterned assortment of the corneal epithelial cells suggests existence of some global processes or forces. While some models have been proposed to explain formation of spiral patterns, none have been able to completely explain this phenomenon. We assume here that the stresses and strains on the cornea surface cause special assortment of epithelial cells into spiral patterns. In this regard, we create a computer-based numerical simulation model for the rat cornea, allowing determination of deformation, stress and strain on the cornea surface.

In this work, a large deformation model of the cornea including the stiffening effect of collagen fibrils in a hydrated matrix is embedded in a finite element code. A constitutive model for the finite deformation and anisotropic behavior of the cornea is proposed that includes the oriented and dispersed distribution of collagen fibers in nearly incompressible matrix. The cornea is subjected to intraocular pressure and the stress and strain distribution on the cornea surface is examined. An algorithm is devised to track the directions of critical strains to drive the development of spiral patterns. The pathline tracking procedure results in spiral-like curves that are eventually fitted with logarithmic spirals with determined pitch angles. These angles are finally compared to the pitch angles of the logarithmic spirals observed on the rat cornea surface.

1.3 Organization of the Dissertation

The remainder of the dissertation is organized as follows: Chapter 2 reviews the use of FEM in assessing corneal mechanical behavior. Section 2.1 discusses the modeling assumptions made in many finite element models of the cornea. The purpose of this section is to give modelers an understanding of the different assumptions that have been used, so that they may choose an appropriate model for their application of interest. Section 2.2 discusses different applications in cornea mechanics. Finite elements have been used to model the response of the cornea surgery, disease and treatments such as collagen cross-linking, trauma, and basic research applications. Section 2.3 summarizes the review section and makes some suggestions on the future of such modeling in the practice of ophthalmology and eye research.

Chapter 3 explains volumetric locking in nearly incompressible materials and proposes an $\bar{\boldsymbol{F}}$ method as a solution to treat the nonlinear incompressibility constraints. Nearly incompressible materials such as the cornea require special treatment in a finite element context. While solutions exist to this issue, the literature is incomplete in the details of the $\bar{\boldsymbol{B}}$ method for large deformations. A trilinear hexahedra with integral-averaged volumes for nearly incompressible nonlinear deformation is developed. The choice of averaged $\bar{\boldsymbol{F}}$ is related to the resulting $\bar{\boldsymbol{B}}$ and stiffness matrices are proposed. Section 3.1 discusses integral averages for $\bar{\boldsymbol{F}}$**,** including two of several possible choices. Section 3.2 derives the $\bar{\boldsymbol{B}}$ formulation consistent with choice of $\bar{\boldsymbol{B}}$. The stiffness matrix is presented in Section 3.3, though the full derivation is relegated to the Appendix (Section 7). This section is followed by numerical examples and some calculations in Section 3.4.

In Chapter 4, a finite deformation model for the rat cornea is developed to explain special assortment of epithelial cell into spiral patterns. Section 4.1 provides background to the problem

under investigation. In Section 4.2 the generation of spiral patterns on the surface of the rat cornea is discussed. In Section 4.3, an anisotropic and large strain finite element model of the rat cornea is developed. This includes creating the 3-dimensional geometric model of the rat cornea and an overview of the restrictions applied on the cornea limbus. The section is followed by a review on the preferred orientation of collagen fibrils in some mammalian cornea as well as assumption of predominant fibril directions on the rat cornea. Also, a structural constitutive formulation including the stiffening effects of collagens in Neo-Hookean matrix is discussed. Section 4.4 focuses on the spiral post-processing which includes the determination of in-plain strains and developing an algorithm for tracking directions of critical strains. In Section 4.5, the numerical simulation results are compared to experimental observations. The dissertation is followed by a discussion on potential mechanical explanation for spiral formation in Section 4.6.

The dissertation is followed by a discussion and conclusion in Chapter 5, an Appendix on derivation of stiffness matrix for the proposed $\bar{\boldsymbol{B}}$ approach in Chapter 6 and finally list of references.

2 Review of Finite Element models of the Cornea

2.1 Introduction

The cornea is the transparent, anterior part of the eye, which refracts light onto the lens and is essential to vision. The curvature and thickness of the cornea play important role in focusing light to the lens, and hence are largely responsible for its optic power [11].

In humans and many other mammals, the cornea consists of five layers: the epithelium, Bowman's membrane, the stroma, Descemet's membrane and the endothelium [12]. Of the five layers, the middle layer, the stroma, makes up about 90% of the cornea thickness in humans and is the major layer contributing to the mechanical strength and stiffness of the cornea [13].

The stroma is a composite material consisting of matrix embedded with complex network of collagen fibers. The matrix is a viscoelastic and nearly incompressible material [12]. The collagen fibrils are bundled together to form fibers [14]. The fibers are stacked parallel to form layers called lamellae [15]. The stroma, in human cornea, consists of about 300 lamella at the center and about 500 at limbus [16]. The fibers act as reinforcement to the tissue and give it mechanical strength along their orientation. The arrangements of collagen fibrils are important to determining the mechanical strength of cornea. X-ray scatter intensity distribution data indicated two preferred directions of collagen orientation at the center of the cornea, Nasal-Temporal and Superior-Inferior [17], [18]. Near the limbus they tend to run in the circumferential direction [18]. Approximately two-thirds of the fibrils are preferentially oriented in the cornea, with the remaining third having more or less random orientation [19], [20]. This arrangement of the collagen fibrils results in anisotropy of the cornea material.

Biomechanical experiments on corneal tissue have been performed both in vitro and in vivo studies. Recently, the use of computational models based on finite element method has proven to be an effective way to study the cornea mechanics and diseases related to it (Pandolfi & Holzapfel 2008; Pinsky et al. 2005; Carvalho et al. 2009; Gefen et al. 2009). These models have been successful in predicting the pre-operative and post-operative response for eye surgery to treat myopia, hyperopia, astigmatism and keratoconus [15], [23]–[26].

The finite element method (FEM) is a numerical technique to obtain approximate solutions for partial differential equations involving physical, thermal, chemical or other phenomena. Generally these differential equations are impossible to solve analytically due to the complex geometries and properties of the materials. The approach for solving the equations is to simplify the form of the equation using simple interpolation functions and integrate the entire solution to obtain the final results. This method is very useful in solving problems involving complex material properties and irregular geometries.

To carry out a finite element analysis (FEA), a given body or system is divided into small units called elements. These elements are interconnected at points called nodes. The nodes and elements create a network referred as mesh. Each element is assigned specific material and structural properties and analyzed under certain boundary conditions. Boundary conditions can include forces, displacements, and temperatures. The analyzed solution of each element is assembled together to give the global response of the system.

The accuracy of this method, in general, depends upon the number of elements used for the analysis. The larger the number of the elements, the more precise the solution. However, over-refinement of the mesh leads to large computational time and memory use in the computer.

The element shape and type of elements used also play important role in the accuracy of the analysis.

The focus of this article will be the use of FEA for mechanical analysis of the cornea. We will review how this method has been applied to examine the cornea under different loads such as intraocular pressure, impact from a foreign object, or incisions. The method can also be used to examine how the shape is affected by changes in material properties such as during keratoconus. It is worth mentioning briefly, though, that the method can be applied to a wide variety of problems. It has been used to study thermal, electrical, ionic transport and other physical responses. Shafahi and Vafai [27] used thermal finite element model of eye to study its response to thermal disturbances. Papaioannou and Samaras [28] used rabbit eye model to simulate the temperature distribution and velocity field generated under exposure to millimeter wave radiation. Jo and Aksan [29] performed simulation of conductive keratoplasty, a thermal treatment for hyperopia and presbyopia, to predict thermal damage of the cornea tissue. Mandel et al. [6] used the three-dimensional cornea model exposed to electrical field to evaluate electrical properties of endothelial layer. Guimera et al. [30] also developed a non-invasive FEM to predict the electrical properties of endothelium and study variations in permeability of epithelium. Li and Pinsky [31] created multi-phasic mathematical model describing transport of ionic solution and ionic species in human cornea tissue. We refer the reader to those papers and references therein for further details on those topics of study.

The remainder of this Chapter is organized as follows: Section 2.2 discusses the modeling assumptions made in many finite element models of the cornea. The purpose of this section is to give modelers an understanding of the different assumptions that have been used, so that they may choose an appropriate model for their application of interest. Section 2.3 discusses different

applications in cornea mechanics. Finite elements have been used to model the response of the cornea to surgery, disease and treatments such as collagen cross-linking and trauma, as well as examining basic research applications. Section 2.4 summarizes the work and makes some suggestions on the future of such modeling in the practice of ophthalmology and eye research.

2.2 Modeling Basics

The structural model of the cornea can be approached by creating a continuum model or shell model. Continuum models explicitly model the geometry of the cornea in three dimensions, though two-dimensional approximations are sometimes used. Shell-based models use the theory of thin shell behavior to reduce the geometrical complexity. The modeled geometry is a surface, with the thickness of the shell as defined parameter. Tensile and bending loads on the shell create deformations in the shell in accordance with shell theory. While this reduces geometrical complexity and increases efficiency of the formulation, shell theory is difficult to extend to complex constitutive models. Anderson et al. [32] proposed a cornea model by using shell analysis to develop a non-linear finite element model to study the mechanical behavior of the cornea. Howland et al. [33], Pinsky and Datye [34], Li and Tighe [35] and Elsheikh and Wang [36] also based their model on this method.

2.2.1 Geometry

The structure of the human cornea has non-uniform curvature with variable thickness throughout [36]. It is thinner at the center and thickens towards the edge. Dubbelman et al. [37] recorded the cornea geometry for the internal and external surfaces of the human cornea using

Scheimpflug photography. Roy and Dupps [24] used the MRI to determine the geometric profile of eye.

Some early models of the cornea, e.g. [38], use a two-dimensional axisymmetric approximation of the cornea. This models the geometry as a surface of revolution, and is efficient compared to three-dimensional models. However, it cannot capture the subtle variations in the geometry of the cornea from a surface of revolution, anisotropies in the material that are prevalent, or any loads that occur off center, such as an impact or incision. Figure 3 illustrates common shell elements and 3-D elements used for FEA of cornea.

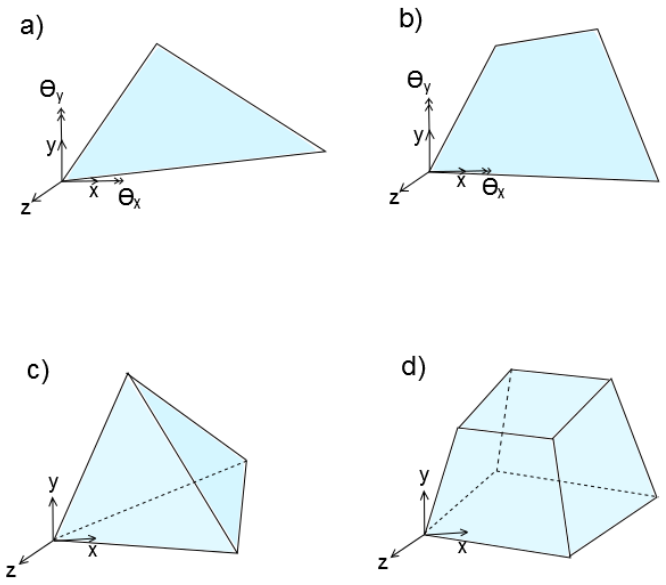

Figure 3 – Common shell and solid elements used for FEA of cornea. a) Triangle and b) quadrilateral are common shell elements. Each shell element node has 5 degrees of freedom (DOF) – 3 translational and 2 rotations (about two orthogonal axes on the shell surface). c) Tetrahedra and d) hexahedra are common 3-D elements. Each element node has 3 translational DOF.

Pandolfi and Holzapfel [12] used the cornea geometry data published by Dubbelman et al. [37] to create biconic interior and exterior surfaces for 3-D cornea model. Pandolfi and Manganiello [20] used ellipsoidal shape to define the anterior and posterior cornea surfaces. Nguyen et al. [39] and Nguyen and Boyce [40] also approximated the cornea surface to be ellipsoidal according to digital image correlation (DIC) measurements of cornea surface profile. Buzard [41] and Howland et al. [33] used axisymmetry to create their cornea model.

Salimi et al. [42] meshed the cornea model into triangular shell elements. For 3-D models hexahedral elements are more commonly used [12], [16], though tetrahedral elements may also be used. Linear tetrahedral and standard tri-linear hexahedral are known perform poorly for nearly incompressible materials such as soft tissues. Tri-linear hexahedral elements can be modified using techniques such as selective reduced integration [43], or higher-order elements may be employed. Figure 4 shows an example of FE mesh of the cornea.

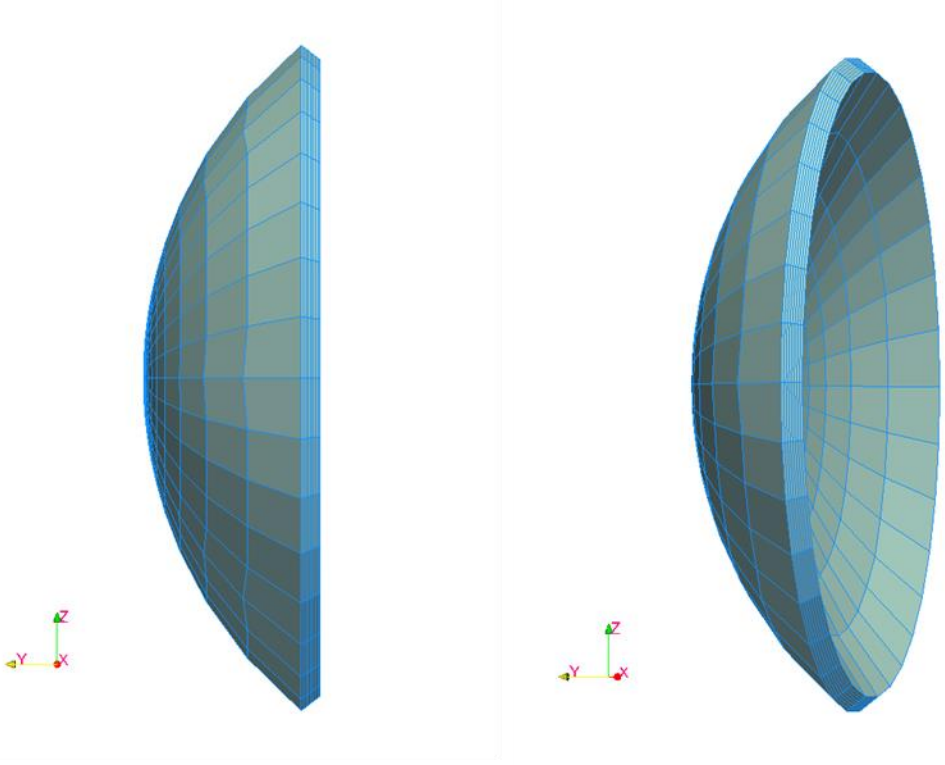

Figure 4 – An example of FE mesh of the cornea using hexahedral elements

2.2.2 Boundary Conditions

The viscous fluid filled inside the anterior chamber of the eye exerts pressure, called intra-ocular pressure (IOP), on the cornea. Under physiological conditions, the IOP inflates the cornea and gives it shape. A model developed for the cornea using entire eyeball allows appropriate realistic displacement at limbus. Uchio et al.[44], Amini and Barocas [45] modeled entire eye globe for the analysis. However, the whole eye model may not be efficient as it is highly time consuming and not economical for developing and analyzing.

Alastrue et al. [15] analyzed the cornea model with limbus constrained against displacement. Anderson et al. [32] compared the deformation pattern of the entire eye model to the rigid cornea-limbus boundary. They proposed an approximate boundary condition, with roller support at the edges inclined at 40˚ with respect to the horizontal axis, to represent the cornea-limbus behavior. The results obtained from their boundary assumption were similar to the results obtained for whole eye. References [21], [46], [47] adopted similar boundary conditions to their cornea models. Roy and Dupps [24] created the whole eye model and compared the displacement results with the cornea model with fixed sclera to show that the corneoscleral limbus plays an important part in predicting response of the refractive surgery. Pandolfi and Holzapfel [12] proposed a cornea model allowing rotation at the limbus and restricting displacement at the edges. Pandolfi and coworkers [23] earlier had investigated the cornea constrained against displacement and rotation, displacement only, and springs normal to the cross section. Rotation at the limbus plays part in changing the curvature of the cornea. Figure 5 illustrates these boundary conditions. Figure 6 illustrates displacement results of FE simulation of a mouse cornea subjected to IOP, with rotation at the limbus.

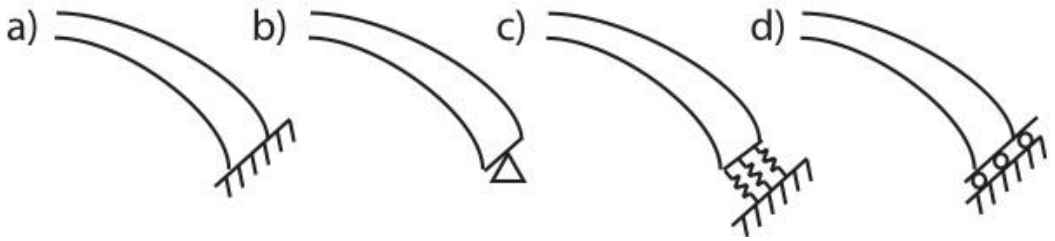

Figure 5 – Schematic of boundary conditions at the limbus used by researchers. a) The cornea is constrained against displacement and rotation, as proposed in [15]. b) The cornea is fixed against displacement, but may rotate at the edges, as in [12]. c) Springs normal to the cross-section. Researchers in [23] investigated boundary conditions (a), (b), and (c). d) Cornea is allowed to expand along a given surface, as in [21], [32], [46], [47]. Forty degrees from horizontal is taken as a typical angle.

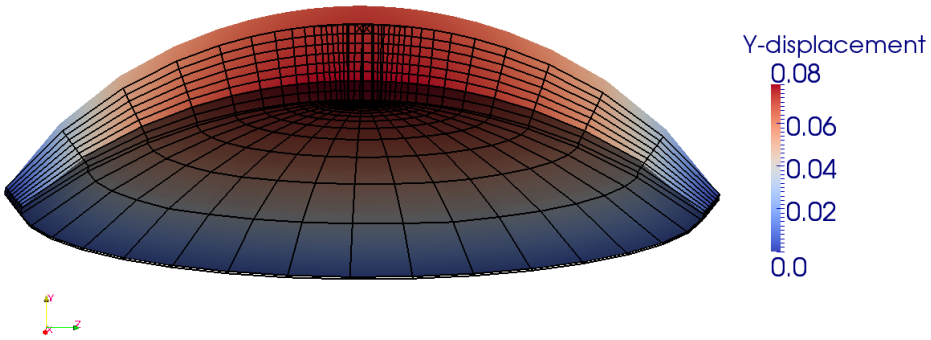

Figure 6 – An example of vertical displacement mapping of a mouse cornea subjected to IOP obtained from FE simulations is shown in cross section. The wireframe on the bottom is the undeformed mesh and vertical displacement colored by magnitude is shown on top. The cornea displacement but not rotation is restricted along the limbus.

2.2.3 Material Models

For creating a material model, the cornea material is often approximated as the stroma, which is the major contributor of mechanical strength [12], [16], [40]. The stroma layer may be modeled as a non-linear anisotropic viscoelastic material which undergoes large deformation. Finite deformation theory is incorporated in the cornea model which successfully captures its true non-linear response under deformation [12], [40].

Earlier finite element models were simple linear elastic models. One of the earlier models developed by Vito et al. [48] considered stroma as a linear elastic, homogeneous and isotropic material. Similarly Bryant et al. [49], Hanna et al. [50], Gefen et al. [22], Velinsky and Bryant [51] also assumed cornea to undergo small deformation and used linear elasticity for their analysis. Pinsky and Datye [34] developed linear material cornea model based on anisotropic constitutive model using the predominant fiber directions in the cornea.

The first geometrically nonlinear models represented the stroma as a nearly incompressible isotropic hyperelastic material. The Neo-Hookean model is widely used for modeling tissues [12], [16]. Other hyperelastic models have also been used. Niroomandi et al. used a simpler Saint Venant-Kirchhoff hyperelastic model [52]. Bryant and McDonnell created 2-D axisymmetric model to compare various isotropic and a couple transversely isotropic constitutive models of cornea [53]. Of the models they compared, an exponential nonlinear model best fit inflation experiments.

Many researchers used a base isotropic model for the matrix of the stroma, and additional terms for the effect of the fibers as discussed below. Alastrue et al. [15], Hanna et al. [50] and Pandolfi et al. [23] considered the matrix as a Mooney-Rivlin model. Nguyen et al. [39] and Pinsky et al. [16] used a Neo-Hookean model as their matrix model.

Anisotropic nonlinear hyperelastic models with embedded collagen fibers have been frequently used in recent cornea models [12], [15], [16], [40]. Alastrue et al. [15] used a discrete fiber model with embedded collagen fibers in two preferred orientations, nasal-temporal and superior-inferior directions. Most other recent models do not simulate each fiber explicitly, which is computationally expensive, but include a smeared effect of oriented fibers. Cristobal et al. [54], Pandolfi and Manganiello [20] developed their models with two preferred directions at center and circumferential at the limbus region. Pandolfi and Holzapfel [12] used distributed model with two preferred orientations. Pinsky et al. [16] and Nguyen et al. [39] developed continuous distributed fiber model with preferred orientation.

Nguyen et al. [39] created anisotropic cornea model taking into consideration viscoelastic properties. Yoo et al. [55] also used viscoelastic ocular tissue model for their study.

2.2.4 Parameter Measurement and Optimization

Cornea tissue material properties are determined by various laboratory tests of cornea specimens. The material parameters used for the cornea model are based on these studies. Wollensak et al. [56], Hoeltzel et al. [38] and Zeng et al. [57] performed uniaxial tension tests on cornea tissue to record stress-strain relation. Kohlhaas et al. [58] and Wollensak et al. [56] extended these tests to study the effect of cross-linking of collagen fibril on the mechanical response of cornea. Bryant and McDonnell [53], Elsheikh et al. [59], Anderson et al. [32] conducted inflation tests on entire cornea to determine apical displacement at different pressure values. It is worth noting that inflation tests tend to give different values for stiffness parameters compared to tensile strip tests. While the reason for this is still not completely understood, inflation tests are generally believed to more closely match the in vivo cornea behavior. Petsche

et al. [60] examined the depth-dependent material properties of the stroma. However, there is still experimental work to be done to fully determine the mechanical behavior of the cornea.

Determining model parameters from experiments is also generally nontrivial. Linear and even nonlinear isotropic parameters can be easily fit from tension tests, though again there are questions to the accuracy of those tests in vivo. Inflation tests or parameters for anisotropic models are more complicated. Inverse simulation is a mathematical approach to determine unknown model parameters to match observed or assumed physical responses. In the inverse FEM, an optimization algorithm is coupled with an FEM to find a set of optimal parameters for a given model to be used in the FE simulation. Such methods are important for determining the physical properties of actual corneas.

Nguyen and Boyce [40] presented an inverse FEM to estimate bovine corneal material properties using an in vitro inflation experiment and also to investigate the influence of variations in these properties on the bovine inflation response. They determined a set of anisotropic material properties minimizing the error between simulation results and experimental measurements of surface displacement field.

2.2.5 Summary of Finite Element Modeling Choices

Different choices in finite element models of the cornea can affect the results. Two-dimensional or shell models are efficient, but may not be able to capture the complex material behavior of some applications accurately. While modeling the entire eye may avoid approximate boundary conditions at the limbus, the computational time increases significantly. However, modeling the changing IOP under impact may be difficult without a full model of the eye.

Material models are also increasingly accurate and, at the same time, computationally more expensive. While linear models are very efficient, they may be inaccurate over large changes in deformation. Isotropic models may not accurately capture the behavior of the complex material in the stroma, but may be adequate for problems that only require a rough idea of the displacements. The depth of knowledge of the properties of corneal tissue is improving. In applications with rapid load, the viscoelastic and dynamic properties of the cornea may be important. For others, such as the long-term results of surgery, a quasi-static model is acceptable. It is important to select a model that can simulate an application with the necessary accuracy. However, a model with too much detail may become very expensive computationally.

2.3 Applications

FEA is a useful tool for studying corneal mechanical behavior and how it functions. FEA has been widely used in modeling surgical effects on the cornea as well as studying corneal diseases and eye trauma. In this section, different applications of FEA in simulation of corneal surgery, disorders, impact and etc. are studied.

2.3.1 Surgery

The curvature of the internal and external surfaces of cornea significantly affects its refractive power. Refractive eye surgery can improve the visual acuity for common refractive maladies such as astigmatism, hyperopia and myopia. In several surgical techniques the dioptric power of the cornea is improved by removing thin layers of biological tissues and adjusting the curvature of the cornea using excimer lasers [23]. Laser-assisted in-situ keratomileusis (LASIK), photorefractive keratectomy (PRK), and intrastromal photorefractive keratectomy (ISPRK) are

three main types of refractive surgeries. Refractive surgeries on cornea periphery such as conductive keratoplasty (CK) and intra-corneal ring (ICR) have recently attracted more interests. These surgeries are mainly performed on hyperopic eyes which require steepening rather than flattening of the cornea surface [47].

FEA has potential usefulness as a simulation tool for refractive surgery planning using accurate in vivo corneal material properties and geometry data [24]. FEA has been extensively used to model deformation of cornea for corneal surgery simulation and to predict mechanical and refractive effects of the surgery [33].

Pandolfi et al. [23] implemented an FEM in astigmatic and myopic corneas to evaluate the mechanical and refractive outcomes of laser refractive surgery. They computed the change in the curvature and thickness of the human cornea exposed to laser ablation and evaluated the corrected dioptric power for individual patient cases.

Roy and Dupps [24] proposed an FE model of the whole eye to give insight into refractive surgery planning. They later presented an inverse FEM to determine the undeformed state of the cornea [26]. They developed a 3-D patient-specific corneoscleral FE model to estimate the surgical impact on corneal shape variations and the changes in corneal elastic properties.

Niroomandi et al. [52] presented a novel numerical technique for actual surgery simulation using an extended finite element method (X-FEM). The X-FEM method enhances standard FE with defining additional degrees of freedom (those interested in further theory of the X-FEM are referred to Belytschko et al. [61] among others on the subject). In their model, the opening of the fracture induced by the incision in refractive surgery was reproduced using X-

FEM method. Their presented FEM was able to simulate the complex constitutive model of the cornea and to recover the scalpel cut discontinuities for the actual surgery simulations.

Nomograms in ophthalmology are sets of tables of corrected values or graphics used to plan the surgical procedure, especially for incisional surgeries for astigmatism and similar diseases [54]. Nomograms can manage the incision effect by revising the cut parameters such as depth, length and optical zone in incisional surgery. Cristóbal et al. [54] proposed a FE model of limbal incision to predict the patient-specific optical power to be induced in the surgery. The nomogram outcomes were compared to simulation results and in some cases, the nomograms were revised accordingly.

CK is a sub-ablative thermal treatment in which thin electrodes are inserted into the stroma to apply radiofrequency (RF) heating. The heat causes the peripheral corneal tissue to shrink. Jo et al. [29] developed a 3-D FE model including the cornea, the aqueous humor and the RF electrodes to investigate the resultant thermal damage during RF heating in CK procedure. Fraldi et al. [47] also presented a viscoelastic FEA to study the mechanical response of the hyperopic cornea to CK and assess the post-surgery stability of the applied refractive correction. Hameed Sayed et al. [62] created a 3-D FE model to simulate the ISPRK technique for correcting myopic corneas and predicting the treatment results. The simulation outcomes were compared with the results from an earlier 2-D FE model developed by Bryant et al. [49] for the same purpose. The model outputs were more correlated to the clinical data compared to the 2-D model.

2.3.2 Corneal Diseases

Finite element analysis has been widely used to study biomechanical interactions in corneal maladies (e.g. keratoconus) and to better understand aetiology and treatment of the diseases. FEM can be used to investigate the effect of variations in corneal material properties on vision power in corneal diseases.

Keratoconus is a degenerative corneal disease characterized by irregular thinning and bulging of the cornea structure and progressive topographic irregularity in the cornea. This shape distortion leads to optical aberration that might be corrected in mild cases by using hard contact lenses or glasses or may require corneal transplantation at more severe conditions [22]. Collagen across-linking (CXL) is a new method for treating keratoconus. In this technique, the epithelium is usually removed from the central zone of the cornea and a riboflavin solution is penetrated into the stroma [26]. Under ultraviolet (UV) radiation, the riboflavin creates additional cross-linking in the collagen fibrils, stiffening the cornea.

Gefen et al. [22] presented a 3-D linear anisotropic FE model of normal and keratoconic corneas to investigate the mechanical behavior and optical performance. The analysis results revealed that IOP level had a considerable influence in the optical power of the keratoconic cornea while having little effect on refractive power of normal cornea. Roy and Dupps presented a 3-D patient-specific FE model of a whole eye to study keratoconus progression [26]. The model was able to demonstrate a patient-specific procedure for investigating the locally reduced corneal elastic properties during the keratoconus development.

Carvalho et al. presented an FEM of a keratoconic cornea to predict the biomechanical behavior and evolution of cornea in keratoconus [21]. Using shell elements, they investigated how variations in IOP and material properties of the cornea (i.e. reduction in rigidity of cornea)

can lead to a localized increase in corneal curvature. Foster et al. [63] examined the stiffening effect of cross-linking on the collagen fibers in corneal tissue, fitting material parameters to experiments on cornea strips.

2.3.3 Impact and Trauma

Ocular trauma can cause long-term vision disorders and is expensive to treat [64]. FEM is a useful tool for simulating ocular trauma. It may offer possible solutions for reducing eye impact injuries and designing protective tools against globe trauma. Impact of different projectiles with the eye has been simulated using FEA to investigate the injury potential.

Stitzel et al. [64] offered a nonlinear FEM of human eye to predict the eye rupture injury caused by high speed blunt impacts. The numerical model was verified with experiments to predict the injury due to different types of impacting projectiles and loading conditions.

Weaver et al. implemented a numerical model of eye impact considering a variety of blunt projectiles and loading conditions, based on many experimental impact tests [65]. They investigated the effect of different projectile mass, size, material properties and velocity on response of the eye to impact. The study results gave insight into predicting eye rupture in various loading conditions and designing eye safety equipment.

Gray et al. studied the impact of paintballs on the cornea, with the aim of designing safer paintballs [66]. To this end, they implemented a numerical model of human eye, orbit and paintball into the CTH computer code (a 3-D finite-volume and large deformation numerical hydrocode developed by Sandia National Laboratory) to study the physical mechanism causing the eye impact injury. By varying material properties they concluded paintballs with less mass could be safer for the eye.

Uchio et al. also presented a 3-D FEA supercomputer simulation of eyeball traumatic impact. They investigated the threshold of impact eye injuries caused by different size and velocity bodies [44].

2.3.4 Other Applications

FEM can be used as a potential non-invasive tool in clinical applications for investigating biomechanical behavior of the cornea and the characteristic measurements. FEM may be a critical method for assessing corneal mechanical and electrical properties as well as IOP measurements.

Applanation tonometry is among the most widely used contact tonometry techniques for IOP measurements. FEM has been applied to examine applanation tonometry in order for measuring IOP [42]. Ghaboussi et al. developed a computationally efficient numerical method to accurately measure IOP in the cornea using a modified applanation tonometer [67]. They used a combination of neural network and genetic algorithm to fit clinical applanation tonometry outcomes (force and displacement history data) to that achieved from FE model.

As the heart beats, the intraocular pressure (IOP) behind the cornea changes; the vibration characteristics of the eye also vary with IOP. Salimi et al. developed a coupled fluid-structure FEM of the eye and investigated the dynamic response of the eye to changing IOP [42]. They validated the vibrational characteristics from simulation model with experimental modal analysis (EMA) of a water filled spherical shell.

Rhee et al. developed a nonlinear anisotropic FE model of mouse cornea to study formation of spiral patterns on the epithelium [10]. They compared the obtained numerical

curves of maximum shear strain with actual spiral patterns observed in x-ray images of mouse cornea. The presented work helped provide insight into possible development of cornea.

2.4 Conclusion

FEA is a powerful numerical technique for finding approximate solutions to partial differential equations in complex structures. FEA may be used to simulate a wide range of biological structures and body organs. In this work, different application of FEA in studying mechanical behavior of the cornea was reviewed. The review includes studying a wide variety of applications ranging from surgery to disease and impact simulation.

Based on the articles reviewed, FEA has been used to develop a better understanding of the mechanics of the cornea in a variety of settings. It can be a noninvasive predictive method for assessing corneal function and properties and studying related diseases. The FE models can be used in clinical applications to investigate corneal malfunctions and present possible treatments. FEA can predict the pre and post-operative responses of the cornea to refractive surgeries and may be used as a patient-specific simulation tool in clinical applications for surgical planning.

In the future, FE models may become important tools in planning treatments. Initially, the models will be used to improve procedural parameters such as incision locations and depths. However, it will soon be possible to provide patient-specific cornea models that can be used to plan individual surgeries and predict outcomes, such as optimal treatment times and concentrations for collagen cross-linking.

Obtaining the parameters for the stiffness of individual corneas, especially in vivo, remains challenging. A combination of investigations excised corneas and simple tests in vivo corneas will be able to give reasonably data to approximate patient-specific cornea properties.

Ongoing investigations on the complex mechanical properties of the cornea will continue to create more realistic and accurate models for all these applications.

3 Integral-averaged $\bar{B}$ Method for Nearly Incompressible Nonlinear Deformation

3.1 Introduction

Many materials exhibit nearly incompressible responses over some part of their deformation. Biological tissues, rubbers, metals undergoing plastic deformation, and soil under undrained conditions are examples. To model these materials in a finite element context, care has to be taken to use elements designed for nearly incompressible behavior. The fact that low-order finite elements perform poorly for nearly incompressible media is well known. There are several ways to view the problem, but one is that in standard elements have too many incompressibility constraints, which overwhelm the shear response. While higher-order elements can relieve this, even they do not behave optimally. And for certain classes of problems, such as some dynamic problems or problems involving jumps in the displacement field, low-order elements are generally preferred.

Many solutions have been proposed to relieve this volumetric locking effect in low-order elements, particularly quadrilaterals and hexahedra. Reduced integration [68] can reduce the number of volumetric constraints, but results in spurious non-zero energy modes, often called hourglass modes. However, modification can control these modes [69]–[72] among others). Mixed methods treat the mean stress as a separate variable. While effective, the extra set of equations complicates the process and results in higher computation time [73]–[75] among others). It should be noted that many times the extra variable may be condensed at the element level, minimizing this extra cost. Assumed enhanced strain formulations add extra terms to the

strain and can relieve locking, for example in [76], [77]. Variational multiscale methods [78]–[80] and other stabilization techniques ([81] among others) have also been employed to relieve locking, but also add extra complexity to the system.

Because they can be implemented relatively simply in a displacement-only framework, so-called $\bar{\boldsymbol{B}}$ methods have been highly popular. Discussed in [43] for linear elements, these elements replace the volumetric part of the strain displacement matrix with a reduced-order integration or averaged value. The reduced interpolation order of the volumetric term reduces the number of constraints, relieving the locking. No extra degrees of freedom are added to the system, though in some cases additional integration points are added. While these elements do not formally satisfy the Ladyzenskaya-Babuska-Brezzi conditions [82], [83] that determine whether locking should be relieved, they perform well in practice and their relative ease of implementation has made the approach popular.

For the finite deformation case, these methods have been extended using a so-called $\bar{\boldsymbol{F}}$ approach. This approach takes a reduced order or average evaluation of the deformation gradient $\boldsymbol{F}$. Several variations on this idea have been proposed, including reduced integration scheme for the logarithm of the volumetric deformation [84], reduced integration scheme for the volumetric deformation [85], and an average over the reference of the Jacobian [86]. In another approach, average Jacobian $\bar{J}$ is defined by relating it to a volume change parameter [87]. Most authors choose to use the $\bar{\boldsymbol{B}}$ modification for the gradient weighting function (virtual velocity gradient), though some do not [85]. While it has not been emphasized in the literature, each choice of $\bar{\boldsymbol{F}}$ determines a corresponding $\bar{\boldsymbol{B}}$ matrix. Many authors do not comment on the stiffness matrix.

In this Chapter, we develop an 8-node hexahedral element that averages the Jacobian over the element. While the integration procedure adds some modest complexity to the

computation time to the code, it avoids tracking variables at an extra integration point. Extra integration points can add memory costs. They can also add significant complexity in multiphysics problems or history-dependent materials, though we do not investigate those here. We examine integral averages in both the reference and current configurations, and detail the relationship between the choice of $\bar{\boldsymbol{F}}$ and $\bar{\boldsymbol{B}}$, as well as explicitly deriving the stiffness matrix.

While beyond the scope of this dissertation, it bears mentioning the $\bar{\boldsymbol{B}}$ method does not work for linear triangles and tetrahedra, as the volumetric deformation is already constant in the element. However, the concepts have been extended to these elements using a method termed "$\bar{\boldsymbol{F}}$-patch", where the volumetric deformation is taken as not constant over a single element, but a small patch of neighboring elements [88]. Recently, a $\bar{\boldsymbol{B}}$ approach has been applied to NURBS-based finite elements as well [87], [89].

The remainder of this Chapter is organized as follows: Section 3.2 discusses integral averages for $\bar{\boldsymbol{F}}$**,** including two of several possible choices. Section 3.3 derives the $\bar{\boldsymbol{B}}$ formulation consistent with choice of $\bar{\boldsymbol{F}}$. The stiffness matrix is presented in section 3.4, though the full derivation is relegated to the Appendix. This Section is followed by numerical examples and, finally a conclusion.

3.1.1 Notation

A few notes on notation: We employ the summation convention in this dissertation, that a repeated index within a single term of an expression has an implied sum over the range of the index. For Example $A_{ii} = tr(\boldsymbol{A})$, where $tr(.)$ is the trace operator, and $A_{ij}\, x_j = b_j$ is equivalent to $\boldsymbol{Ax} = \boldsymbol{b}$.

Outer products are represented with the "⊗" symbol, e.g. for two matrices $\boldsymbol{A}$ and $\boldsymbol{B}$, $(\boldsymbol{A} \otimes \boldsymbol{B})_{ijkl} = A_{ij} B_{kl}$. For a matrix $\boldsymbol{A}$ and vector $\boldsymbol{v}$, $(\boldsymbol{A} \otimes \boldsymbol{v})_{ijk} = A_{ij} v_k$, and for two vectors $\boldsymbol{u}$ and $\boldsymbol{v}$, $(\boldsymbol{u} \otimes \boldsymbol{v})_{ij} = u_i v_j$.

First- and second-order tensors are denoted with in bold, e.g. $\boldsymbol{\sigma}$ or $\boldsymbol{d}$. Third-order tensors of matrices are written in calligraphic script, for example, $\boldsymbol{\mathcal{B}}$, and fourth-order tensors in blackboard bold, such as $\mathbb{C}$.

We use curly braces for second-order tensors converted to vectors in Voigt notation. Kinematic quantities have doubled off-diagonal terms unless stated otherwise, while other quantities do not. For example

$$\{\boldsymbol{\tau}\} = \begin{Bmatrix} \tau_{11} \\ \tau_{22} \\ \tau_{33} \\ \tau_{23} \\ \tau_{31} \\ \tau_{12} \end{Bmatrix}; \qquad \{\boldsymbol{l}\} = \begin{Bmatrix} l_{11} \\ l_{22} \\ l_{33} \\ l_{23} + l_{32} \\ l_{31} + l_{13} \\ l_{12} + l_{21} \end{Bmatrix} \tag{1}$$

Similarly, fourth-order tensors converted to Voigt-form matrices are denoted with brackets, e.g. $[\mathbb{C}]$.

3.2 Review on the Selective Reduced Integration Methods for Linear FEM

In standard elements, the strain field is volume preserving at all the integration points. Therefore, in the Reduced Integration method, the number of integration points is reduced to prevent the volumetric locking. In this method, the element stiffness matrix is calculated using fewer numbers of integration points (usually one order of accuracy less). In full reduced integration, the under integration results in spurious non-zero energy modes, often termed

hourglass modes. While the global solution may still be adequate, the local variations can be undesirable. Hourglass control can correct this, or selective reduced integration may be employed.

In selective reduced integration, the stiffness matrix is separated into two parts: The isochoric part ($\boldsymbol{k}^{iso}$), and the volumetric part ($\boldsymbol{k}^{vol}$). The numerical value of the second part is usually much larger than the first part [68]. The $\boldsymbol{k}^{vol}$ term is responsible for preventing the locking behavior in nearly incompressible materials and therefore is treated differently. $\boldsymbol{k}^{vol}$ is calculated using fewer quadrature points (reduced integration points) to reserve volumetrically stiff behavior. Whereas $\boldsymbol{k}^{iso}$ is evaluated using full integration method.

The element stiffness is found from:

$$\boldsymbol{k}^{e} = \boldsymbol{k}^{e\,iso} + \boldsymbol{k}^{e\,vol} = \int_{\Omega^e} \boldsymbol{B}^T \boldsymbol{D}^{iso} \boldsymbol{B}\, d\Omega + \int_{\Omega^e} \boldsymbol{B}^T \boldsymbol{D}^{vol} \boldsymbol{B}\, d\Omega \tag{2}$$

In three-dimensional analysis, $\boldsymbol{D}^{iso}$ and $\boldsymbol{D}^{vol}$ may be written as:

$$\boldsymbol{D}^{iso} = K \begin{bmatrix} 1 & 1 & 1 & 0 & 0 & 0 \\ 1 & 1 & 1 & 0 & 0 & 0 \\ 1 & 1 & 1 & 0 & 0 & 0 \\ 0 & 0 & 0 & 0 & 0 & 0 \\ 0 & 0 & 0 & 0 & 0 & 0 \\ 0 & 0 & 0 & 0 & 0 & 0 \end{bmatrix} \tag{3}$$

$$\boldsymbol{D}^{vol} = 2\mu \begin{bmatrix} \frac{2}{3} & -\frac{1}{3} & -\frac{1}{3} & 0 & 0 & 0 \\ -\frac{1}{3} & \frac{2}{3} & -\frac{1}{3} & 0 & 0 & 0 \\ -\frac{1}{3} & -\frac{1}{3} & \frac{2}{3} & 0 & 0 & 0 \\ 0 & 0 & 0 & 1 & 0 & 0 \\ 0 & 0 & 0 & 0 & 1 & 0 \\ 0 & 0 & 0 & 0 & 0 & 1 \end{bmatrix}$$

(4)

In which K is the bulk modulus and μ is the shear modulus.

3.3 Review on Volume Average $\bar{\boldsymbol{B}}$ Formulation for Linear Elasticity

As stated before, standard low order finite elements are not accurate for the analysis of nearly incompressible materials as over-stiff response may be observed. A popular solution to prevent incompressibility in these elements is the $\bar{\boldsymbol{B}}$ method.

Strain-displacement matrix may be written in terms of nodal sub-matrices as:

$$\boldsymbol{B} = [\, \boldsymbol{B}_1,\ \boldsymbol{B}_2,\ \ldots,\ \boldsymbol{B}_{n_{en}}]$$

(5)

In which n_{en} is the number of element nodes

In 3D analysis a sub-matrix $\boldsymbol{B}_a$ is:

$$\boldsymbol{B}_a = \begin{bmatrix} B_1\, B_2\, B_3 \\ B_1\, B_2\, B_3 \\ B_1\, B_2\, B_3 \\ 0\; B_3\; B_2 \\ B_3\; 0\;\; B_1 \\ B_2\; B_1\; 0 \end{bmatrix}$$

(6)

In which $B_i = \frac{\partial N_a}{\partial x_i}$ for *i = 1, 2, 3* and N_a is the shape function at node a

In the $\bar{\boldsymbol{B}}$ method, strain-displacement matrix $\boldsymbol{B}$ is split into an isochoric and a volumetric part.

$$\bar{\boldsymbol{B}}_a = \boldsymbol{B}_a^{iso} + \bar{\boldsymbol{B}}_a^{vol}$$

(7)

The isochoric part of $\boldsymbol{B}_a$ is given as:

$$\boldsymbol{B}_a^{iso} = \boldsymbol{B}_a - \boldsymbol{B}_a^{vol}$$

(8)

In which the volumetric part is:

$$\boldsymbol{B}_a^{vol} = \frac{1}{3} \begin{bmatrix} B_1\, B_2\, B_3 \\ B_1\, B_2\, B_3 \\ B_1\, B_2\, B_3 \\ 0\;\; 0\;\; 0 \\ 0\;\; 0\;\; 0 \\ 0\;\; 0\;\; 0 \end{bmatrix}$$

(9)

The over-stiff response is formed in the volumetric part. Therefore, in the $\bar{\boldsymbol{B}}$ method in order to circumvent this constraint, the volumetric part is modified as follows:

$$\bar{\boldsymbol{B}}_a^{vol} = \frac{1}{3}\begin{bmatrix} \bar{B}_1 & \bar{B}_2 & \bar{B}_3 \\ \bar{B}_1 & \bar{B}_2 & \bar{B}_3 \\ \bar{B}_1 & \bar{B}_2 & \bar{B}_3 \\ 0 & 0 & 0 \\ 0 & 0 & 0 \\ 0 & 0 & 0 \end{bmatrix}$$

(10)

According to mean-dilatation formulation, $\bar{B}_i(\xi)$ may be derived as:

$$\bar{B}_i(\xi) = \frac{\int_{\Omega^e} B_i \, d\Omega}{\int_{\Omega^e} d\Omega}$$

(11)

$$B_i = \frac{\partial N_a}{\partial x_i}$$

(12)

Similar to selective reduced integration, $\bar{\boldsymbol{B}}$ can also be evaluated using a reduced integration rule rather than volume averaging.

3.4 $\bar{\boldsymbol{F}}$ Formulations

The basis of the $\bar{\boldsymbol{F}}$ formulation for geometrically nonlinear material models is to replace the dependence of the stress on the deformation gradient $\boldsymbol{F}$ with a dependence on a modified deformation gradient $\bar{\boldsymbol{F}}$

$$\boldsymbol{\tau} = \boldsymbol{\tau}(\bar{\boldsymbol{F}}, \ldots)$$

(13)

Here, $\boldsymbol{\tau}$ is the Kirchhoff stress, though the use of any stress measure may suffice. The ellipsis is a reminder that the stress may also be a function of the rate of deformation, internal

state variables, or other quantities. To relieve volumetric locking associated with nearly incompressible materials, typically the volumetric part of $\boldsymbol{F}$ is replaced by an average or reduced order approximation. To accomplish this task, $\boldsymbol{F}$ is typically split into a volumetric component $\boldsymbol{F}^{vol}$ and an isochoric component $\boldsymbol{F}^{iso}$ such that

$$\boldsymbol{F} = \boldsymbol{F}^{vol}\boldsymbol{F}^{iso} \tag{14}$$

$$\boldsymbol{F}^{vol} = J^{1/3}\,\boldsymbol{I} \quad ; \quad \boldsymbol{F}^{iso} = J^{-1/3}\,\boldsymbol{F} \tag{15}$$

$$det\ \boldsymbol{F}^{vol} = det\ \boldsymbol{F} = J \ ; \quad det\ \boldsymbol{F}^{iso} = 1 \tag{16}$$

where $\boldsymbol{1}$ is the second order identity tensor and $J = det\ \boldsymbol{F}$ is the Jacobian of the deformation. The Jacobian, then, is replaced with some modified $\bar{J}$, resulting in a modified deformation gradient

$$\overline{\boldsymbol{F}} = \overline{\boldsymbol{F}}^{vol}\boldsymbol{F}^{iso} = \left(\frac{\bar{J}}{J}\right)^{1/3}\boldsymbol{F} \tag{17}$$

$$\overline{\boldsymbol{F}}^{vol} = \bar{J}^{1/3}\,\boldsymbol{I} \quad ; \ \det \overline{\boldsymbol{F}}^{vol} = \bar{J} \tag{18}$$

Many forms for $\bar{J}$ have been proposed. Effective choices should reduce the order of the volumetric strain interpolation to reduce the number of volumetric constraints. One of the simplest for trilinear hexahedra (and their two-dimensional counterparts, the bilinear quadrilaterals) is to evaluate the modified Jacobian at the center of the element, $\bar{J} = J(\boldsymbol{\xi} = \boldsymbol{0})$, for example in [84]. The drawback of this approach is that the deformation must be evaluated at an

extra Gauss point. This extra data modestly increases memory requirements and increases the complexity of the code. The complexity increases for more complex constitutive models such as plasticity models, where internal state variables and other quantities must be tracked, and multiphysics formulations, where mechanical quantities must be shared with quantities from the other physics.

An alternative approach is to use an averaging scheme or stabilization procedure. We adopt the former in this work. Specifically, we examine two possibilities

$$\bar{J} = \frac{\int_{\Omega_0{}^e} J \; d\Omega_0}{\int_{\Omega_0{}^e} d\Omega_0} \tag{19}$$

$$J = \frac{\int_{\Omega^e} J \; d\Omega}{\int_{\Omega^e} d\Omega} \tag{20}$$

The first is a volume average of the Jacobian over the reference configuration $\Omega_0{}^e$, the second a volume average over the current configuration Ω^e. Since the reference configuration is at times an arbitrary theoretical state, there is some logic to adopting the second. However, the formulation for the former we will see is simpler, and for nearly incompressible materials, there is not a great difference between the volume in the current and reference configurations.

Note: As discussed in [84] for very nearly incompressible or completely incompressible materials, hourglass modes may appear due to ill-conditioning of the stiffness matrix. These modes can be alleviated by replacing $\overline{\boldsymbol{F}}$ with an $\widetilde{\boldsymbol{F}}$, composed of $\overline{\boldsymbol{F}}$ and $\boldsymbol{F}$. The authors in [84] use $\widetilde{\boldsymbol{F}} = \varepsilon \, \boldsymbol{F} + (1 - \varepsilon) \; \overline{\boldsymbol{F}}$, for some relatively "small" ε (originally suggested in [90]). Similarly, Doll and coworkers [91] proposed a $\tilde{J} = J^{\,\varepsilon} \; \bar{J}^{(1-\varepsilon)}$. For models which use a volumetric penalty parameter, however, these modes may also be eliminated by setting the volumetric penalty

stiffness not too much higher than the shear stiffness. We do not perform a formal analysis of appropriate penalty parameter values in this dissertation, but roughly three to four orders of magnitude higher than shear stiffness parameters appear to be appropriate values in practice.

3.5 Consistent $\bar{\boldsymbol{B}}$ Formulations

The appropriate function for the $\bar{\boldsymbol{B}}$ follows from the chosen form for $\bar{\boldsymbol{F}}$. One can derive the standard $\boldsymbol{B}$ matrix from the velocity gradient $\boldsymbol{l}$ using a pseudo-time derivative, as shown in [92]. In a finite element context

$$\{\boldsymbol{l}\} = \boldsymbol{B}\dot{\boldsymbol{d}} \tag{21}$$

where $\boldsymbol{d}$ in this dissertation refers to the vector of element nodal displacements (we have dropped the common superscript ^{e} to simplify the notation). We adopt a similar approach to derive $\bar{\boldsymbol{B}}$, i.e.

$$\{\bar{\boldsymbol{l}}\} = \bar{\boldsymbol{B}}\,\dot{\boldsymbol{d}} \tag{22}$$

First, we must derive an expression for the modified velocity gradient $\bar{\boldsymbol{l}}$

$$\bar{\boldsymbol{l}} = \dot{\bar{\boldsymbol{F}}}\,\bar{\boldsymbol{F}}^{-1} \tag{23}$$

$$\bar{\boldsymbol{F}}^{-1} = \left(\frac{J}{\bar{J}}\right)^{1/3}\boldsymbol{F}^{-1} \tag{24}$$

The expression for $\dot{\bar{\boldsymbol{F}}}$ can be determined as

$$\dot{\bar{\boldsymbol{F}}} = \left(\frac{\bar{J}}{J}\right)^{1/3} \dot{\boldsymbol{F}} + \frac{1}{3}\left(\frac{\bar{J}}{J}\right)^{-2/3} \frac{d}{dt}\left(\left(\frac{\bar{J}}{J}\right)\right)\boldsymbol{F}$$

$$= \left(\frac{\bar{J}}{J}\right)^{1/3} \dot{\boldsymbol{F}} + \frac{1}{3}\left(\frac{\dot{\bar{J}}}{J} - \frac{\bar{J}\dot{J}}{J^2}\right)\left(\frac{\bar{J}}{J}\right)^{2/3} \boldsymbol{F}$$

$$= \left(\frac{\bar{J}}{J}\right)^{1/3} \dot{\boldsymbol{F}} + \frac{1}{3}\left(\frac{\dot{\bar{J}}}{\bar{J}} - \frac{\dot{J}}{J}\right)\left(\frac{\bar{J}}{J}\right)^{1/3} \boldsymbol{F}$$

$$= \left(\frac{\bar{J}}{J}\right)^{\frac{1}{3}} \dot{\boldsymbol{F}} + \frac{1}{3}\left(\frac{\dot{\bar{J}}}{\bar{J}} - \frac{\dot{J}}{J}\right)\bar{\boldsymbol{F}}$$

$$= \left(\frac{\bar{J}}{J}\right)^{\frac{1}{3}} \dot{\boldsymbol{F}} + \frac{1}{3}\left(\, tr(\bar{\boldsymbol{l}}) - tr(\boldsymbol{l})\,\right)\bar{\boldsymbol{F}}$$

(25)

Here we define $(\bar{\boldsymbol{l}}) = \frac{\dot{\bar{J}}}{\bar{J}}$. This quantity will depend, of course, on the choice of $\bar{J}$. We derive this quantity in a moment for the choices we have considered, but first note that for any choice of $\bar{J}$

$$\bar{\boldsymbol{l}} = \dot{\bar{\boldsymbol{F}}}\,\bar{\boldsymbol{F}}^{-1}$$

$$= \left[\left(\frac{\bar{J}}{J}\right)^{\frac{1}{3}} \dot{\boldsymbol{F}} + \frac{1}{3}\left(\, tr(\bar{\boldsymbol{l}}) - tr(\boldsymbol{l})\right)\bar{\boldsymbol{F}}\right]\left[\left(\frac{\mathrm{J}}{\bar{\mathrm{J}}}\right)^{\frac{1}{3}} \boldsymbol{F}^{-1}\right]$$

$$= \dot{\boldsymbol{F}}\boldsymbol{F}^{-1} + \frac{1}{3}\left(\, tr(\bar{\boldsymbol{l}}) - tr(\boldsymbol{l})\,\right)\bar{\boldsymbol{F}}\,\bar{\boldsymbol{F}}^{-1}$$

$$= \boldsymbol{l} + \tfrac{1}{3}\left(\, tr(\bar{\boldsymbol{l}}) - tr(\boldsymbol{l})\,\right)\mathbf{1}$$

(26)

where we use $\boldsymbol{1}$ as the second order identity tensor. Note that this has the familiar form of the small strain $\bar{\boldsymbol{B}}$ formulation where the volumetric part of the tensor is replaced with the modified component.

For the choice of $\bar{J} = \frac{\int_{\Omega_0{}^e} J \, d\Omega_0}{\int_{\Omega_0{}^e} d\Omega_0}$,

$$\dot{\bar{J}} = \frac{d}{dt}\left(\frac{\int_{\Omega_0{}^e} J \; d\Omega_0}{\int_{\Omega_0{}^e} d\Omega_0}\right)$$

$$= \frac{\int_{\Omega_0{}^e} \dot{J} \; d\Omega_0}{\int_{\Omega_0{}^e} d\Omega_0}$$

$$= \frac{\int_{\Omega_0{}^e} J \; tr(\boldsymbol{l}) \; d\Omega_0}{\int_{\Omega_0{}^e} d\Omega_0}$$

(27)

Hence

$$tr(\bar{\boldsymbol{l}}) = \frac{\int_{\Omega_0{}^e} J \; tr(\boldsymbol{l}) \; d\Omega_0}{\bar{J} \int_{\Omega_0{}^e} d\Omega_0}$$

$$= \frac{\int_{\Omega_0{}^e} J \; tr(\boldsymbol{l}) \; d\Omega_0}{\int_{\Omega_0{}^e} J \; d\Omega_0}$$

(28)

Curiously, averaging *J* over the reference configuration results in $tr(\boldsymbol{l})$ being averaged over the current configuration.

Averaging *J* over the current configuration results in a somewhat more complicated formulation. In this case

$$\dot{\bar{J}} = \frac{d}{dt}\left(\frac{\int_{\Omega^e} J \; d\Omega}{\int_{\Omega^e} d\Omega}\right)$$

$$= \frac{d}{dt}\left(\frac{\int_{\Omega_0{}^e} J^2\, d\Omega_0}{\int_{\Omega_0{}^e} J\, d\Omega_0}\right)$$

$$= \left(\frac{\int_{\Omega_0{}^e} 2J\dot{J}\, d\Omega_0}{\int_{\Omega_0{}^e} J\, d\Omega_0}\right) - \frac{\int_{\Omega_0{}^e} J^2\, d\Omega_0}{(\int_{\Omega_0{}^e} J\, d\Omega_0)^2}\int_{\Omega_0{}^e} \dot{J}\, d\Omega_0$$

$$= \left(\frac{2\int_{\Omega_0{}^e} J^2 tr(\boldsymbol{l})\, d\Omega_0}{\int_{\Omega_0{}^e} J\, d\Omega_0}\right) - \frac{\int_{\Omega_0{}^e} J^2\, d\Omega_0}{(\int_{\Omega_0{}^e} J\, d\Omega_0)^2}\int_{\Omega_0{}^e} J\, tr(\boldsymbol{l})\, d\Omega_0$$

$$= \left(\frac{\int_{\Omega_0{}^e} J^2\, d\Omega_0}{\int_{\Omega_0{}^e} J\, d\Omega_0}\right)\left(\frac{2\int_{\Omega_0{}^e} J^2 tr(\boldsymbol{l})\, d\Omega_0}{\int_{\Omega_0{}^e} J^2\, d\Omega_0} - \frac{\int_{\Omega_0{}^e} J\, tr(\boldsymbol{l})\, d\Omega_0}{\int_{\Omega_0{}^e} J d\Omega_0}\right)$$

$$= \bar{J}\left(\frac{2\int_{\Omega_0{}^e} J^2 tr(\boldsymbol{l})\, d\Omega_0}{\int_{\Omega_0{}^e} J^2\, d\Omega_0} - \frac{\int_{\Omega_0{}^e} J\, tr(\boldsymbol{l})\, d\Omega_0}{\int_{\Omega_0{}^e} J\, d\Omega_0}\right)$$

(29)

Hence

$$tr(\bar{\boldsymbol{l}}) = \frac{\dot{\bar{J}}}{\bar{J}} = \frac{2\int_{\Omega_0{}^e} J^2 tr(\boldsymbol{l})\, d\Omega_0}{\int_{\Omega_0{}^e} J^2\, d\Omega_0} - \frac{\int_{\Omega_0{}^e} J\, tr(\boldsymbol{l})\, d\Omega_0}{\int_{\Omega_0{}^e} J\, d\Omega_0}$$

(30)

In a finite element context, we can factor out the element nodal velocity vector implicit in the equations from the finite element shape functions. Recall that

$$l_{ij} = N_{I,j}\,\dot{d}_{Ii}$$

(31)

$$\Rightarrow \quad tr(\boldsymbol{l}) = N_{I,j}\,\dot{d}_{Ii} = \boldsymbol{\nabla} N_I \,.\, \dot{\boldsymbol{d}}_I$$

(32)

Where d_{Ii} is the ith degree of freedom for element nodal displacement subvector $\boldsymbol{d}_I$. The $\boldsymbol{\nabla}$ operator in the dissertation is used with respect to the current coordinates. Therefore

$$\bar{\boldsymbol{l}} = \boldsymbol{l} + \frac{1}{3}\left(tr(\bar{\boldsymbol{l}}) - tr(\boldsymbol{l}) \right) \mathbf{1}$$

$$= \boldsymbol{\mathcal{B}}_I \dot{\boldsymbol{d}}_I + \tfrac{1}{3}\left[(\boldsymbol{1} \otimes \overline{\boldsymbol{\nabla} N_I}\,)\, \dot{\boldsymbol{d}}_I - (\boldsymbol{1} \otimes \boldsymbol{\nabla} N_I\,)\, \dot{\boldsymbol{d}}_I \right]$$

$$= \left[\boldsymbol{\mathcal{B}}_I + \tfrac{1}{3}\left(\boldsymbol{1} \otimes \overline{\boldsymbol{\nabla} N_I}\,\right) - (\boldsymbol{1} \otimes \boldsymbol{\nabla} N_I\,) \right] \dot{\boldsymbol{d}}_I$$

(33)

Here $\boldsymbol{\mathcal{B}}_I$ is the third-order tensor that relates the velocity gradient to the nodal velocity subvector $\dot{\boldsymbol{d}}_I$.

$$(\boldsymbol{\mathcal{B}}_I)_{ija} = N_{I,j}\, \delta_{ia}$$

(34)

In other words, it is the tensor equivalent of the standard updated Lagrangian $\boldsymbol{B}_I$ matrix (see, for example, [92]).

Gradients here are with respect to current coordinates. For a given choice of $\bar{J}$, we only need to calculate the appropriate $\overline{\boldsymbol{\nabla} N_I}$. For the Jacobian averaged over the reference configuration

$$tr(\bar{\boldsymbol{l}}) = \frac{\int_{\Omega_0{}^e} J\, tr(\boldsymbol{l})\; d\Omega_0}{\int_{\Omega_0{}^e} J\, d\Omega_0}$$

$$= \frac{\int_{\Omega_0{}^e} J\, \boldsymbol{\nabla} N_I . \dot{\boldsymbol{d}}_I\; d\Omega_0}{\int_{\Omega_0{}^e} J\, d\Omega_0}$$

$$= \frac{\int_{\Omega_0{}^e} J\, \boldsymbol{\nabla} N_I\; d\Omega_0}{\int_{\Omega_0{}^e} J\, d\Omega_0} . \dot{\boldsymbol{d}}_I$$

$$= \overline{\boldsymbol{\nabla} N_I} . \dot{\boldsymbol{d}}_{\mathrm{I}}$$

(35)

where:

$$\overline{\boldsymbol{\nabla} N_I} \;=\; \frac{\int_{\Omega_0{}^e} J\,\boldsymbol{\nabla} N_I \; d\Omega_0}{\int_{\Omega_0{}^e} J \; d\Omega_0}$$

(36)

Similarly, for the Jacobian averaged in the current configuration:

$$tr\big(\bar{\boldsymbol{l}}\big) = \frac{2\int_{\Omega_0{}^e} J^2 tr(\boldsymbol{l})\, d\Omega_0}{\int_{\Omega_0{}^e} J^2 \; d\Omega_0} - \frac{\int_{\Omega_0{}^e} J\, tr(\boldsymbol{l}) \; d\Omega_0}{\int_{\Omega_0{}^e} J \; d\Omega_0}$$

$$= \frac{2\int_{\Omega_0{}^e} J^2 \boldsymbol{\nabla} N_I . \dot{\boldsymbol{d}}_I \, d\Omega_0}{\int_{\Omega_0{}^e} J^2 \; d\Omega_0} - \frac{\int_{\Omega_0{}^e} J\,\boldsymbol{\nabla} N_I . \dot{\boldsymbol{d}}_I \; d\Omega_0}{\int_{\Omega_0{}^e} J \; d\Omega_0}$$

$$= \left(\frac{2\int_{\Omega_0{}^e} J^2 \boldsymbol{\nabla} N_I \, d\Omega_0}{\int_{\Omega_0{}^e} J^2 \; d\Omega_0} - \frac{\int_{\Omega_0{}^e} J\,\boldsymbol{\nabla} N_I \; d\Omega_0}{\int_{\Omega_0{}^e} J \; d\Omega_0}\right) . \dot{\boldsymbol{d}}_I$$

(37)

Therefore:

$$\overline{\boldsymbol{\nabla} N_I} \;=\; \frac{2\int_{\Omega_0{}^e} J^2 \boldsymbol{\nabla} N_I \, d\Omega_0}{\int_{\Omega_0{}^e} J^2 \; d\Omega_0} - \frac{\int_{\Omega_0{}^e} J\,\boldsymbol{\nabla} N_I \; d\Omega_0}{\int_{\Omega_0{}^e} J \; d\Omega_0}$$

(38)

With the correct expression for $\overline{\boldsymbol{\nabla} N_I}$, we can write

$$\bar{\boldsymbol{B}}_I \;=\; \boldsymbol{B}_I + \frac{1}{3}\left(\boldsymbol{1} \otimes \overline{\boldsymbol{\nabla} N_I} \;-\; \boldsymbol{1} \otimes \boldsymbol{\nabla} N_I\right)$$

(39)

In implementation, this expression is generally rearranged into a vector form such that

$$\{\bar{\boldsymbol{l}}\} = \; \bar{\boldsymbol{B}}\, \dot{\boldsymbol{d}}$$

(40)

In this case, the nodal submatrix $\bar{\boldsymbol{B}}_I$ takes the form

$$\bar{\boldsymbol{B}}_I = \begin{bmatrix} N_{I,1} & 0 & 0 \\ 0 & N_{I,2} & 0 \\ 0 & 0 & N_{I,3} \\ 0 & N_{I,3} & N_{I,2} \\ N_{I,3} & 0 & N_{I,1} \\ N_{I,2} & N_{I,1} & 0 \end{bmatrix} + \frac{1}{3} \begin{bmatrix} \bar{N}_{I,1} & \bar{N}_{I,2} & \bar{N}_{I,3} \\ \bar{N}_{I,1} & \bar{N}_{I,2} & \bar{N}_{I,3} \\ \bar{N}_{I,1} & \bar{N}_{I,2} & \bar{N}_{I,3} \\ 0 & 0 & 0 \\ 0 & 0 & 0 \\ 0 & 0 & 0 \end{bmatrix} - \frac{1}{3} \begin{bmatrix} N_{I,1} & N_{I,2} & N_{I,3} \\ N_{I,1} & N_{I,2} & N_{I,3} \\ N_{I,1} & N_{I,2} & N_{I,3} \\ 0 & 0 & 0 \\ 0 & 0 & 0 \\ 0 & 0 & 0 \end{bmatrix}$$

(41)

The full $\bar{\boldsymbol{B}}$ maybe written as usual as

$$\bar{\boldsymbol{B}} = [\, \bar{\boldsymbol{B}}_1,\ \bar{\boldsymbol{B}}_2,\ \ldots,\ \bar{\boldsymbol{B}}_{n_{en}}]$$

(42)

where n_{en} is the number of element nodes (8 in this case, but we keep the notation for generality).

We assume that the gradient of the weighting function, or virtual velocity vector, takes the same modifications as that used in the physical velocity gradient. Hence the element internal force vector may be written

$$\boldsymbol{f}_{int}{}^{e} = \int_{\Omega_0{}^{e}} \bar{\boldsymbol{B}}^T \{\boldsymbol{\tau}\ (\bar{\boldsymbol{F}}, \ldots)\}\, d\Omega_0$$

(43)

This derivation may also be carried out in a total Lagrangian setting, however, the volumetric part does not separate out as cleanly and the formula is more complicated.

Note: It is not strictly necessary to use the same averaging for the virtual velocity gradient as for the actual, or, in fact, any averaging. The authors in [85] use the standard **B** matrix for the virtual velocity gradient, i.e.

$$\boldsymbol{f}_{int}{}^{e} = \int_{\Omega_0{}^{e}} \boldsymbol{B}^T \{\boldsymbol{\tau}\ (\bar{\boldsymbol{F}}, \ldots)\}\, d\Omega_0$$

(44)

The resulting formulation is somewhat simpler, but is also asymmetric. As the authors point out in that article, some materials have a asymmetric tangent stiffness already, and for these materials little is lost. However, for materials with a symmetric tangent stiffness, the proposed formulation creates a symmetric stiffness matrix, which has advantages in storage and solution time.

3.6 Stiffness Matrix

The stiffness matrix may be derived by taking a directional derivative, or another pseudo-time derivative. The derivation is relegated to the appendix, where the latter approach is taken. If n_{ndof} is the number of degrees of freedom per node, the $n_{ndof} \times n_{ndof}$ nodal submatrix $\boldsymbol{K}_{IJ}^{e}$ of stiffness matrix related the residual vector for node *I* to the displacements at node *J* has the form

$$\boldsymbol{K}_{IJ}^{e} = \int_{\Omega_0{}^{e}} \overline{\boldsymbol{B}}_I^T [\,\mathbb{C}^{\tau}] \overline{\boldsymbol{B}}_J + \left(\boldsymbol{\nabla} N_I \cdot \boldsymbol{\tau} \cdot \boldsymbol{\nabla} N_J\right)\mathbf{1}$$

$$+\frac{2}{3}(\boldsymbol{\nabla} N_I \cdot \boldsymbol{\tau}) \otimes \left(\overline{\boldsymbol{\nabla} N_J} - \boldsymbol{\nabla} N_J\right) + \frac{2}{3}(\overline{\boldsymbol{\nabla} N_I} - \boldsymbol{\nabla} N_I) \otimes \left(\boldsymbol{\nabla} N_J \cdot \boldsymbol{\tau}\right)$$

$$+\frac{2\tau_{kk}}{9}(\overline{\boldsymbol{\nabla} N_I} - \boldsymbol{\nabla} N_I) \otimes \left(\overline{\boldsymbol{\nabla} N_J} - \boldsymbol{\nabla} N_J\right) + \frac{\tau_{kk}}{3}\left(\boldsymbol{\nabla} N_J \otimes \boldsymbol{\nabla} N_I + \frac{d\overline{\boldsymbol{\nabla} N_I}}{d\boldsymbol{d}_J}\right) d\Omega_0$$

(45)

where $\mathbb{C}^T$ is the tangent modulus between the convected rate of the Kirchhoff stress and the velocity gradient, i.e.

$$\boldsymbol{\tau}^{\nabla c} = \mathbb{C}^{\tau} : \boldsymbol{D}$$

(46)

The formula is general, and can be applied for any choice of $\bar{J}$. One simply has to calculate the derivative $\frac{d\overline{\nabla N_I}}{d\boldsymbol{d}_J}$. For the Jacobian averaged in the reference configuration

$$\frac{d\overline{\nabla N_I}}{d\boldsymbol{d}_J} = \frac{\int_{\Omega_0{}^e} J\,(\,\nabla N_I \otimes \nabla N_J - \nabla N_J \otimes \nabla N_I\,)\,d\Omega_0}{\int_{\Omega_0{}^e} J\;d\Omega_0} - \overline{\nabla N_I} \otimes \overline{\nabla N_J}$$

(47)

For the Jacobian averaged in the current configuration:

$$\frac{d\overline{\nabla N_I}}{d\boldsymbol{d}_J} = \frac{4\int_{\Omega_0{}^e} J^2\;\nabla N_I \otimes \nabla N_J\,d\Omega_0}{\int_{\Omega_0{}^e} J^2\;d\Omega_0} - \frac{2\int_{\Omega_0{}^e} J^2\;\nabla N_J \otimes \nabla N_I\,d\Omega_0}{\int_{\Omega_0{}^e} J^2\;d\Omega_0}$$

$$- \frac{4\left(\int_{\Omega_0{}^e} J^2\;\nabla N_I\,d\Omega_0\right) \otimes \left(\int_{\Omega_0{}^e} J^2\;\nabla N_J\,d\Omega_0\right)}{\int_{\Omega_0{}^e} J^2\;d\Omega_0} - \frac{2\int_{\Omega_0{}^e} J\;\nabla N_I \otimes \nabla N_J\,d\Omega_0}{\int_{\Omega_0{}^e} J\;d\Omega_0}$$

$$+ \frac{\int_{\Omega_0{}^e} J\;\nabla N_J \otimes \nabla N_I\,d\Omega_0}{\int_{\Omega_0{}^e} J\;d\Omega_0} - \frac{\left(\int_{\Omega_0{}^e} J\;\nabla N_I\,d\Omega_0\right) \otimes \left(\int_{\Omega_0{}^e} J\;\nabla N_J\,d\Omega_0\right)}{(\int_{\Omega_0{}^e} J\;d\Omega_0)^2}$$

(48)

Clearly the second formula is more complex than the first. These formulas are derived in the appendix.

3.7 Numerical Examples

In this section, the performance of the proposed $\bar{\boldsymbol{B}}$ method is investigated by means of numerical examples. Four numerical examples with nearly incompressible nonlinear elastic material properties are presented.

3.7.1 Three-dimensional block

In the first three numerical examples, a nearly incompressible nonlinear elastic block fixed on bottom and subjected to three different loading conditions are presented. The block is 2 meters high with a square cross section of 1 meter. The quantity we compare is the displacement at node A located at (1, 2, 1) meters.

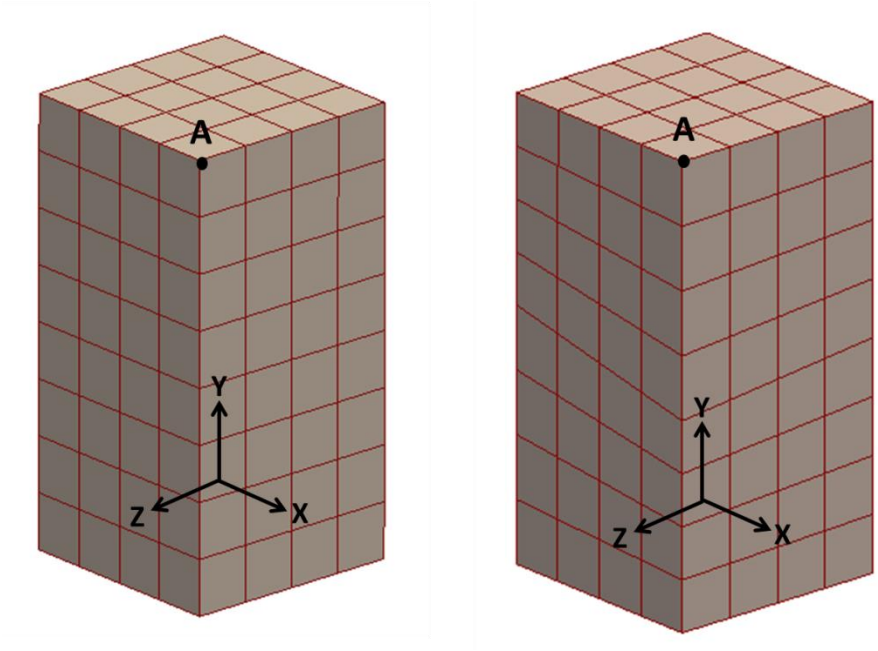

Figure 7 – Geometry of a block with 2 meters height and a square cross section of 1 meter. The block is meshed with 128 regular hexahedra (i.e. cubes) on the left and128 irregular hexahedra on the right. We focus on comparing the displacement at node A using standard and $\bar{\boldsymbol{B}}$ trilinear hexahedral elements under different loading conditions.

For this set of examples, the material model used is a Neo-Hookean model that follows the decomposition of strain energy function into isochoric and volumetric components:

$$\Psi\left(J, \boldsymbol{C}^{iso}\right) = \Psi^{iso}\left(\boldsymbol{C}^{iso}\right) + U(J) \tag{49}$$

In which U is the penalty function enforcing incompressibility constraints defined as

$$U(J) = \frac{K}{2}\,(J\ -1)^2$$

(50)

where K is a generalization of the linear bulk modulus. The isochoric part may be defined as

$$\Psi^{iso}\left(\boldsymbol{C}^{iso}\right) = \frac{\mu_0\,(I_1^{iso} - 3)}{2}$$

(51)

In which μ_0 is analogous to the shear modulus and I_1^{iso} is the first invariant of the modified right Cauchy-Green deformation tensor defined as:

$$I_1^{iso} = tr(\boldsymbol{C}^{iso})\ \ ;\ \boldsymbol{C}^{iso} = J^{-2/3}\,\boldsymbol{C}\ \ ;\ \boldsymbol{C} = \boldsymbol{F}^T\boldsymbol{F}$$

(52)

The material parameters of μ_0=60 kPa and K = 29980 kPa are used which correspond to a generalized Poisson's ratio of ν = 0.499.

This set of examples investigates the performance of three-dimensional mean dilation 8-node $\bar{\boldsymbol{B}}$ hexahedral elements employed in our large deformation FE computer code under a side pressure, compressive pressure and specified tensile displacement. The obtained displacement results are then compared to standard 8-node hexahedral elements and 8-node hexahedral $\bar{\boldsymbol{B}}$ elements used in ANSYS (solid 185). Solid 185 is an 8-node hexahedral element that has large deformation and large strain capabilities and can be used in 3-dimensional simulation of fully incompressible hyperelastic models. We use the default $\bar{\boldsymbol{B}}$ option that employs "selective reduced integration".

3.7.1.1 Block Subjected to Side Pressure

This example is used to assess performance of near incompressible limit material subjected to a side pressure. Follower forces are used. In this block, displacement is fully constrained in bottom and a side pressure of 2 kPa is uniformly applied to the front left edge. Three meshes respectively consisting of 2, 16 and 128 elements are considered to investigate the convergence. For each mesh, the solution for the two element shapes is obtained to ensure that elements with nonconstant initial element Jacobians perform well (for clarity, the element Jacobian is the volume ratio between the physical volume and the volume in the bi-unit cube in the parent domain, and is different from the Jacobian of the deformation which we have been discussing throughout this dissertation). For each mesh, regular and irregular hexahedra, and each refinement, four cases are run: standard displacement elements with no special treatment of the volumetric deformation, $\bar{\boldsymbol{B}}$ elements with the Jacobian averaged in the reference configuration, $\bar{\boldsymbol{B}}$ elements with the Jacobian averaged in the current configuration and ANSYS solid 185. The displacement results at node A located at (1, 2, 1) meters are obtained for each approach and compared in Table (1). The convergence as a function of the number of elements per mesh is investigated.

Table 1 – Displacement results, in m, obtained at node A, using standard and $\bar{\boldsymbol{B}}$ FEA method for different numbers of elements per mesh

		Standard Method		$\bar{B}$ Method ($\bar{J}$ averaged in reference configuration)		$\bar{B}$ Method ($\bar{J}$ averaged in current configuration)		ANSYS Solid 185	
Element type		Cubes	Irreg.	Cubes	Irreg.	Cubes	Irreg.	Cubes	Irreg.
d-x (m)	2 elements	-0.0001	-0.0001	0.0007	-0.0024	0.0006	-0.0027	0.0003	-0.0029
	16 elements	-0.0021	-0.0026	0.0044	0.0039	0.0045	0.0039	0.0044	0.0039
	128 elements	-0.0030	-0.0035	0.0029	0.0027	0.0029	0.0027	0.0029	0.0028
d-y (m)	2 elements	0.0065	0.0061	0.0970	0.0979	0.0975	0.0985	0.0979	0.0988
	16 elements	0.0154	0.0160	0.0675	0.0677	0.0673	0.0675	0.0678	0.0679
	128 elements	0.0293	0.0294	0.0669	0.0670	0.0667	0.0668	0.0670	0.0671
d-z (m)	2 elements	-0.0798	-0.0800	-0.4674	-0.4646	-0.4717	-0.4690	-0.4658	-0.4631
	16 elements	-0.0938	-0.0944	-0.3087	-0.3086	-0.3091	-0.3090	-0.3085	-0.3084
	128 elements	-0.1279	-0.1281	-0.3260	-0.3259	-0.3263	-0.3262	-0.3259	-0.3258

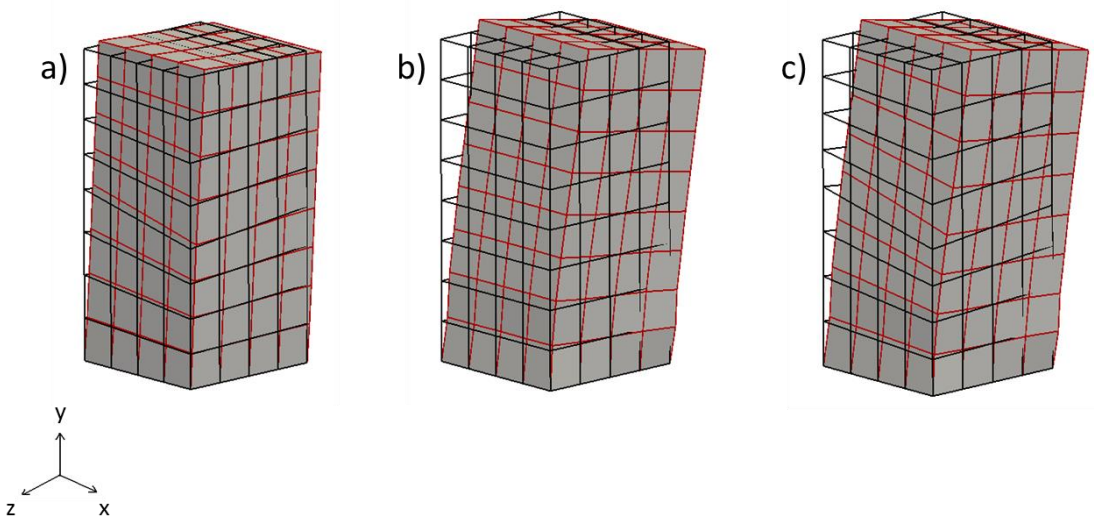

Figure 8 – Deformed shape of an incompressible block subjected to side pressure and fixed bottom displacement obtained from FEA simulation using a) standard 8-node hexahedral elements b) mean-dilational 8-node $\bar{\boldsymbol{B}}$ cubes elements c) mean-dilational 8-node $\bar{\boldsymbol{B}}$ irregular hexahedral elements. In cases (b) and (c), the deformation is shown for $\bar{J}$ averaged in the reference configuration, but all the $\bar{\boldsymbol{B}}$ methods exhibited very similar deformation. The wireframe in black is the undeformed mesh and the solid surface with red wireframe shows the deformed shape of the block.

From the obtained results we can see that average volume $\bar{\boldsymbol{B}}$ elements improve the displacement results over standard methods in the analysis of large deformation nearly incompressible materials. The displacement results obtained from both of the proposed $\bar{\boldsymbol{B}}$ approaches closely agree with ANSYS large deformation $\bar{\boldsymbol{B}}$ method. Convergence of solution with mesh refinement is also observed. The deformed shapes are shown in Figure 8. Since refinement, perturbations in element shape, and type of averaging are satisfied, for remaining examples we run only the irregular, 128 element mesh with the reference-averaged Jacobian.

Table 2 illustrates the evolution of the norm of the residual over the iterations for the last loading step for $\bar{J}$ averaged in reference configuration. This result indicates that the proposed tangent matrix leads to quadratic convergence rate.

Table 2 – Evolution of the residual norm during the last time step in Newton-Raphson iterations with the proposed $\bar{\boldsymbol{B}}$ approach.

Iteration number	Norm of the residual
1	5.1099
2	1.7×10^{-2}
3	2.822×10^{-4}
4	1.657×10^{-8}

3.7.1.2 Block Subjected to Compressive Pressure

This example is presented to assess performance of the proposed $\bar{\boldsymbol{B}}$ approach in simulation of a block with near incompressible limit material properties under pressure. In this block, displacement is fully constrained in bottom and a pressure of 12 kPa is uniformly applied to the top surface. The solution is obtained for 128-elements mesh with irregular hexahedra using

three different element types: standard 8-node hexahedral elements, proposed mean-dilation 8-node hexahedral $\bar{\boldsymbol{B}}$ elements with $\bar{J}$ averaged in the reference configuration and 8-node hexahedral $\bar{\boldsymbol{B}}$ elements employed in ANSYS. Displacement results obtained from three approaches at node A are displayed in Table 3. The displacement results obtained with the proposed $\bar{\boldsymbol{B}}$ approach almost match to the ones obtained using ANSYS trilinear hexahedra. The deformed shape of the block under compression is also depicted in Figure 9.

As illustrated in this figure and the table, displacement results are larger with $\bar{\boldsymbol{B}}$ elements than with standard elements. The two $\bar{\boldsymbol{B}}$ methods are quite comparable. As expected, using the $\bar{\boldsymbol{B}}$ scheme the volumetric locking behavior in the analysis of nearly incompressible materials is relieved.

Table 3 – Displacement results obtained at node A using standard and $\bar{\boldsymbol{B}}$ elements under compressive pressure.

		Standard Method	$\bar{\boldsymbol{B}}$ Method ($\bar{J}$ averaged in reference configuration)	ANSYS $\bar{\boldsymbol{B}}$ Method (Solid 185)
128 elements	d-x (m)	0.0226	0.0176	0.0181
	d-y (m)	-0.0829	-0.1264	-0.1264
	d-z (m)	0.0152	0.0175	0.0170

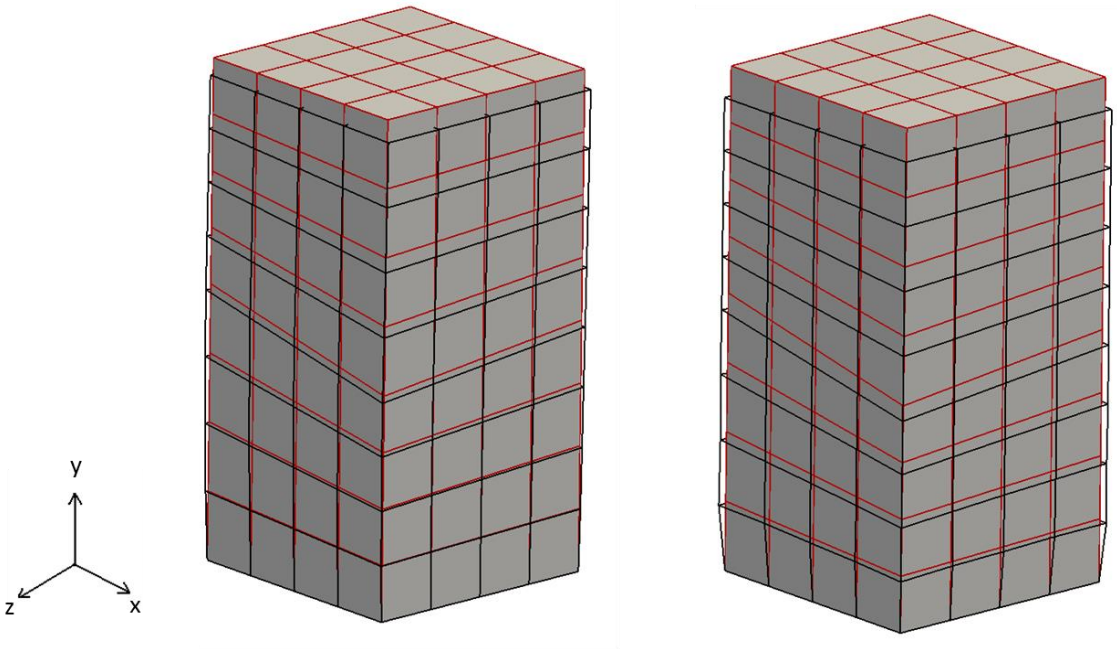

Figure 9 – Deformed shape of an incompressible block subjected to uniform pressure on top and restricted in bottom obtained from FE simulation using standard 8-node hexahedral elements (on the left) and mean-dilational 8-node $\bar{\boldsymbol{B}}$ hexahedral elements (on the right). The solid surface with red wireframe is the undeformed shape and the wireframe in black shows the deformed shape.

3.7.1.3 Block Subjected to Tensile Displacement

In this example, performance of the proposed $\bar{\boldsymbol{B}}$ approach in the simulation of a nearly incompressible block under tension is accessed. The top surface of the block is given a uniform tensile displacement of 0.4 meters and the deformation is fully constrained in bottom. The displacement solution is obtained for a 128-element mesh using 3 different element types: standard 8-node hexahedral elements, proposed mean-dilation 8-node hexahedral $\bar{\boldsymbol{B}}$ elements with the Jacobian averaged in the reference configuration, and 8-node $\bar{\boldsymbol{B}}$ hexahedral elements employed in ANSYS. For standard and the proposed $\bar{\boldsymbol{B}}$ approach, the deformed shape is displayed in Figure 10. The displacements of the block are magnified by a factor of two in order

to better visualize the volumetric locking in standard FEM. In addition to locking, the standard mesh with irregular elements produces a notable asymmetry in the response. Figures 11 and 12 respectively illustrate the distribution of vertical and von Mises Kirchhoff stresses, respectively on the block. Figure 13 depicts the plot of reaction force versus displacement using standard and $\bar{\boldsymbol{B}}$ trilinear elements. As shown in the graph, using standard FEM for nearly incompressible materials, results in greater resistance to external displacement due to the tendency to lock.

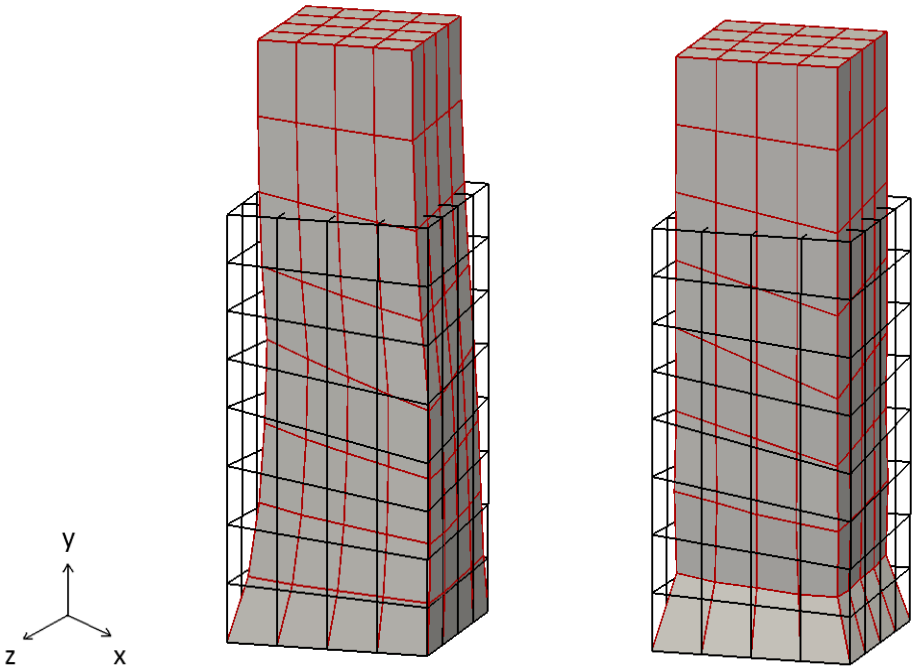

Figure 10 – Deformed shape of an incompressible block subjected to uniform tensile displacement on top and fully restricted displacement on bottom, obtained from FEA simulation using standard 8-node hexahedral elements (on the left) and mean-dilational 8-node $\bar{B}$ hexahedral elements (on the right). The wireframe in black is the undeformed mesh and the solid surface with red wireframe shows the deformed shape of the block, with displacements magnified by a factor of two.

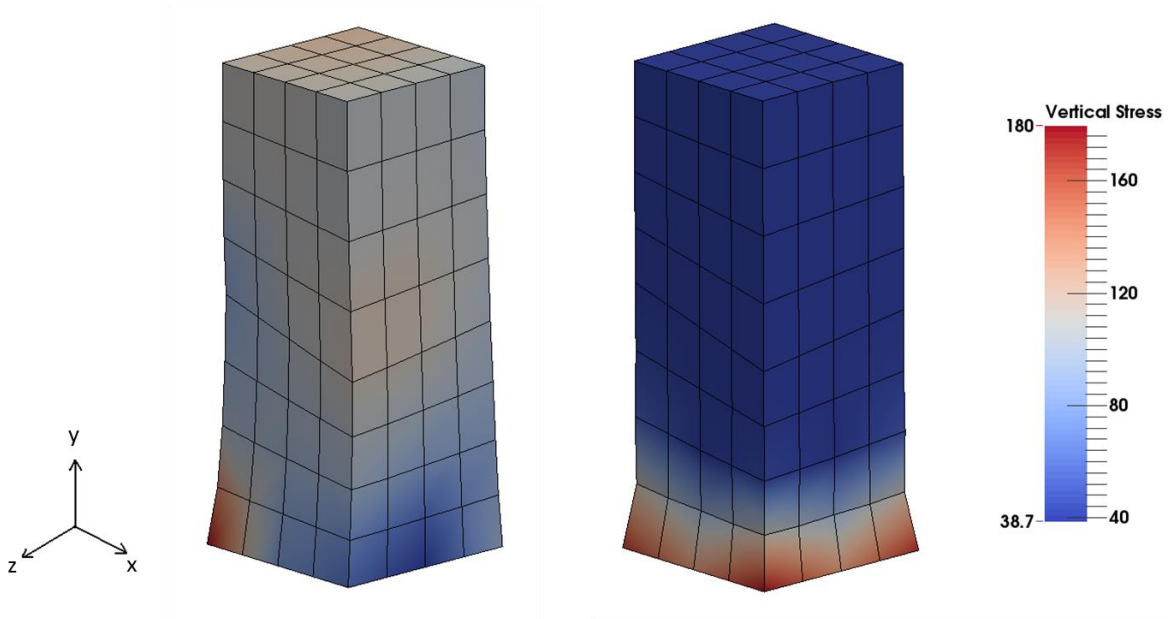

Figure 11 – Distribution of Kirchhoff vertical stress τ_{yy} obtained from FEA simulation using standard 8-node hexahedral elements (on the left) and mean-dilational 8-node $\overline{\boldsymbol{B}}$ hexahedral elements (on the right). The tensile stress is notable higher in the standard example.

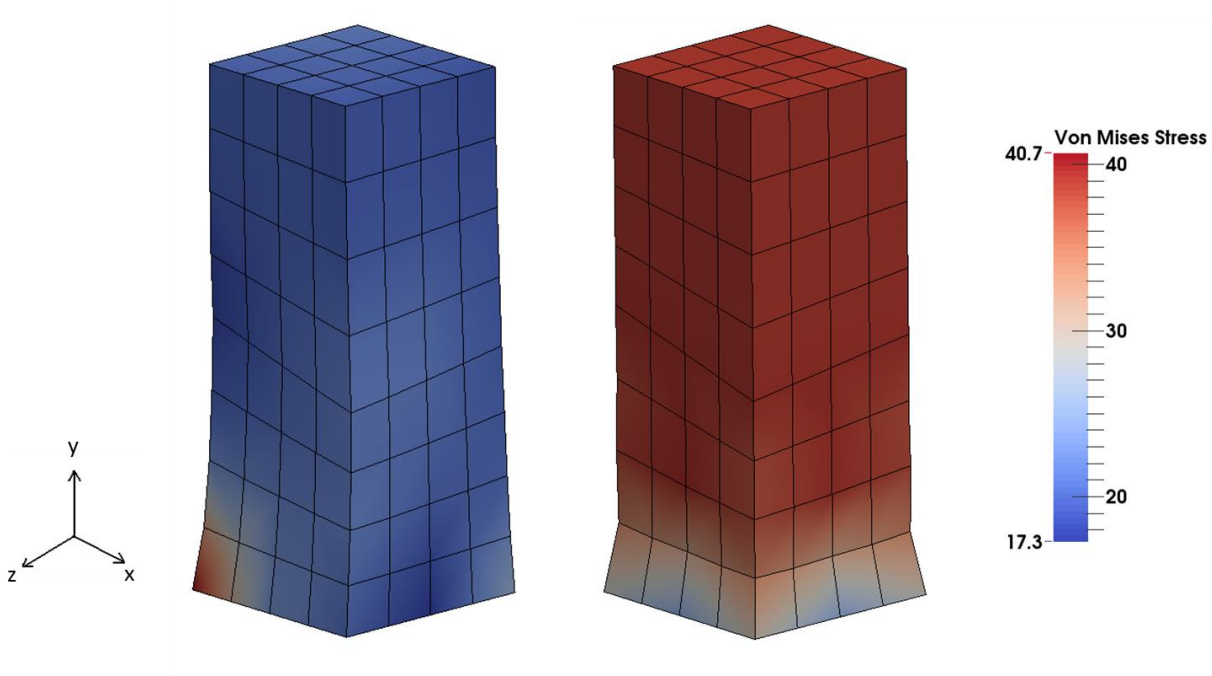

Figure 12 – Distribution of Kirchhoff von Mises stress obtained from FEA simulation using standard 8-node hexahedral elements (on the left) and mean-dilational 8-node $\overline{\boldsymbol{B}}$ elements (on the right).

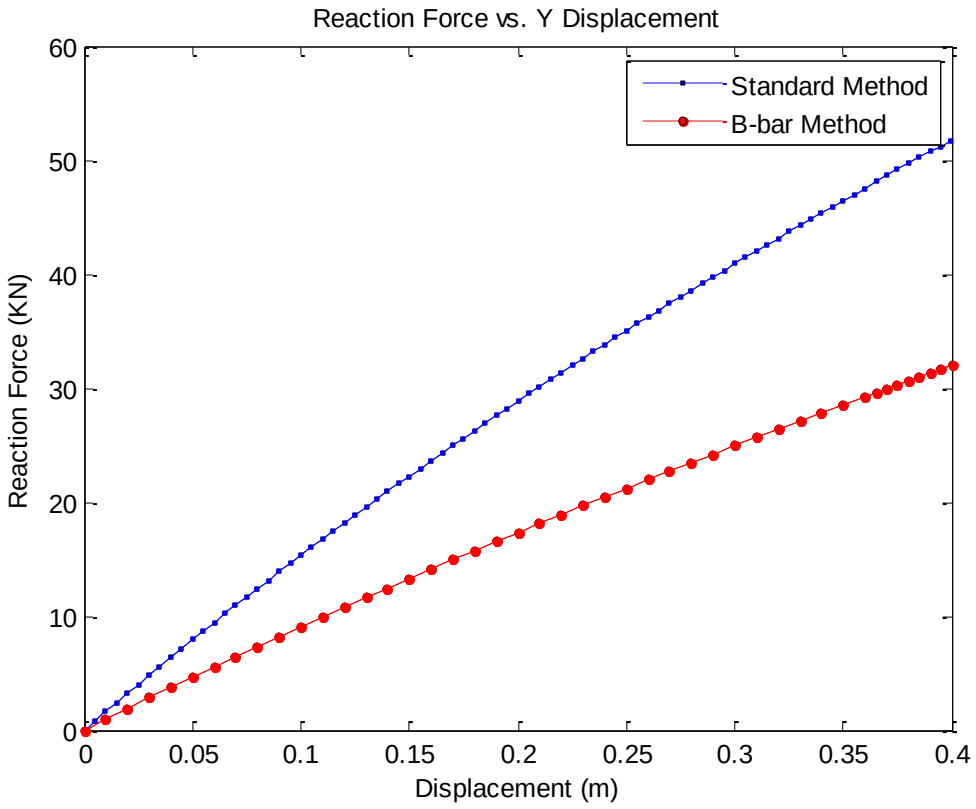

Figure 13 – Plot of the reaction force versus displacement using standard and $\bar{B}$ trilinear hexahedral elements

3.7.2 Incompressible Mouse Cornea Subjected to Pressure

In the final example, the incompressible behavior of a three-dimensional mouse cornea subjected to pressure loading is studied by means of standard and $\bar{\boldsymbol{B}}$ methods. An intraocular pressure of 1.73 kPa is applied to the posterior side of the cornea. The cornea displacement but not rotation is restricted along the center of the cornea edge. While some models of the human cornea use more restrictive boundary conditions on the edges, the mouse cornea is thinner at the edge than at the center, and hence the approximation used here is appropriate. Four different meshes each having 2, 4, 6 and 8 layers of elements through the cornea thickness consisting of

respectively 1360, 2720, 4080 and 5440 hexahedral elements are considered to assess convergence.

The mouse cornea is a nearly incompressible soft biological tissue consisting of five layers of which the stroma is the thickest and stiffest. For simplicity, only the stiffness of the stroma is considered in the constitutive model development. The stroma is composed of oriented and dispersed collagen fibrils embedded in nearly incompressible matrix. The material model used is an anisotropic hyperelastic model adopted from Pandolfi and Holzapfel [12] for the human cornea. The model follows the decomposition of the strain energy function into a volumetric component and isochoric components of oriented fibrils distributed in Neo-Hookean matrix:

$$\Psi\left(J, \boldsymbol{C}^{iso}\right) = \Psi^{iso}\left(\boldsymbol{C}^{iso}\right) + U(J) \tag{53}$$

In which U is the penalty function enforcing incompressibility constraints of the cornea defined as:

$$U(J) = \lambda\, log^2 J \tag{54}$$

where λ is a positive penalty parameter. The isochoric component may be written

$$\Psi^{iso}\left(\boldsymbol{C}^{iso}\right) = \Psi^{iso}_{fibril}(I_1^{iso}, I_4^{iso}) + \Psi^{iso}_{matrix}(I_1^{iso}) \tag{55}$$

$$\Psi^{iso}_{matrix}\left(I_1^{iso}\right) = \frac{\mu_0\,(I_1^{iso} - 3)}{2} \tag{56}$$

$$I_1^{iso} = tr(\boldsymbol{C}^{iso}) \tag{57}$$

$$\boldsymbol{C}^{iso} = J^{-\frac{2}{3}}\boldsymbol{C} \;\; ; \;\; \boldsymbol{C} = \boldsymbol{F}^T\boldsymbol{F}$$

(58)

$$\Psi^{iso}_{fibril}(I_1^{iso}, I_4^{iso}) = \frac{k_1}{2k_2}\{exp[k_2(I_4^{iso^*} - 1)^2] - 1\}$$

(59)

$$I_4^{iso^*} = \kappa\, I_4^{iso} + (1 - 3\kappa)\, I_4^{iso}$$

(60)

$$I_4^{iso} = \boldsymbol{M} \cdot \boldsymbol{C}^{iso} \cdot \boldsymbol{M}$$

(61)

For a given unit orientation vector $\boldsymbol{M}$. Here μ_0 is the shear modulus analogue for the matrix and k_1 and k_2 are materials parameters that define the stiffening effect of the fibrils. The values of the material parameters used in the simulation are given in Table 4.

The unit vector $\boldsymbol{M}$ is the mean orientation of collagen fibrils in the reference configuration. For the human cornea, fibrils are characterized by two mean orientations [12]. However, based on x-ray images, one mean orientation of collagen fibrils is assumed for the mouse cornea [5] and accordingly the quantities involving $I_6^{iso^*}$ are removed from the constitutive equations presented in [12]. The mean orientation is assumed to be horizontal (nasal-temporal) near the center, and circumferential near the edge. There is a transition region in between, where the orientation is linearly interpolated. The dispersion parameter κ describes the ratio of anisotropic fibrils to isotropically distributed ones in the cornea. For the mouse cornea, in the region around the cornea center, we assume that approximately 80% of collagen fibrils are oriented in horizontal direction and 90% have circumferential orientation around the cornea edge. Again, in the transition region a linear interpolation of the two directions is assumed.

Spheres with different radii of curvature for outer and inner surfaces of the cornea result in varying thickness throughout. For the mouse cornea model, a thickness of 0.3 mm at the apex and 0.1 mm at the edge was assumed. An initial cornea height of 0.84 mm and the distance from cornea center to the inner and outer edges of respectively 1.33 mm and 1.39 mm were used. Areas less than 0.45 mm from the center were assumed to have horizontal collagen fibrils, while those outside 1.25 mm were assigned circumferential orientations. The transition zone was in between.

Table 4 – Materials constants assumed for anisotropic and nonlinear FE simulation of mouse cornea.

λ (kPa)	μ_0 (kPa)	k_1(kPa)	k_2
5500	60	20	400

The finite element simulation is performed using the standard 8-node hexahedral elements and the proposed $\bar{\boldsymbol{B}}$ approach, with $\bar{J}$ averaged in the reference configuration. The convergence is studied by increasing the number of layers of elements through the thickness of the mesh. The quantity of interest is the displacement in the vertical direction at the corneal apex.

The results of vertical displacement at the apex versus the number of element layers through corneal thickness are shown in Figure 14. The results obtained with standard 8-node hexahedral elements and with 8-node $\bar{\boldsymbol{B}}$ elements are compared. Using the $\bar{\boldsymbol{B}}$ method, all the displacement values reach a converged solution with fewer layers, and the standard elements appear to exhibit some locking. Figure 15 also illustrates the deformed shape of the cornea using the standard and $\bar{\boldsymbol{B}}$ FE simulation. This example demonstrates that the proposed method functions well even with anisotropic materials.

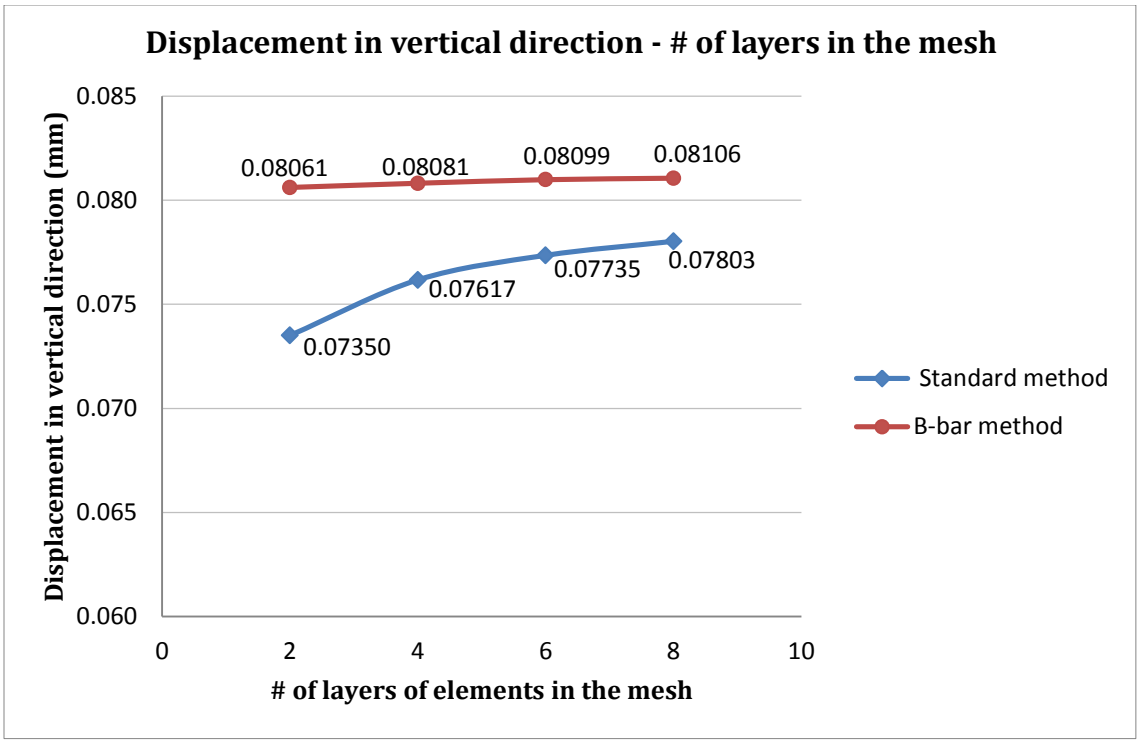

Figure 14 – Vertical displacement at cornea apex versus number of layers of elements through the corneal thickness with standard and $\bar{\boldsymbol{B}}$ elements obtained from nonlinear and anisotropic FEA simulation of mouse cornea subjected to pressure.

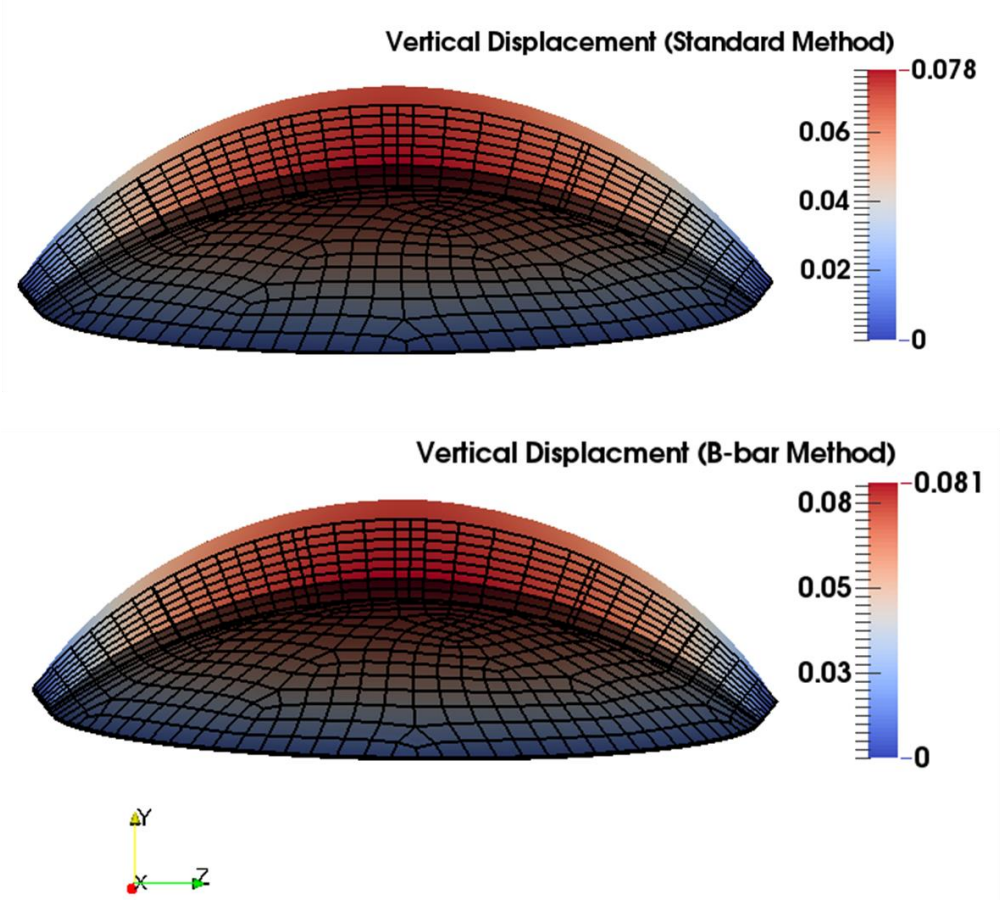

Figure 15 – Vertical displacement mapping of a mouse cornea subjected to pressure obtained from standard and $\bar{\boldsymbol{B}}$ FE simulation (the top and bottom figures respectively) are shown in cross section. The wireframe on the bottom is the undeformed mesh and vertical displacement colored by magnitude is shown on top. The cornea displacement but not rotation is restricted along the center of the cornea edge.

3.8 Conclusion

In this work, we have developed a $\bar{\boldsymbol{B}}$ method for finite deformation nearly incompressible materials, based on an integral average of the volumetric part of the deformation gradient. There is an advantage in such formulations over reduced-order quadrature formulation in that the deformation can be tracked at fewer integration points, saving memory and perhaps, modestly,

computation time. Though not considered here, the advantages are greater in history-dependent materials and multiphysics applications. While integral-averaged $\overline{\boldsymbol{F}}$ methods have been proposed before, there appears to be little in the literature linking a given choice of $\overline{\boldsymbol{F}}$ to the appropriate $\overline{\boldsymbol{B}}$ matrix in these cases, especially for integral formulations. The consistently derived stiffness also appears to be lacking in most of the literature for integral-averaged $\overline{\boldsymbol{F}}$ formulations, though it has been derived reduced-order quadrature formulations.

We have examined two possible choices for the integral averaging of the Jacobian, over the reference configuration and over the current configuration. While there may be some justification for the current configuration as more 'natural', there formulation is more complex. Since the volume change in nearly incompressible materials is small, one does not expect there to be a great difference in the results. This observation is confirmed by numerical examples.

Since the formulation is general, it can be applied to other choices of $\bar{J}$, including reduced integration or logarithmic variations. The formulation is not limited to isotropic materials and can be extended to inelastic materials with some work. Overall, numerical results are similar to existing reduced integration methods.

4 Finite Element Modeling of Spiraling on the Rat Cornea

4.1 Introduction

The cornea is the transparent, anterior layer of the eye that protects the eye and refracts light. It is covered with a tear film that, together with the underlying tissue, provides almost two-thirds of the refractive power of the eye [3]. The curvature and material composition of cornea are largely responsible for its refractive power, and a slight change in its structure remarkably affects the vision function.

In many mammals, including humans, mice, and rats, the cornea consists of 5 layers. From the anterior to the posterior the layers are the epithelium, Bowman's membrane, stroma, Descemet's membrane, and endothelium. The epithelium is the outermost layer of the cornea and consists of cells that can reproduce and regenerate after an injury. The endothelium consists of unrenewable cells that keep cornea hydrated and transparent. Permeability of the endothelium can affect the transparency of the cornea and its ability to function correctly.

The stroma is the thickest layer of the cornea and contributes the majority of the mechanical strength and stiffness of the cornea. It is composed of complex network of collagen fibrils that are distributed in a nearly incompressible and viscoelastic matrix. The collagen fibrils bundle together to form fibers that are stacked parallel to create layers called lamellae. The fibers act as reinforcement to the cornea and provide mechanical strength along their orientation. The collagen fibrils are distributed in all possible orientations in the plane of the cornea but have preferred orientations around the center and the edge [17], [93]. For example, in the human cornea, collagen is distributed along the inferior-superior and nasal-temporal directions around the center and circumferential and radial around the limbus (a region at the corneal periphery

where it meets the sclera). Fibrils exhibit horizontal preferred orientation at the center and circumferential around the edge in the mouse cornea [4], [5]. The arrangements of collagen fibrils play important role in the mechanical strength of cornea. The dominant orientations of the collagen fibrils throughout the lamellae lead to anisotropy of the cornea material.

The cornea has a complex structure with non-uniform thickness throughout. The outer and inner surfaces of the cornea have different curvatures. The central thickness of the human cornea is thinner than the thickness around the limbus. However, in some animals such as mice and rats, cornea is thicker at the center. The curvature and thickness of cornea are largely responsible for the refractive power, and a slight change in corneal structure remarkably affects vision. Hence, studying the mechanical behavior of the cornea is critical in investigating vision and possible disorders.

In vivo and in vitro studies have been performed on the cornea to investigate the biomechanical behavior of the tissue. Recently, numerical techniques such as finite element method (FEM) have been widely used as an effective and noninvasive technique to examine the cornea mechanics. FEM has been implemented to model deformation of the cornea for surgery simulation and refractive surgery planning [23,24]. Some authors [21], [22], [63], used FEM to investigate biomechanical interactions in corneal diseases such as keratoconus in order to better understand the atiology of the illness and offer possible treatment solutions. Discussed in [27], [29], FEM is implemented to study response of the cornea to thermal treatments and disturbances. Some others [6], [30] used FEM to predict the electrical properties of the corneal endothelium and study variations in the permeability. Various applications of FEM in studying corneal biomechanical behavior, surgery predictions, clinical application, investigating related diseases and the response of the cornea to impact have been reviewed [94].

During the generation of an organ primordial cells are allocated to stem cell pools and cells then assort themselves as a result of cell division, cell movement and cell death [8] . These processes operate in a stereotypical manner in a reproducible and conserved manner (Landini & Iannaccone 2000). The resulting distribution of cells can be observed when two or more genetically distinct populations of cells that can be visually distinguished comprise the tissues of an animal. Aggregation chimeras [95] provide a system that allows such visualization. These animals are produced by allowing the individual cells of early embryos of the mouse or rat from two genetically distinct strains to mix prior to implantation. The resulting animal has two genetically distinct lineages and these lineages can be observed microscopically utilizing a variety of markers.

In the cornea, the allocation of epithelial cells is followed by an assortment of cells such that a distinctive pinwheel pattern is observed in both mouse and rat [1], [2]. Moreover, the edges of patches of cells of similar lineages trace out characteristic spiral curves that have been established as logarithmic spirals [2]. The patterns of cell assortment correlate with the distribution of nerves in the cornea [96] implying that there is some global process or force that is responsible for the distribution.

In the same way as for other organ mosaic patterns, it was held that stem cell divisions laying down a trail of progeny as the cornea expanded was responsible for the spiral assortment of epithelial cells. However, a number of fine details of the timing and distribution of cells makes that explanation unlikely [2]. Since the absence of spiral distribution correlates with human disease states and abnormal cornea structure and function, the possibility that biomaterial properties contribute to normal epithelial cell distribution is of significance.

In this work, a large deformation model for the rat cornea that includes the stiffening effect of oriented and dispersed collagen fibrils in incompressible matrix is developed and implemented in a finite element code. The model proposed allows understanding the biomechanical behavior of the rat cornea. The stresses and strains on the surface of the cornea subjected to intraocular pressure are investigated. An algorithm is created that tracks the pathlines of critical shear strains on the cornea surface. The directions of critical strain, in particular, tend to form spiral-like curves that are matched with logarithmic spirals with determined pitch angles. The resulting angles are compared to the pitch angles measured in logarithmic spirals observed on the rat cornea images.

The remainder of this Chapter is organized as follows: Section 4.2 discusses the special assortment of epithelial cell into spiral patterns on the surface of the rat cornea along with observations and measurements of those patterns. In Section 4.3, an anisotropic and large strain finite element model of the rat cornea is developed. This includes creating the 3-dimetional geometric model of the rat cornea and an overview of the restrictions applied on the cornea limbus. The section is followed by a review of the preferred orientation of collagen fibrils in some mammalian cornea as well as assumption of predominant fibril directions on the rat cornea. Also, a structural constitutive formulation including the stiffening effects of collagens in Neo-Hookean matrix is discussed. Section 4.4 focuses on the spiral post-processing which includes the determination of in-plain strains and developing an algorithm for tracking directions of critical strains. In Section 4.5, the numerical simulation results are compared to experimental observations. This Section is followed by a discussion on potential mechanical explanation for spiral formation in Section 6 and finally a conclusion in Section 7.

4.2 Spirals in the Rat Cornea

Rat chimeras were produced as described previously by amalgamation of two 8-cell morulae, one of which ubiquitously expresses enhanced green fluorescent protein (eGFP). Chimeras were perfused with 4% paraformaldehyde in Phosphate Buffered Saline (PBS), a physiological saline solution, and eyes were enucleated and kept in 4% paraformaldehyde at 4°C overnight. Corneas were dissected then relaxed with small radial incisions and imaged on a Zeiss 510 META confocal microscope. Since confocal microscopy uses a variable pinhole in front of the photomultiplier tube, light outside of the focal plane of the objective is blocked from detection. Varying the diameter of the confocal pinhole allows for a change in the thickness of the focal plane. Imaging relaxed corneas, which now lie flat and parallel with the plane of focus, allowed for easy optical separation of epithelium fluorescence without interference or contribution from cells in the stroma or endothelium by simply adjusting the focal plane and its thickness to match that of the epithelium. Because the scale of the corneas is much larger than the field of view of the microscope's objective, multiple images were taken using a computer controlled stage and automatically stitched together in software.

Landmarks on the images were picked along cell lineage boundaries and coordinates of edge landmarks were recorded. Using an initial guess of the spiral center, angle (θ) and radii (r) were calculated for each landmark from this initial center. The polar coordinate data of landmarks were then fit using exponential curves of the form $r = ae^{b\theta}$ which in Cartesian coordinates represent logarithmic spirals.

The exponential equation used to fit the landmark data was used to calculate radii of the fit at the original angles of the landmarks. Total error between the fit and the original landmarks was used to optimize the spiral's center using Microsoft Excel's solver to minimize the total error by

varying the coordinates of the spiral's center position. The radii and angles were then recalculated and refit with exponential curves using this optimized center. A total of 12 edges were analyzed with three edges per image for four images representing four corneas from three rats of ages 10 months, 13 months, and 16 months old and demonstrated in Figure 16.

Figure 17 demonstrates the landmark points and the matching logarithmic spirals in the polar coordinates for cornea C3-1 (r versus θ plot). The variable b of the exponential function fit to the landmarks is related to the curvature of the spiral and therefore is more useful as a unique descriptor of the patch edge. A smaller value of b describes a spiral with a tighter curve with less increase in radius with each increment of angle around the spiral. Likewise, a larger value in b describes a spiral with a looser curve where each increment in angle means a larger change in the radius. A related, but simpler description of each spiral fit is the pitch angle, which represents the angle of inclination between the tangent of the spiral and that of a circle (see Figure 18). Hence a pitch angle varying from zero to $\pi/2$ would be a curve that relaxes from a circle of radius a at a pitch angle of zero to a straight radial stripe at a pitch angle of $\pi/2$. Spiral pitch angles reported for each fit are calculated as $\pi/2 - Atan(1/b)$. A negative pitch angle describes, a spiral which moves clockwise toward the center, while spirals that move counterclockwise inward have a positive pitch angle.

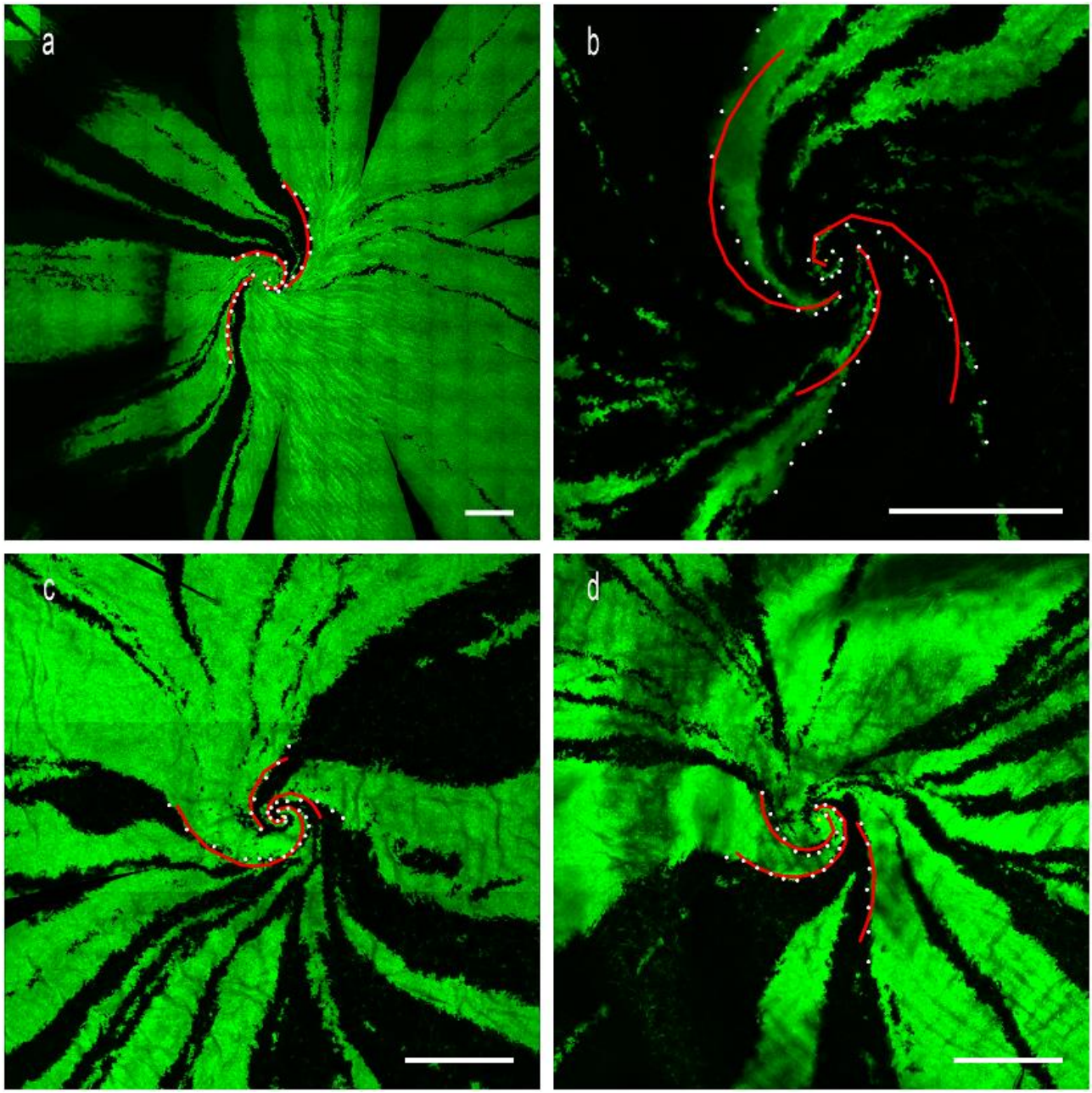

Figure 16 – Confocal images of cornea belonging to a) 10 months rat (C1), b) 13 months rat (C2), c) and d) 16 months rat (respectively C3-1 and C3-2, right and left corneas of the same animal). For each rat cornea, three sets of landmarks are overlaid along the cell boundaries that resemble spiral patterns. These points are fitted with logarithmic spirals (red curves) and the pitch angles are measured. Scale bars on each cornea are 500µm.

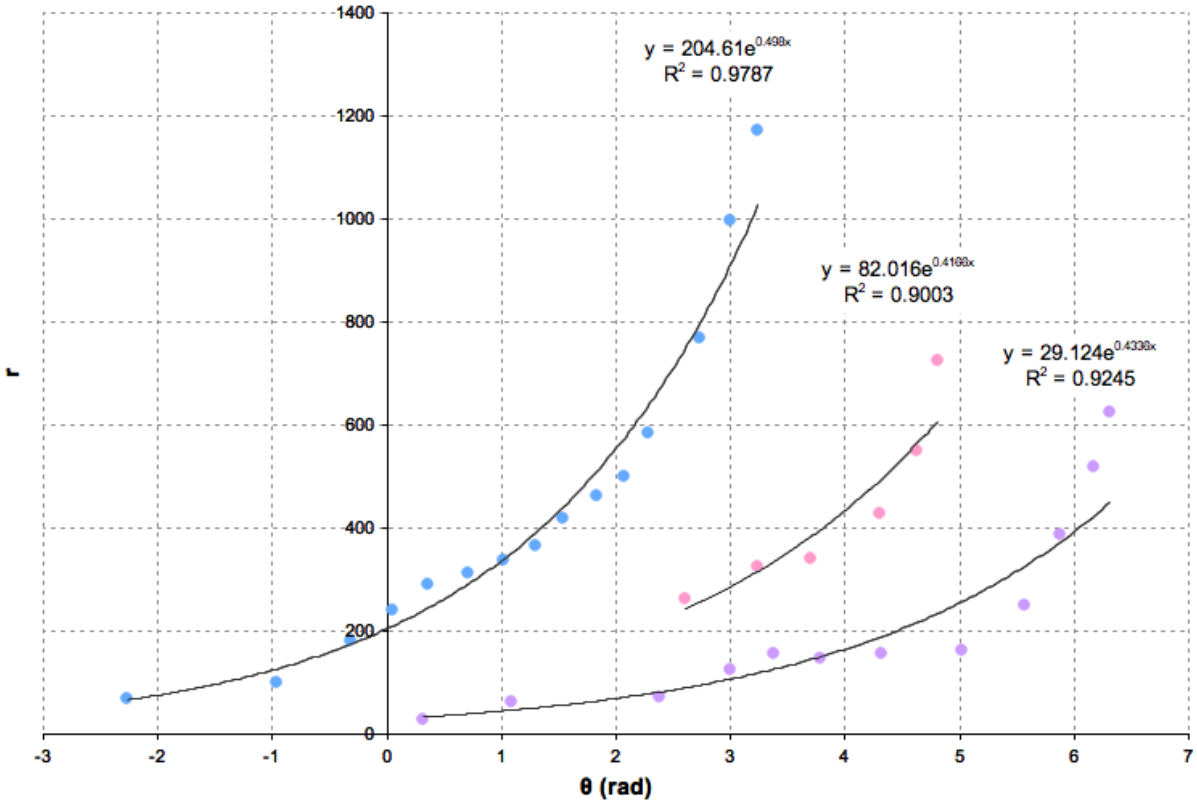

Figure 17 – r versus θ plot of landmark points and the matching logarithmic spirals in the polar coordinates for cornea C3-1

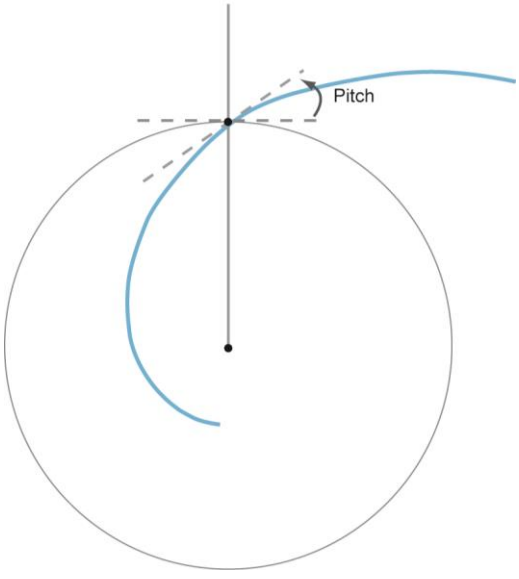

Figure 18 – Schematic representation of pitch angle of a logarithmic spiral

Table 5 – Results of the measurements of the logarithmic spirals fitted to cell lineage boundaries for the four sampling rat corneas

Cornea label	C1			C2			C3-1			C3-2		
Spiral #	1	2	3	1	2	3	1	2	3	1	2	3
b	-0.369	-0.921	-1.225	0.555	0.688	0.636	0.498	0.434	0.417	0.446	1.049	0.413
Pitch angle °	-20.3	-42.7	-50.8	29.0	34.5	32.5	26.5	23.4	22.6	24.0	46.4	22.4

4.3 Rat Cornea Finite Element Model

4.3.1 Geometric Model of the Rat Cornea

The first step in the numerical modeling effort is development of a dimensionally correct cornea model. The rat cornea was cryosectioned and the sections were mounted on slides before confocal imaging. Figure 19 illustrates the provided confocal image of the cross section of a rat cornea. The figure was analyzed to obtain precise measurements (given in Table 6). As seen in the table, the interior and exterior surfaces of the image were fit to spheres of different radii and centers. This leads to non-uniform thickness throughout the cornea being greatest at the apex (nearly 175 microns). The three-dimensional structure of the rat cornea was created based on the obtained measurements (see Figure 20).

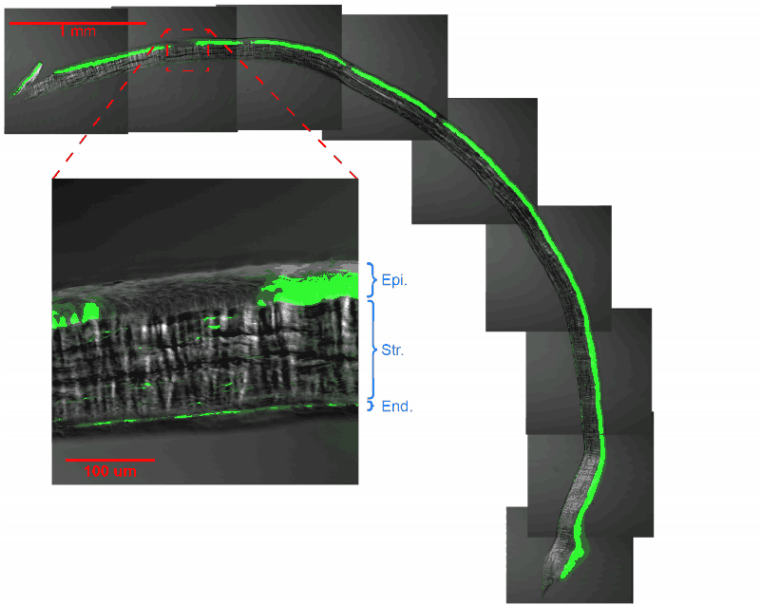

Figure 19 – Confocal image of cross section of a rat cornea used to construct the geometry of the cornea for the finite element model [2]. In the zoomed-in image, Epi. is the epithelium, Str. is the stroma, and End. is the endothelium.

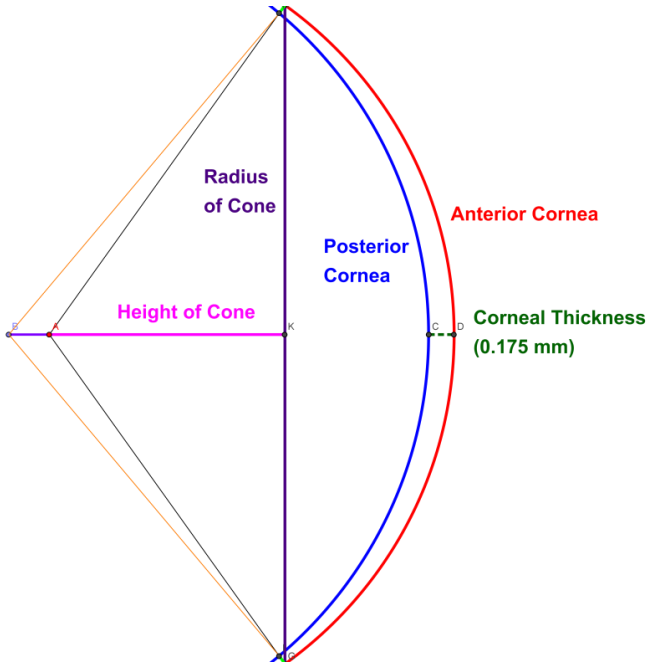

Figure 20 – Two-dimensional representation of geometry used to create the three-dimensional structure of the rat cornea

Table 6 – Measurements obtained for creating 3-dimentional rat cornea structure

Description	Calculation (mm)
Anterior Radius of Curvature	2.767
Posterior Radius of Curvature	2.869
Thickness (at apex)	0.175
Corneal Height	5.223
Height of Cone for model	1.610
Radius of Cone for model	2.250

4.3.2 Boundary Conditions

There is a viscous fluid behind the cornea, the aqueous humor, that exerts pressure, called intra-ocular pressure (IOP), to the cornea. Under physiological conditions, the IOP inflates the cornea and gives it shape. Some authors [44], [45] have modeled the entire eyeball to consider more realistic displacement at the cornea edge. However, the proposed models may be time consuming and not economical. Some others offered an approximate boundary condition, with roller support at the edge inclined at 40˚ with respect to the horizontal axis, to represent the cornea-limbus behavior in human eye [21], [46], [47]. In this work, the displacement boundary is setup to restrict displacement along the center of the cornea edge and allow rotation at the limbus (similar to model proposed by [20]). Since the rat cornea is thinner at the limbus than at the center, the approximation used is appropriate.

A constant intraocular pressure of 1.7 kPa [97] was uniformly distributed to the inner surface of the cornea. In order to maintain the correct direction (normal to the cornea surface)

and magnitude of the pressure with respect to the changing surface, a follower forces technique was applied [92].

4.3.3 Assumptions on Fibril Orientations

The density and orientation of collagen fibrils in the stroma greatly affect the biomechanical behavior of the cornea, and hence studying arrangement of collagens is crucial to developing an accurate model [4]. Recently, X-ray scattering has been successfully used to investigate the predominant orientations of the collagen fibrils in the cornea [4], [17], [93]. In many mammals, collagen fibrils are oriented circumferentially (parallel to the edge of the cornea) in the region around the edge of the cornea. The dominant orientation of collagen is weaker in the central zone of the cornea and differs among mammalian species. For example, collagen fibrils are oriented along the horizontal and vertical directions (superior-inferior and nasal-temporal, Figure 21) in the human cornea. X-ray patterns revealed vertical predominant directions for horse cornea, while showing circumferential preferred orientations in pig and rabbit [4] and horizontal directions in the mouse cornea [5].

Second harmonic generation (SHG) is a useful tool for studying collagen fibril orientations throughout the tissue thickness. The advantage of this approach is that orientation of collagen fibrils can be seen as a function of depth. Latour and coworkers performed SHG microscopy profiles of the rat cornea and provided depth images of collagen directions throughout the cornea thickness [98]. Using the depth profiles of the central cornea, average of the predominant orientations of collagen fibrils in the entire thickness of the rat cornea was calculated. This analysis revealed four preferred directions of collagen fibrils around the center

of the rat cornea: nasal-temporal, superior-inferior, nasal-superior to temporal-inferior, and superior-temporal to nasal-inferior.

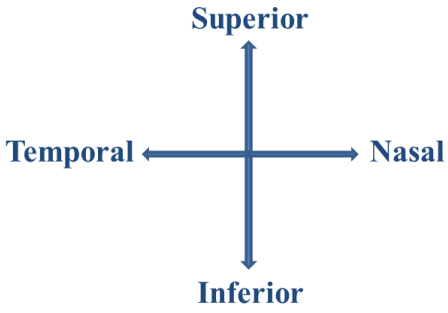

Figure 21 – Schematic of superior-inferior and nasal-temporal directions [17].

While the images obtained only cover a small (about 335 microns) portion of the cornea, these directions are assumed to be predominant throughout the central region of the cornea.

To summarize the discussion on modeling of collagen fibrils in the rat cornea, for numerical purposes, the predominant directions are assumed by introducing three zones in the cornea as follows:

1- Central zone ($r < R_{in}$) :

In the central cornea, it is assumed that collagen fibrils demonstrate four predominant orientations, aligned in 0^o, 90^o, 45^o and 135^o with respect to the horizontal direction.

2- Limbal zone ($r > R_{out}$):

In the region around the edge of the cornea (limbus), it is assumed that collagen fibers are highly aligned in circumferential directions [99]. This is in agreement with preferential circumferential orientation of fibers reported in many other mammals [4].

3- Transition zone ($R_{in} < r < R_{out}$)

In this area the orientation of collagen fibrils between the central and limbal zones is linearly interpolated.

Figure 22 demonstrates the schematic exhibition of the predominant orientations of the collagen fibrils in the three presumed regions of the rat cornea. In this cornea model, $R_{in}\ and\ R_{out}$ are respectively assumed as 0.75 mm and 1.75 mm. These values are approximate, extrapolated from x-ray images of mouse corneas [5], adjusted to the dimensions of the rat cornea.

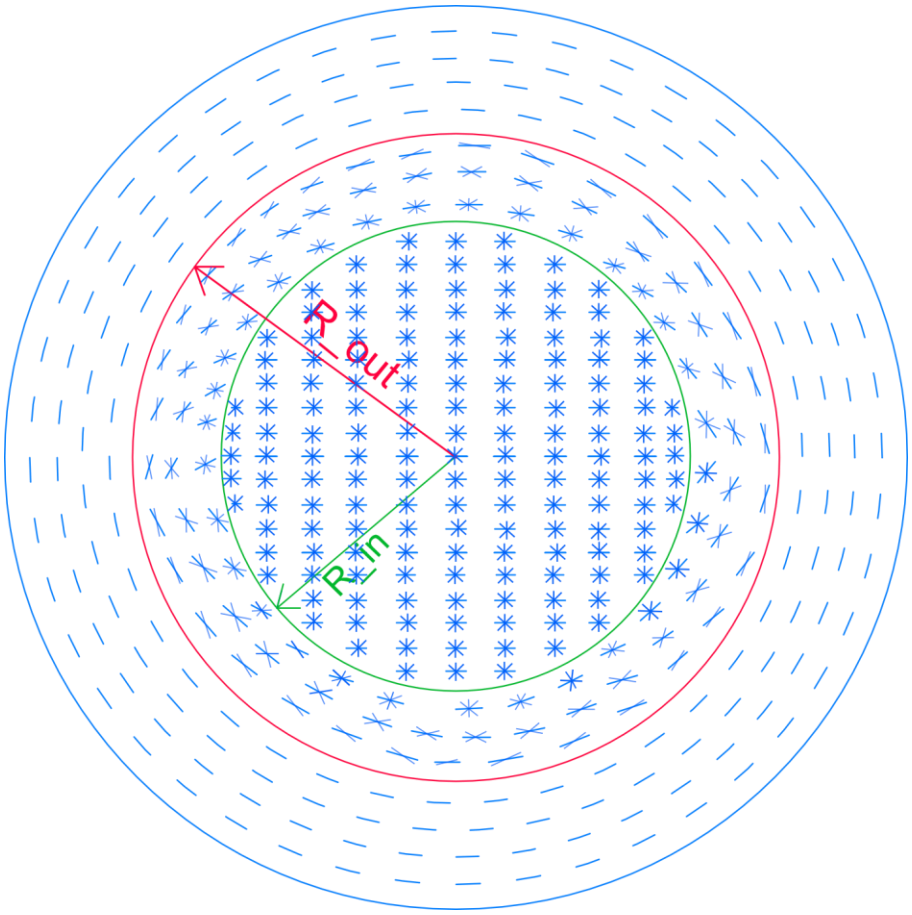

Figure 22 – Schematic presentation of the predominant directions of collagen fibrils assumed in the rat cornea for numerical purposes. The collagen fibrils are assumed to have varying preferred orientations depending on the three regions defined on the cornea: Central area, transition zone and corneal edge.

4.3.4 Collagen Fibril Behavior

The type I collagen forms fibers that run throughout the stroma, reinforcing and stiffening it. These fibers have well-documented nonlinear behavior, becoming stiffer with increasing strain. This behavior has been explained by the fact the molecules unwind at low strains, with relatively low resistance. At higher strains, the molecule cannot unwind further, and the backbone of the molecule is stretched, increasing resistance. Several models have been proposed for stress-strain relationship of collagen fibers ([63], and references therein). In this investigation, we do not model each fiber explicitly, but fit the overall effect of the fibers with an exponential function which stiffens with increasing strain, following [12].

4.3.5 Constitutive Model

The corneal tissue demonstrates highly nonlinear mechanical behavior. This suggests using nonlinear material models for the cornea. In the present work the material model used is an anisotropic hyperelastic model adopted from Pandolfi and Holzapfel [12] for the human cornea. The model follows the decomposition of the strain energy function into a volumetric part and isochoric components of oriented fibrils distributed in Neo-Hookean matrix:

$$\Psi\left(J, \boldsymbol{C}^{iso}\right) = \Psi^{iso}\left(\boldsymbol{C}^{iso}\right) + U(J)$$

(62)

In which *U* is the penalty function enforcing incompressibility constraints of the cornea defined as

$$U(J) = \lambda \, log^2 J$$

(63)

Here λ is a positive penalty parameter, and as it approaches infinity the constraint condition is fully satisfied. A very high value of λ, however, could lead to an ill-conditioned stiffness matrix. *J* is the Jacobian, which is the ratio of the volume in the current configuration to reference configuration (*J = det(**F**)*, ***F*** is the gradient of deformation).

The isochoric component is expressed as combined strain energy density of hydrated matrix (Ψ^{iso}_{matrix}) and anisotropic collagen fibrils (Ψ^{iso}_{fibril}):

$$\Psi^{iso}\left(\boldsymbol{C}^{iso}, M_4, M_6, M_8, M_{10}\right) = \Psi^{iso}_{matrix}\left(I_1^{iso}\right) + \Psi^{iso}_{fibril}(I_1^{iso}, I_4^{iso}, I_6^{iso}, I_8^{iso}, I_{10}^{iso})$$

(64)

Strain energy density of matrix is presented by an incompressible and isotropic Neo-Hookean model as:

$$\Psi^{iso}_{matrix}\left(I_1^{iso}\right) = \frac{\mu_0\ (I_1^{iso} - 3)}{2}$$

$$I_1^{iso} = tr(\boldsymbol{C}^{iso})$$

$$\boldsymbol{C}^{iso} = J^{-\frac{2}{3}}\,\boldsymbol{C}$$

$$\boldsymbol{C} = \boldsymbol{F}^T\boldsymbol{F}$$

(65)

Here μ_0 is the shear modulus analogue for the matrix, I_1^{iso} is the first invariant of the modified right Cauchy-Green tensor $\boldsymbol{C}^{iso}$ which is the deviatoric part of the second order symmetric right Cauchy-Green tensor $\boldsymbol{C}$. Note that $\det(\boldsymbol{C}) = J^2$ and hence $\det(\boldsymbol{C}^{iso}) = 1$.

Strain energy density of fibril associated with four families of collagen fibrils is expressed as:

$$\Psi_{fibril}^{iso}(I_1^{iso}, I_4^{iso}, I_6^{iso}, I_8^{iso}, I_{10}^{iso}) = \sum_{i=4,6,8,10} \frac{k_1}{2k_2} \{ exp[k_2(I_i^{iso^*} - 1)^2] - 1\}$$

(66)

$$I_i^{iso^*} = \kappa\, I_i^{iso} + (1 - 3\kappa)\, I_i^{iso}$$

(67)

$$I_i^{iso} = \boldsymbol{M}_i \cdot \boldsymbol{C}^{iso} \cdot \boldsymbol{M}_i$$

(68)

Here $\boldsymbol{M}_4, \boldsymbol{M}_6, \boldsymbol{M}_8, \boldsymbol{M}_{10}$ (considering i = 4, 6, 8, 10) are the unit orientation vectors defined in the reference configuration that represent the mean orientation of collagen fibrils in the four directions as described earlier. $I_4^{iso}, I_6^{iso}, I_8^{iso}, I_{10}^{iso}$ are pseudo-invariants that describe the stretch in the directions of respectively $\boldsymbol{M}_4, \boldsymbol{M}_6, \boldsymbol{M}_8, \boldsymbol{M}_{10}$.

The dispersion parameter $\kappa \in [0, \frac{1}{3}]$ describes the ratio of anisotropic fibrils to isotropically distributed ones in the cornea.

$$\kappa = \frac{1}{3}(1 - \theta)$$

(69)

Where θ is the percentage of the predominant fibril orientation. For the rat cornea model, in the region around the cornea center, it is assumed in here that approximately 80% of collagen fibrils are oriented in horizontal direction and 90% have circumferential orientation around the cornea edge. In the transition region, linear interpolation of the two values is assumed. This may be written as:

$$r < R_{in} \Rightarrow \theta = 80\%$$

$$r > R_{out} \Rightarrow \theta = 90\%$$

$$R_{in} < r < R_{out} \Rightarrow \theta = \frac{r - r_{out}}{r_{out} - r_{in}} * 0.1 + 0.8$$

(70)

Also, k_1 (stress-like parameter) and k_2 (dimensionless parameter) are material parameters that define the stiffening effect of the fibrils and are determined from mechanical tests. The values of the material parameters used in the simulation are given in Table 7 (based on material parameters suggested in [12]).

Table 7 – Material constants assumed for the rat cornea model (based on data obtained in [12])

λ (kPa)	μ_0 (kPa)	k_1(kPa)	k_2
5500	60	20	400

It is worth noting that k_2 and especially k_1 need not to be the same for all orientations, but we assume it is the case in this model. Clearly, the model is based on limited data and is imperfect. Improvements will be made as more detailed data on the rat cornea is available.

The total stress developed in the cornea due to penalty function, matrix and fibril is expressed as

$$\boldsymbol{S} = \boldsymbol{S}_{penalty} + \boldsymbol{S}_{matrix} + \boldsymbol{S}_{fibril}$$

(71)

where $\boldsymbol{S}$ is the Second Piola-Kirchhoff stress for the cornea in which the constituents are derived from

$$\boldsymbol{S}_{penalty} = 2\frac{\partial U}{\partial \boldsymbol{C}} = 2\,\lambda\,\boldsymbol{C}^{-1}\log J$$

(72)

$$\boldsymbol{S}_{matrix} = 2\,\frac{\partial \Psi^{iso}_{fibril}}{\partial \boldsymbol{C}} = \mu_0\, I_3^{-1/3}\left(\mathbf{1} - \frac{1}{3}\, I_1\, \boldsymbol{C}^{-1}\right)$$

(73)

$$\boldsymbol{S}_{fibril} = 2\,\frac{\partial \Psi^{iso}_{fibril}}{\partial \boldsymbol{C}} = 2\,\sum_{i=4,6,8,10}\; k_1 \exp\left[k_2\left(I_i^{iso^*} - 1\right)^2\right]\left(I_i^{iso^*} - 1\right)\frac{\partial I_i^{iso^*}}{\partial \boldsymbol{C}}$$

(74)

where

$$\frac{\partial I_i^{iso^*}}{\partial \boldsymbol{C}} = I_3^{-1/3}\left[\kappa\left(\mathbf{1} - \frac{1}{3}\,\boldsymbol{C}^{-1} I_1\right) + (1-3\kappa)\left(\boldsymbol{M}\otimes\boldsymbol{M} - \frac{1}{3}\,\boldsymbol{C}^{-1} I_i\right)\right]$$

(75)

In these equations, ***1*** is the second order identity tensor, i.e. $\mathbf{1}_{ij} = \delta_{ij}$, where δ_{ij} is the Kronecker delta. The "⊗" symbol represents the outer product, e.g. for two vectors ***U*** and ***V***, $(\boldsymbol{U} \otimes \boldsymbol{V})_{ij} = U_i V_j$ and for two matrices ***A*** and ***B***, $(\boldsymbol{A} \otimes \boldsymbol{B})_{ijkl} = A_{ij} B_{kl}$.

The fourth order tangent modulus tensor $\boldsymbol{D}$ resulting from the above equations is stated at

$$\boldsymbol{D} = \boldsymbol{D}_{penalty} + \boldsymbol{D}_{matrix} + \boldsymbol{D}_{fibril}$$

(76)

$$\boldsymbol{D}_{penalty} = 4\,\frac{\partial^2 \boldsymbol{U}_{penalty}}{\partial \boldsymbol{C}^2} = 2\mu_0\,\left(-\boldsymbol{L}\;\; log\, J + \;\boldsymbol{C}^{-1}\otimes\boldsymbol{C}^{-1}\right)$$

(77)

in which $\boldsymbol{L} = \frac{\partial \boldsymbol{C}^{-1}}{\partial \boldsymbol{C}}$ is a fourth-order tensor

$$\boldsymbol{D}_{matrix} = 4\,\frac{\partial^2 \Psi^{iso}_{matrix}}{\partial \boldsymbol{C}^2} = \frac{2\mu_0\, I_3^{-1/3}}{3}\,\left(\frac{I_1}{2}\boldsymbol{L} + \frac{1}{3}\, I_1\, \boldsymbol{C}^{-1}\otimes\boldsymbol{C}^{-1} - \boldsymbol{1}\otimes\boldsymbol{C}^{-1} - \boldsymbol{C}^{-1}\otimes\boldsymbol{1}\right)$$

(78)

$$\boldsymbol{D}_{fibril} = 4\,\frac{\partial^2 \Psi^{iso}_{fibril}}{\partial \boldsymbol{C}^2}$$

(79)

$$\boldsymbol{D}_{fibril} = 4k_1 \sum_{i=4,6,8,10} \exp(k_2(I_i^{iso^*} - 1)^2) \{ [1 + 2k_2(I_i^{iso^*} - 1)^2] \frac{\partial I_i^{iso^*}}{\partial \boldsymbol{C}} \otimes \frac{\partial I_i^{iso^*}}{\partial \boldsymbol{C}} + (I_i^{iso^*} - 1) \frac{\partial^2 I_i^{iso^*}}{\partial \boldsymbol{C}^2} \}$$

(80)

where

$$\frac{\partial^2 I_i^{iso^*}}{\partial \boldsymbol{C}^2} = \kappa \frac{\partial^2 I_1^{iso}}{\partial \boldsymbol{C}^2} + (1 - 3\kappa) \frac{\partial^2 I_i^{iso}}{\partial \boldsymbol{C}^2}$$

(81)

$$\frac{\partial^2 I_1^{iso}}{\partial \boldsymbol{C}^2} = -\frac{1}{3} I_3^{-\frac{1}{3}} \{ \boldsymbol{1} \otimes \boldsymbol{C}^{-1} - \frac{1}{3} I_1 \boldsymbol{C}^{-1} \otimes \boldsymbol{C}^{-1} + \boldsymbol{C}^{-1} \otimes \boldsymbol{1} - \boldsymbol{L} \otimes I_1 \}$$

(82)

$$\frac{\partial^2 I_i^{iso}}{\partial \boldsymbol{C}^2} = -\frac{1}{3} I_3^{-\frac{1}{3}} \{ \boldsymbol{M_i} \otimes \boldsymbol{M}_i \otimes \boldsymbol{C}^{-1} - \frac{1}{3} I_i \boldsymbol{C}^{-1} \otimes \boldsymbol{C}^{-1} + \boldsymbol{C}^{-1} \otimes \boldsymbol{M_i} \otimes \boldsymbol{M}_i - \frac{1}{2} I_i \boldsymbol{L} \}$$

(83)

4.3.6 Finite Element Discretization

The geometry is meshed using 8-node hexahedral elements. The elements are arranged in a radial pattern to better capture the spiral patterns near the center.

In the analysis of nearly incompressible materials (such as cornea), very little change in volume is observed under large deformations. Standard 8-node hexahedra are known to exhibit volumetric locking behavior. Many solutions have been proposed to relieve the incompressibility constraints, among which the $\bar{\boldsymbol{B}}$ method is a popular solution to relieve volumetric locking. In these elements, the volumetric part of the strain-displacement matrix, $\boldsymbol{B}$, is replaced by a reduced -order integration or averaged value (Hughes, 1980). In the large deformation regime, the gradient of deformation, $\boldsymbol{F}$, is replaced by a modified deformation gradient $\bar{\boldsymbol{F}}$ to treat incompressibility constraints (called $\bar{\boldsymbol{F}}$ method). Discussed in (Foster and Mohammad Nejad, in

review), we modify the volumetric part of the deformation gradient using an averaged integral. The integral-averaged $\bar{\boldsymbol{F}}$ approach leads to a so called $\bar{\boldsymbol{B}}$ element.

The proposed averaged-volume trilinear $\bar{\boldsymbol{B}}$ elements (with Jacobian averaged in the reference configuration) were used in meshing the structure of the rat cornea model. The mesh was next refined throughout the thickness to assess convergence. A radial mesh being finer at the center and coarser around the edge for better tracking of spirals in the central area was generated. Four different meshes each consisting of 4, 6, 8 and 10 layers of elements respectively having 1792, 2988, 3584 and 4480 hexahedral elements were investigated.

4.4 Spiral Post-Processing and Measurements

4.4.1 In-plane Strain Determination

The initial assumption taken is that the epithelial cells align to the direction of maximum shear strain vectors as they migrate toward the center of the cornea. Here, determination of these vectors is briefly discussed.

The strain used in the finite element model is the Eulerian logarithmic strain defined as

$$\boldsymbol{\varepsilon} = log\ (\sqrt{\boldsymbol{F}\boldsymbol{F}^T}) \tag{84}$$

To analyze the effects of the deformation of the stroma on the epithelium above, we restrict ourselves to the strain $\hat{\boldsymbol{\varepsilon}}$ in the plane of the cornea surface. If $\hat{\varepsilon}_1$ and $\hat{\varepsilon}_2$ are the principal strains in the surface, then the maximum shear strain is

$$\hat{\varepsilon}_{12} = \frac{\hat{\varepsilon}_1 - \hat{\varepsilon}_2}{2} \tag{85}$$

And if $\hat{\boldsymbol{n}}_1$ and $\hat{\boldsymbol{n}}_2$ are the principal strain direction vectors belonging to respectively $\hat{\varepsilon}_1$ and $\hat{\varepsilon}_2$, the two perpendicular maximum shear strain direction vectors are defined as

$$\hat{\boldsymbol{t}} = \frac{\hat{\boldsymbol{n}}_1 \pm \hat{\boldsymbol{n}}_2}{\sqrt{2}}$$

(86)

The resulting shear strain vectors point along the surface of the cornea.

As previous work on mouse cornea [10] demonstrated, directions of maximum shear strain do not always fit observed spirals well. Hence, we examine in this work a linear combination of shear and tensile strains creating critical directions, which is fully justified in Section 6. The critical direction may be written as a combination of the principal in-plane directions.

$$\hat{\boldsymbol{l}} = \frac{\hat{\boldsymbol{n}}_1 \pm c\,\hat{\boldsymbol{n}}_2}{\|\hat{\boldsymbol{n}}_1 \pm c\,\hat{\boldsymbol{n}}_2\|}$$

(87)

In this equation, c >1 indicates a positive effect of tension on this critical direction. The larger the value of c, the greater the effect of tension over shear. Including this factor in the proposed path determination algorithm leads to a curve that can be fitted with logarithmic spiral having smaller pitch angles, similar to the spirals observed on the mouse and rat corneas.

4.4.2 Pathline Determination

To quantify the spiral patterns on the cornea surface created by the vector field critical strains, an algorithm was devised to track the pathlines of in-plane critical strain directions. In this procedure, starting from an arbitrary point on any element, critical strain vectors are traced to the adjacent element.

Within each element, the spiral pattern is approximated using a straight line by averaging the strain, requiring only the determination of two endpoints in each element in space (refer to Figure 23). The endpoints are found by matching the equation of the critical strain direction in the element to the equations of the element edges (similar to the approach used in [100], [101]). The endpoints are next connected together toward the center of the cornea, forming a curve that resembles spiral patterns. As the mesh refinement is performed, more accurate spiral-like curves are obtained. Since there are two critical strain directions, we select the one that matches the spiral we wish to fit, either clockwise inward or counter clockwise inward.

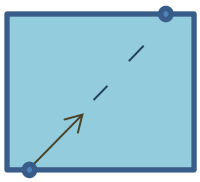

Figure 23 – Schematic 2-dimensional representation of the approach used for finding the endpoints at each element

Observed in the x-ray images of the rat cornea, spiral patterns mainly tend to form around the central cornea zone. Therefore, for simulation purposes, cornea mesh was specifically refined around the central region in order to capture the spirals there more accurately.

4.5 Results and Measurements

To verify convergence, two quantities are examined, the maximum displacement in the vertical direction, and the maximum logarithmic shear strain. These are shown in Table 8. As observed in the Table, the maximum displacement converges rapidly toward a single value. The maximum shear strain also converges, but with a slower rate as expected.

Table 8 – Convergence rates studied for maximum vertical displacement and maximum shear strain obtained from FE simulation. The maximum vertical displacement converges more rapidly.

# of layers in the mesh	# of elements in the mesh	Maximum displacement in vertical direction (mm)	Maximum shear strain
4	1792	0.23603	0.10705
6	2688	0.24124	0.10746
8	3584	0.24126	0.10772
10	4480	0.24127	0.10788

4.5.1 Comparison of Observed Spirals and Simulation Results

As explained earlier, four adult rat corneas (two from the same rat) were sectioned and imaged with confocal microscopy. Landmark points were overlaid onto the cell boundaries that resemble spiral patterns. These points were fitted with logarithmic spirals and the spiral pitch angles were measured. For each rat cornea, the logarithmic spiral with median pitch angle was selected to be compared to the finite element simulation results.

The pathline determination algorithm was performed to trace the pathlines of in-plane critical strain directions obtained from finite element simulation. For each rat cornea, these directions were tracked starting from a point close to the beginning point of the logarithmic spiral fitted to the observed patch edges. However, the pathlines of maximum shear strains did not fit the observed logarithmic spirals well in all of the sampling corneas. In some cases, in order to find the best fit to the observed logarithmic spirals, the pathline tracking algorithm was modified by considering a combination of the effect of shear and tensile strains. The details will be discussed in Section 4.6. Table 9 demonstrates the constants used to fit the simulation curves

to the logarithmic spiral observed at each cornea and the measured spiral pitch angles. Figures 24-27 demonstrate the landmark points overlaid onto the cell boundaries, the logarithmic spirals fitted to the landmarks and spiral-like curves obtained from numerical simulation respectively on rat corneas C1, C2, C3-1 and C3-2.

Table 9 – For each rat, the pitch angle of the logarithmic spiral observed on the cornea is measured. The constant (c) is selected to fit the simulation curve to the observed spiral.

Cornea Label	Pitch Angle (°)	c
C1	-42.7	1.00
C2	32.5	1.45
C3-1	23.4	2.00
C3-2	24.0	2.00

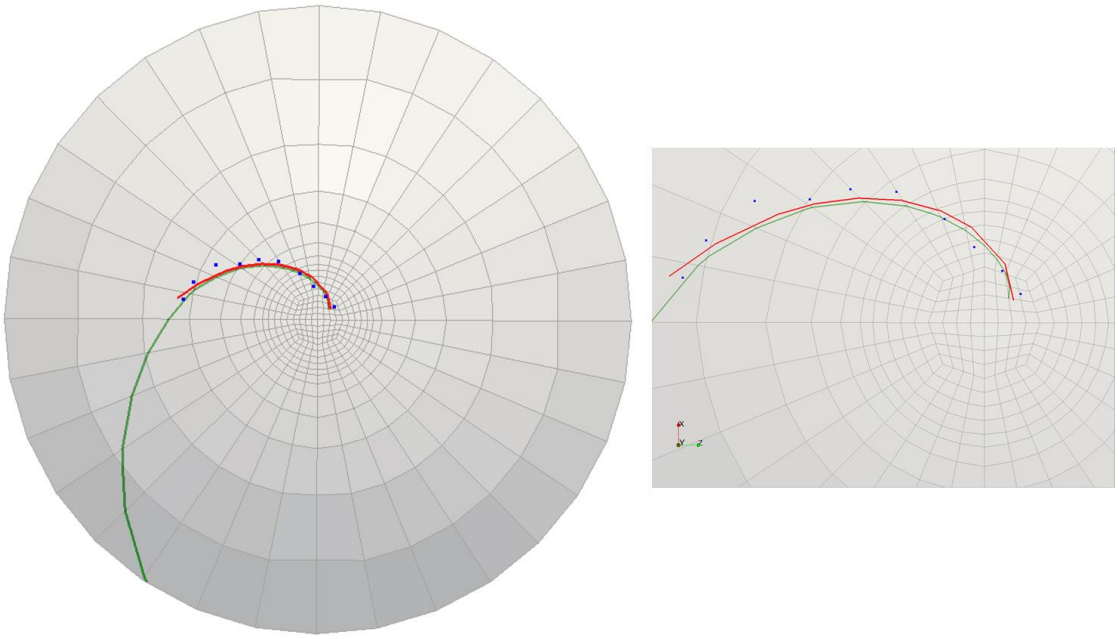

Figure 24 – Cornea C1: Landmark points overlaid onto the cell boundaries are shown in blue, the logarithmic spiral with -42.7° pitch angle fitted to the landmarks is shown in red and green curve is obtained from FE simulations (c=1). The figure on the right demonstrates the zoomed-in view of the central part of the rat cornea on the left.

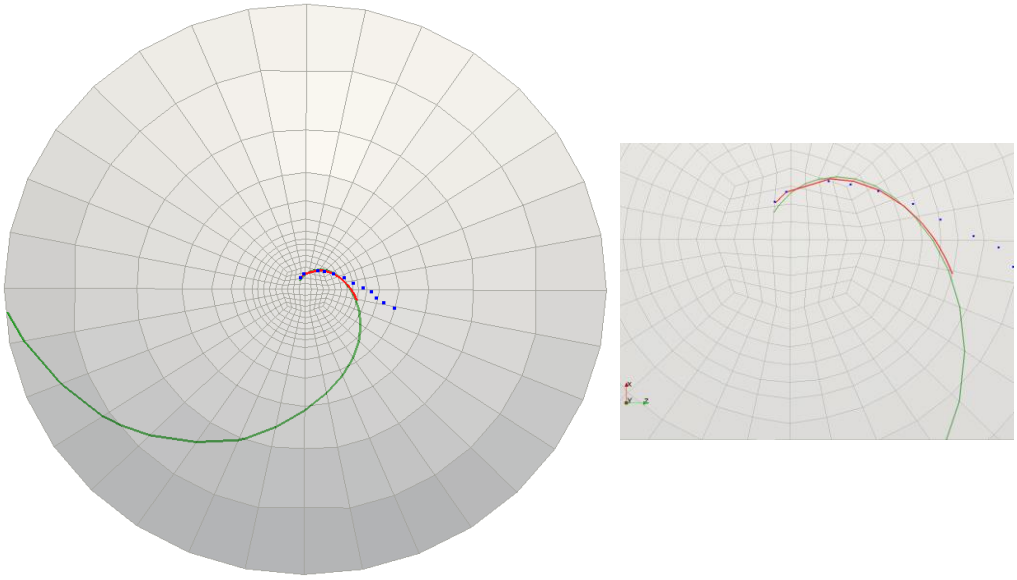

Figure 25 – Cornea C2: Landmark points overlaid onto the cell boundaries are shown in blue, the logarithmic spiral with 32.5° pitch angle fitted to the landmarks is shown in red and green curve is obtained from FE simulations (c=1.45). The figure on the right demonstrates the zoomed-in view of the central part of the rat cornea on the left.

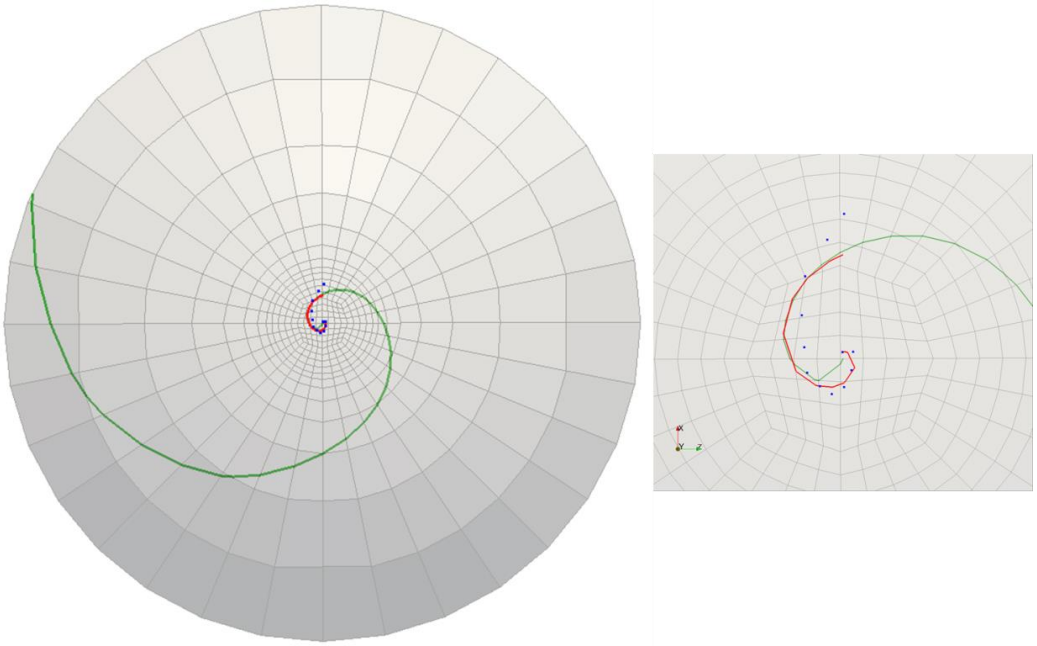

Figure 26 – Cornea C3-1: Landmark points overlaid onto the cell boundaries are shown in blue, the logarithmic spiral with 23.4° pitch angle fitted to the landmarks is shown in red and green curve is obtained from FE simulations (c=2). The figure on the right demonstrates the zoomed-in view of the central part of the rat cornea on the left.

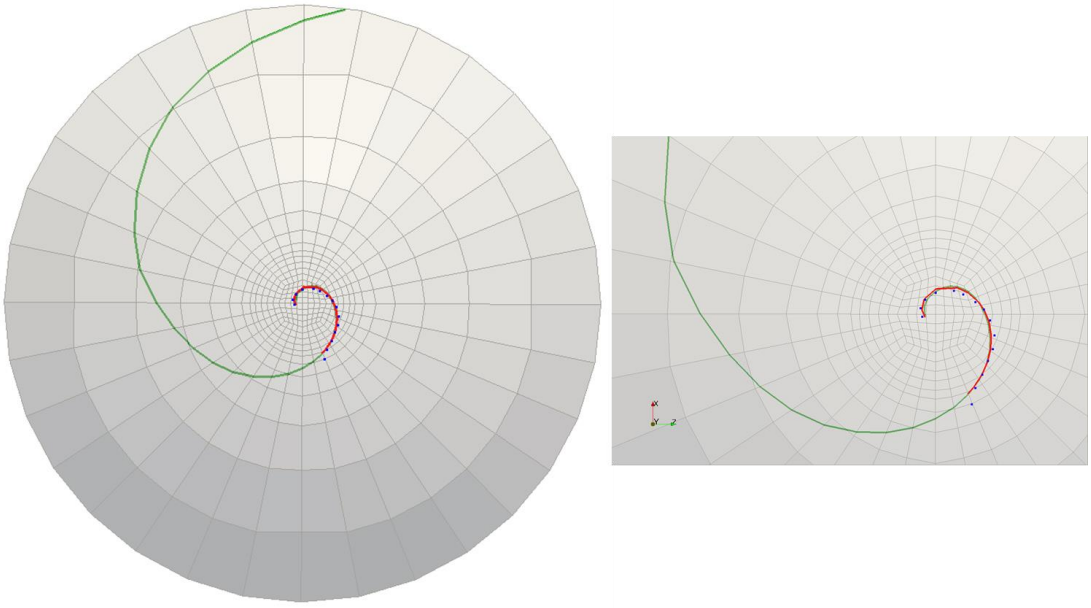

Figure 27 – Cornea C3-2: Landmark points overlaid onto the cell boundaries are shown in blue, the logarithmic spiral with 24° pitch angle fitted to the landmarks is shown in red and green curve is obtained from FE simulations (c=2). The figure on the right demonstrates the zoomed-in view of the central part of the rat cornea on the left.

4.6 Discussion

In young rats, the cornea inflates as the IOP increases. Though we have not explicitly modeled it, the cornea may also grow during this phase. The resulting deformations are likely similar. In either case, the epithelial cells must move and grow to maintain coverage of the cornea. The cells do not appear to fracture, and hence must stretch and slide past each other as they move to cover Bowman's membrane. The shear strains in the membrane facilitate this kind of sliding. As the cells slide past, like cells tend to have stronger adhesion ([102] and references therein), and tend to stick as unlike cells continue to slide past.

However, pathlines of maximum shear strain do not fit observed spirals well in most cases. We hypothesize that normal strain influences the ability of cells to slide with respect to each. Such behavior is observed in soils and other materials, though typically the normal component is compressive in these cases. In the cornea, larger tension on cell boundaries, tending to pull the cells apart, may facilitate sliding.

While there is discussion of both tensile and shear deformation in the cell in tissue mechanics literature, there is little discussion of how normal strain might influence shear deformation. The deformation of epithelial cells under tension in [103] suggests, however, the tension-facilitated shear may be at work in cell deformation. Before fracturing in tension, the cells exhibit noticeable distortion. In pure shear sliding, which is sometimes seen in metals, the slip planes would be at 45° from the maximum tensile stress. In the figures presented, the angle appears lower, approximately 21° from the plane of maximum principal stress. This suggests that a mix of shear and tension lead to the critical slip direction in these cells.

Unlike the stroma, the epithelium is more or less isotropic, at least in the plane of the cornea surface. Hence stresses and strains are coaxial. If we consider a linear effect of tension on shear motion, then motion most likely occurs, overall, on the plane of maximum

$$| \tau | + a \sigma$$

(88)

where τ is the shear stress and σ is the normal stress. Using Mohr's circle (Figure 28 – a), we can see that the critical direction is $\pm\left(\frac{\pi}{4}-\frac{\alpha}{2}\right)$ from the direction of the smaller principal strain, where tan α = a. Therefore, as shown in Figure 28 – b the critical direction

$$l = sin\left(\frac{\pi}{4}-\frac{\alpha}{2}\right) n_1 \pm cos\left(\frac{\pi}{4}-\frac{\alpha}{2}\right) n_2$$

$$l = \frac{n_1 \pm cot\left(\frac{\pi}{4}-\frac{\alpha}{2}\right) n_2}{\left\| n_1 \pm cot\left(\frac{\pi}{4}-\frac{\alpha}{2}\right) n_2 \right\|}$$

(89)

Hence

$$c = cot\left(\frac{\pi}{4}-\frac{\alpha}{2}\right) = \tan\left(\frac{\pi}{4}+\frac{\alpha}{2}\right) = a + \sqrt{1 + a^2}$$

(90)

The last identity comes from some trigonometric manipulation. Since we are more concerned with directions in this study, we will focus on manipulating *c* rather than *a*. However, a linear relationship between the effect of normal and shear strain leads to a critical direction that is a linear combination of the two principal directions.

This evidence for this type of model is, of course, preliminary. The cells in [103] are not corneal epithelial cells. The relationship between normal and shear strain may be nonlinear,

though a linear model may be a good first approximation. Cell boundaries have fairly random orientations, and hence the normal and shear stress vary across a line of moving cells. In this work, we are attempting to understand the tissue-level slip patterns of the cells, but multiscale efforts may reveal the variation that different initial configurations create with regard to the patterns observed. In this regard, the cell motion over time may have a significant effect. On a planer surface under uniaxial tension, the 45° slip lines would only become apparent after large deformations. Similarly, motion of cells in the cornea creates an evolution of patterns that has not been fully investigated. Although the sample size here is quite small, the spirals seem show a tendency to tighten over time. This type of behavior makes sense as the cells continue to arrange of time. Further investigation is necessary to confirm this observation. Cell growth, division, and death along with the viscous behavior of the cell matrix, may also influence the deformation patterns.

It is worth noting that, with or without a tensile component, there are two critical slip directions. If the majority of cells throughout the cornea tend to slip in one dominant direction, clockwise or counterclockwise, the cells will spiral (see Figure 29 a). Presumably, there is no preferred direction and initial perturbations determine the orientation of the spirals. If cells in one section start to slide in a different direction, and cells in a different part of the cornea start to slide in the other, different patterns, such as horseshoes, can emerge (Figure 29 a). Such patterns have been observed in corneas.

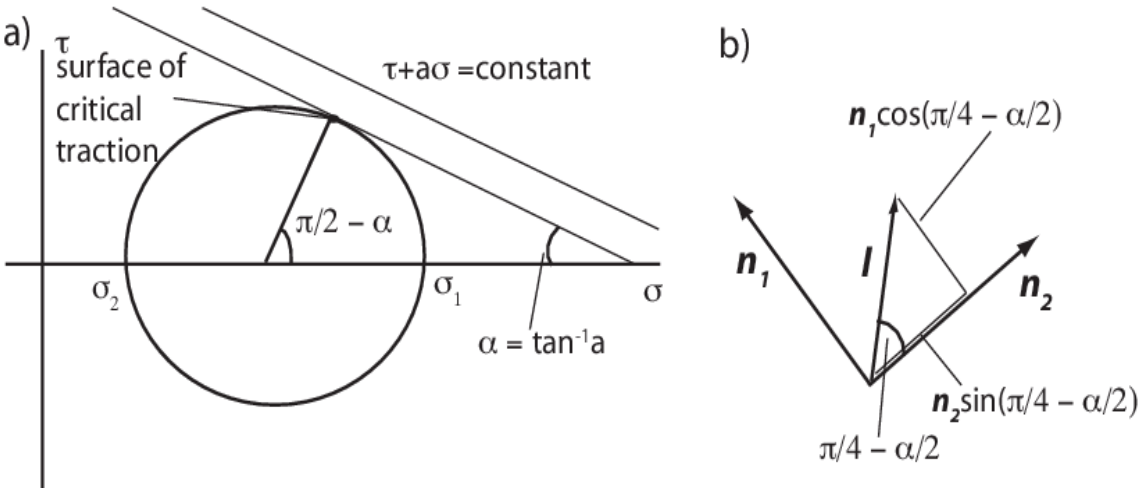

Figure 28 – a) Mohr's circle showing the critical surface traction, located at $\frac{\pi}{2} - \alpha$ from the major principal strain on Mohr's circle, or half that in physical space. b) Critical direction in physical space as a function of the principal directions.

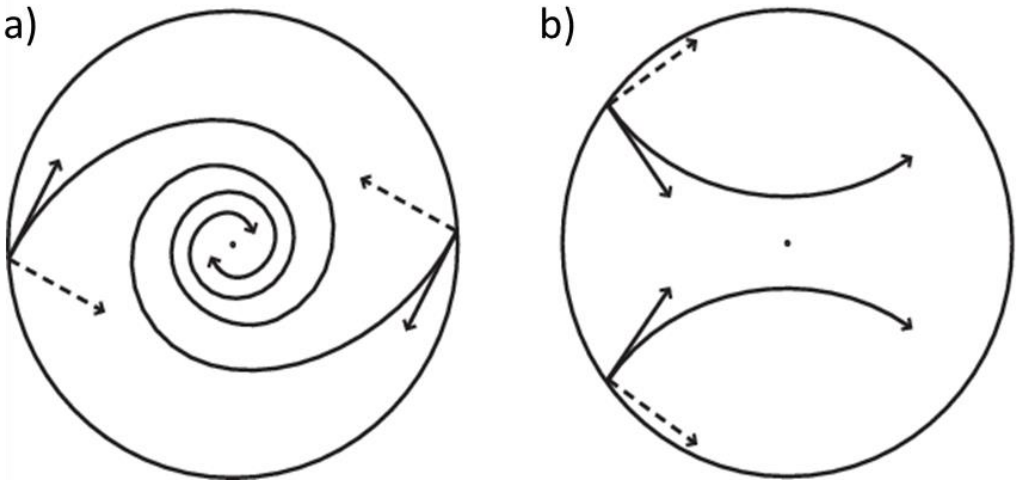

Figure 29 a) If the majority of cells in all parts of the cornea tend to slip in one dominant direction, clockwise or counterclockwise, the cells will spiral. b) If cells in one section start to slide in a different direction that other cells, different patterns, such as horseshoes, can emerge

4.7 Summary and Conclusion

During the generation of an organ, stem cells assort themselves into patterns as a result of cell division, cell movement and cell death. These processes operate in a typical reproducible and conserved manner. If the organ is comprised of two or more genetically distinct groups of cells, the distribution of cells can be visually distinguished. In some mammalian corneas such as mice and rats, the allocation of epithelial cells is followed by a special assortment of cells under both normal and diseased conditions. The edges of patches of epithelial cells having similar lineage often form distinctive spiral patterns that can be visualized. Studying the generation of such patterns is important as it can reveal greater understanding of corneal function and possible disorders. This dissertation proposes a framework for explaining the special arrangement of epithelial cells into spiral patterns due to the effect of stresses and strains on the cornea.

Confocal images of four adult rat corneas (two from the same rat) demonstrating spiral patterns were provided. Landmark points were overlaid onto the patch edges. Logarithmic spirals were fitted to the points and the spiral pitch angles were measured. For each rat cornea, the logarithmic spiral with median pitch angle was compared to the finite element simulation results.

It was assumed in this work that shear strains in the tissue facilitate the sliding of epithelial cells past each other and cause special assortment of cells into spiral patterns. An algorithm was devised to track the pathlines of critical strain directions obtained from finite element simulation. The resulting curve matched the observed logarithmic spirals well for sampling rat cornea C1. The algorithm was modified considering a combination of the effect of shear and tensile strains for other rat corneas samples. In the corneas C2, C3-1 and C3-2, a proper combination of shear and tension were selected to fit well to the observed spirals. Interestingly, the selected combination was the same for cornea C3-1 and C3-2 as they both

belong to one rat. This confirms that in the same animal, corneal epithelial cells form similar patterns. However, sometimes the patterns could be clockwise in one cornea and counter clockwise in the other.

This work presented a framework for studying the development of spiral patterns in the rat epithelium. Using the finite element method as a basis, this framework included a detailed structural and constitutive representation of the rat cornea. A continuum finite deformation model considering material and geometric nonlinearity of collagen fibrils and incompressibility of hydrated matrix was developed. The proposed model included a $\bar{\boldsymbol{B}}$ method to treat incompressibility constraints of the cornea in the large deformation regime. The model involved the effects of preferentially oriented and dispersed collagen fibrils throughout the rat stroma. Based on the simulation results, a mesh of ten layers achieved converged values of strain, though the displacement convergence was much faster. Good agreement between the simulation curves and logarithmic spirals fitted to confocal images of the rat cornea were obtained. This supported the proposed assumption that shear and tensile strains facilitate sliding of epithelial cells.

There are some factors affecting the motion of epithelial cells that were not considered in our numerical model. Variations in the spiral development due to the cell growth and division in the organ were not included in our model. The spiral may also evolve with age. Dynamic motion of the cornea caused by the changing intraocular pressures was lacking in our model. The material parameters used in this rat cornea model were based on limited data, and improved understanding of the structure of the rat cornea would modify results mildly.

A future direction is to use the change in shape of the surface of the stroma as an input condition to model the rearrangement of epithelial cells over time. Cellular finite element models of tissues exist that account for the adhesion of the membranes, the viscosity of the cellular fluid,

and even cell growth and division. More detailed models of the shear and tensile behavior of cell-to-cell adhesion would need to be developed, as well as the attachment to the basement membrane.

5 Conclusions and Future Work

5.1 Conclusions

Finite element analysis is a useful technique for finding approximate solutions to partial differential equations in complex problems. FEA has potential usefulness to simulate a wide range of biological structures. In this dissertation, different application of FEA in investigating biomechanical behavior of the cornea was reviewed. This included reviewing various applications ranging from predicting refractive surgeries to studying corneal diseases and simulating eye impact and trauma.

This dissertation focused on presenting a framework for numerical modeling of the cornea to investigate tissue mechanics. Using the finite element method as a basis, this framework considered the microstructure of the cornea, in particular, collagen fibrils that provide the cornea with unique optical and mechanical properties. An anisotropic, finite-deformation model of the cornea considering stiffening effect of collagen fibrils in a nearly incompressible matrix was developed.

Low-order finite elements perform poorly in the analysis of nearly incompressible materials. Higher order elements can treat this; However, they do not behave optimally and might be computationally expensive. Many solutions exist to relieve this constraint, among which the $\overline{\boldsymbol{B}}$ method has been highly popular due to the fact that it retains a displacement-only approach to the solution to the problem. In $\overline{\boldsymbol{B}}$ elements, the volumetric part of the strain-displacement matrix is replaced with a reduced-order integration or averaged value. The reduced interpolation order of the volumetric term reduced the number of constraints, treating the locking. The averaged volumetric approach has the advantage that deformation is tracked at

fewer integration points than reduced-order quadrature formulations. In this dissertation, a $\bar{\boldsymbol{B}}$ method was developed to prevent the volumetric locking associated with incompressibility constraints of large deformation nearly incompressible materials. The proposed model was extended to large deformation regime by defining an integral average of the gradient of the deformation ($\bar{\boldsymbol{F}}$ approach). While integral-averaged $\bar{\boldsymbol{F}}$ methods have been presented before, there is little in the literature linking the modified deformation gradient to the appropriate strain-displacement matrix. In this dissertation, a framework was developed that related the choice of volume averaged $\bar{\boldsymbol{F}}$ ($\bar{J}$ averaged over the reference configuration or current configuration) to the resulting $\bar{\boldsymbol{B}}$ and derived the proper stiffness matrices. The performance of the proposed method was investigated using numerical examples. The examples demonstrated that the proposed $\bar{\boldsymbol{B}}$ approach could relieve the incompressibility constraints. The approach also exhibited the quadratic convergence rate that ensures a more efficient numerical formulation. Furthermore, the formulation offered was general and can also be extended to anisotropic and inelastic materials.

In addition to treating the incompressibility constraints of the hydrated matrix, the finite element model included a detailed structural and constitutive representation of the rat cornea. The model included the effects of preferentially oriented and dispersed collagen fibrils throughout the corneal stroma. For the rat cornea, in the central region, four preferred orientations of collagen fibrils were assumed (aligned in 0^o, 90^o, 45^o and 135^o with respect to the horizontal direction). It was presumed that 80% of the fibrils demonstrate preferred orientations and the remaining 20% were randomly distributed in the central cornea. For the region around the edge of the cornea (limbal area), 90% of collagen fibrils assumed to show circumferential orientations while the remaining demonstrate dispersed orientation. In the area between the two zones, the preferred orientations of collagen fibrils were linearly interpolated.

Due to the highly nonlinear mechanical behavior of the cornea, a hyperelastic constitutive model considering geometric and material nonlinearity of collagen fibrils was presented. For simplicity, only the stiffness of the stroma was considered. The strain energy density function was decomposed into a volumetric component of a penalty function and deviatoric effects of anisotropic fibrils and Neo-Hookean matrix. Four unit orientation vectors for the assumed fibril families were defined in the reference configuration.

The cornea structure was meshed using the proposed trilinear $\overline{\boldsymbol{B}}$ hexahedra with integral-averaged volume. The intraocular pressure exerted by the aqueous humor behind the cornea, was uniformly applied to the posterior side of the cornea. A Follower forces technique was implemented to maintain the correct direction (normal to the surface) and magnitude of the pressure with respect to the changing surface. The cornea displacement was restricted along the center of corneal edge while allowing rotation at the limbus.

The mesh refinement was performed throughout the cornea thickness to assess convergence. Based on the simulation results, a mesh of ten layers achieved converged values of strain, though the displacement convergence was much faster. The mesh was also refined near the center for better tracking of spirals.

Spatial assortment of epithelial cells tends to form characteristic spiral curves on the anterior surface of the cornea. Studying the generation of such patterns is important as it can reveal greater understanding of corneal function and possible disorders. While some models have been proposed to explain formation of spiral patterns, none have been able to completely explain this phenomenon. This dissertation proposed a framework for explaining assortment of epithelial cells into spiral patterns due to the effect of stresses and strains on the cornea.

To this end, four adult rat corneas (two from the same rat) were sectioned and imaged with confocal microscopy. The images revealed spiral patterns. Landmark points were overlaid onto the original cornea patch data. The patch edges were compared to logarithmic spirals and the spiral pitch angles were measured. For each rat cornea, the logarithmic spiral with median pitch angle was compared to the finite element simulation results.

The assumption taken was that during maturation, shear strains in the tissue facilitates the sliding of epithelial cells past each other. Yet, the pathlines of maximum shear strains obtained from numerical simulation did not fit observed spirals well in all of the sampling corneas. So, we hypothesized that normal stresses influence the movement of epithelial cells as they tend to pull the cells apart and facilitate sliding. This was also implied from the images of the slip planes of epithelial cells under tension [103]. Accordingly, our pathline tracking algorithm was modified considering a combination of the effect of shear and tensile strains.

The distribution of shear strains was obtained on the cornea surface from our finite element simulation. The pathlines of critical shear strains were tracked and demonstrated on top of the cornea surface together with the observed logarithmic spirals. In some cases, the observed logarithmic spirals fit well with pathlines of maximum shear strain directions, while in many other cases they fit pathlines of critical strains considering a mix of shear and tension well.

5.2 Future Work

There are some factors affecting the motion of epithelial cells that were not considered in our numerical model. The spiral patterns observed on the surface of mice and rat corneas seem to tighten up over time. Variations in the spiral development due to the cell growth and division in the organ were not included in our model. Considering two critical slip directions, if majority of

cells tend to slip in one dominant direction, cells assort into spiral patterns. However, if a group of cells slide along a critical direction and cells in other part slide in another direction, different patterns might form. Indeed, horseshoe patterns and other shapes have been observed in some corneas. In our models, we always chose a single critical strain orientation to match the spirals.

A future direction is to use the change in shape of the surface of the stroma as an input condition to model the rearrangement of epithelial cells over time. Cellular finite element models of tissues exist that account for the adhesion of the membranes, the viscosity of the cellular fluid, and even cell growth and division. More detailed models of the shear and tensile behavior of cell-to-cell adhesion would need to be developed, as well as the attachment to the basement membrane.

As the heart beats, the intraocular pressure behind the cornea changes and hence suggests considering dynamic motion of the cornea. This dynamic effect was lacking in our finite element model due to the complexity of the constitutive model used. A linearized model of the cornea is already being developed as an approach to account for the dynamic behavior of the cornea.

Finally, the material parameters used in the cornea model were based on limited data and are imperfect. Many researchers are developing experiments to capture the material structure and behavior of the cornea with greater accuracy. As this data becomes available, better cornea models can be constructed.

5.3 Final Remarks

While there is still some work to be done, the model presented lays much of the foundation. This dissertation offered a continuum finite strain model of mammalian cornea

considering material and geometric nonlinearity of collagen fibrils and incompressibility of hydrated matrix. The proposed finite element model could investigate biomechanical behavior of mammalian cornea.

Spiral patterns observed in nature have enchanted many scientists' attention throughout the years. However, a general explanation for development of such patterns is lacking. This dissertation tried to provide more information about generation of these fascinating patterns in a particular system based on the mechanical behavior of the system. A framework for studying the development of spiral patterns in the epithelium was presented and good agreement between the simulation curves and logarithmic spirals fitted to confocal images of the rat cornea were obtained. The numerical modeling effort was especially fruitful in explaining formation of spiral pattern on the surface of mammalian corneas.

Appendix: Stiffness Derivation for $\overline{B}$ method

As mentioned previously, the stiffness matrix may be derived using a directional derivative or a pseudo-time derivative. Here, we take the latter approach. We examine the nodal subvector of the element internal force vector

$$\boldsymbol{f}_I = \int_{\Omega_0{}^e} \overline{\boldsymbol{B}}_I^T \{\boldsymbol{\tau}\} d\Omega_0 = \int_{\Omega_0{}^e} \overline{\boldsymbol{\mathcal{B}}}_I^T : \boldsymbol{\tau}\, d\Omega_0$$

(91)

where, as mentioned previously, $\overline{\boldsymbol{\mathcal{B}}}_I = \boldsymbol{\mathcal{B}}_I + \frac{1}{3}(\boldsymbol{1}\otimes \overline{\boldsymbol{\nabla} N_I} - \boldsymbol{1}\otimes \boldsymbol{\nabla} N_I)$ and $(\boldsymbol{\mathcal{B}}_I)_{ija} = N_{I,j}\,\delta_{ia}$

For preliminaries, note that

$$\begin{aligned}
(\dot{\mathcal{B}}_I)_{ija} &= \dot{N}_{I,j}\,\delta_{ia} \\
&= -N_{I,k}\,l_{kj}\,\delta_{ia} \\
&= -N_{I,k}\,(\boldsymbol{\mathcal{B}}_J)_{kjb}\,\dot{d}_{jb}\,\delta_{ia} \\
&= -N_{I,k}\,N_{J,j}\,\delta_{kb}\,\dot{d}_{jb}\,\delta_{ia} \\
&= -\delta_{ia}\,N_{J,j}\,N_{I,b}\,N_{J,j}\,\dot{d}_{Jb}
\end{aligned}$$

(92)

and

$$\begin{aligned}
\dot{\overline{\mathcal{B}}}_{ija} &= \dot{\mathcal{B}}_{ija} + \left(\frac{1}{3}\,\dot{\overline{N}}_{I,a} - \dot{N}_{I,a}\right)\delta_{ij} \\
&= \dot{\mathcal{B}}_{ija} + \frac{1}{3}\left(\frac{\partial \overline{N}_{I,a}}{\partial d_{Jb}}\,\dot{d}_{Jb} - N_{I,k}\,l_{ka}\right)\delta_{ij} \\
&= \dot{\mathcal{B}}_{ija} + \frac{1}{3}\left(\frac{\partial \overline{N}_{I,a}}{\partial d_{Jb}} + N_{I,k}\,\mathcal{B}_{kab}\right)\delta_{ij}\dot{d}_{Jb}
\end{aligned}$$

(93)

The time derivative of the nodal subvector of the element internal force vector, then can be written

$$\dot{\boldsymbol{f}}_I = \int_{\Omega_0{}^e} \frac{d}{dt} \left(\overline{\boldsymbol{B}}_I^T : \boldsymbol{\tau} \right) d\Omega_0$$

(94)

Examining the quantity inside the integral

$$\frac{d}{dt} \left(\overline{\boldsymbol{B}}_I^T : \boldsymbol{\tau} \right)_a = \frac{d}{dt} \left[\left(\overline{\boldsymbol{\mathcal{B}}}_I \right)_{ija} \tau_{ij} \right] = \left(\dot{\overline{\boldsymbol{\mathcal{B}}}}_I \right)_{ija} \tau_{ij} + \left(\overline{\boldsymbol{\mathcal{B}}}_I \right)_{ija} \dot{\tau}_{ij}$$

(95)

For convenience, for the remainder of the derivation, we will move the nodal subscript of $\boldsymbol{\mathcal{B}}_I$ and $\overline{\boldsymbol{\mathcal{B}}}_I$ tensors to superscripts, e.g. $(\boldsymbol{\mathcal{B}}_I)_{ija} = \mathcal{B}^I_{ija}$

We examine the second term first. Recall that τ is a function of $\overline{\boldsymbol{F}}$ rather than $\boldsymbol{F}$. Hence,

$$\overline{\mathcal{B}}^I_{ija} \, \dot{\tau}_{ij} = \overline{\mathcal{B}}^I_{ija} \left(\tau^{\nabla c}_{ij} + \bar{l}_{ik} \, \tau_{kj} + \tau_{ik} \, \bar{l}_{jk} \right)$$

(96)

rather than

$$\overline{\mathcal{B}}^I_{ija} \left(\tau^{\nabla c}_{ij} + \bar{l}_{ik} \, \tau_{kj} + \tau_{ik} \, \bar{l}_{jk} \right)$$

(97)

Continuing

$$\overline{\mathcal{B}}^I_{ija} \, \dot{\tau}_{ij} = \overline{\mathcal{B}}^I_{ija} \left(C^{\tau}_{ijkl} \, \bar{l}_{kl} + \bar{l}_{ik} \, \tau_{kj} + \tau_{ik} \, \bar{l}_{jk} \right)$$

$$= \overline{\mathcal{B}}^I_{ija} \left(C^{\tau}_{ijkl} \, \overline{\mathcal{B}}^J_{klb} \dot{d}_{Jb} + \overline{\mathcal{B}}^J_{ikb} \, \dot{d}_{Jb} \, \tau_{kj} + \tau_{ik} \, \overline{\mathcal{B}}^J_{jkb} \, \dot{d}_{Jb} \right)$$

$$= \overline{\mathcal{B}}^I_{ija} \left(C^{\tau}_{ijkl} \, \overline{\mathcal{B}}^J_{klb} + \overline{\mathcal{B}}^J_{ikb} \, \tau_{kj} + \tau_{ik} \, \overline{\mathcal{B}}^J_{jkb} \right) \dot{d}_{Jb}$$

$$= \left(\overline{\mathcal{B}}^I_{ija} \, C^{\tau}_{ijkl} \, \overline{\mathcal{B}}^J_{klb} + \overline{\mathcal{B}}^I_{ija} \, \tau_{kj} \, \overline{\mathcal{B}}^J_{ikb} + \overline{\mathcal{B}}^I_{ija} \, \tau_{ik} \, \overline{\mathcal{B}}^J_{jkb} \right) \dot{d}_{Jb}$$

$$= [\ (\ \bar{B}^{I^T}\ [\mathbb{C}^T]\ \bar{B}^J)_{ab} +\ \ \bar{\mathcal{B}}^I_{ija}\,\tau_{kj}\,\bar{\mathcal{B}}^J_{ikb} +\ \bar{\mathcal{B}}^I_{ija}\,\tau_{ik}\,\bar{\mathcal{B}}^J_{jkb}\ ]\ \dot{d}_{Jb}$$

(98)

Taking the second and third quantities one at a time

$$\bar{\mathcal{B}}^I_{ija}\,\tau_{kj}\,\bar{\mathcal{B}}^J_{ikb} = [\ N_{I,j}\,\delta_{ia} + \tfrac{1}{3}\left(\bar{N}_{I,a} - N_{I,a}\right)\delta_{ij}\ ]\,\tau_{kj}\,[\ N_{J,k}\,\delta_{ib} + \tfrac{1}{3}\left(\bar{N}_{J,b} - N_{J,b}\right)\delta_{ik}]$$

$$= N_{I,j}\,\tau_{kl}\,N_{J,k}\,\delta_{ib}\,\delta_{ia} + N_{I,j}\,\delta_{ia}\,\tau_{kj}\ \tfrac{1}{3}\left(\bar{N}_{J,b} - N_{J,b}\right)\delta_{ik}$$

$$+ \tfrac{1}{3}\left(\bar{N}_{I,a} - N_{I,a}\right)\delta_{ij}\,\tau_{kj}\,N_{J,k}\,\delta_{ib}$$

$$+ \frac{1}{9}\left(\bar{N}_{I,a} - N_{I,a}\right)\delta_{ij}\ \tau_{kj}\left(\bar{N}_{J,b} - N_{J,b}\right)\delta_{ik}$$

$$= N_{I,j}\,\tau_{kl}\,N_{J,k}\,\delta_{ab} + N_{I,j}\ \tau_{ja}\ \tfrac{1}{3}\left(\bar{N}_{J,b} - N_{J,b}\right)$$

$$+ \tfrac{1}{3}\left(\bar{N}_{I,a} - N_{I,a}\right)\ \tau_{bk}\,N_{J,k}$$

$$+ \frac{1}{9}\left(\bar{N}_{I,a} - N_{I,a}\right)\ \tau_{kk}\left(\bar{N}_{J,b} - N_{J,b}\right)$$

$$= [\ \left(\boldsymbol{\nabla} N_I\,.\,\tau.\,\boldsymbol{\nabla} N_J\right)1 + \frac{1}{3}\left(\overline{\boldsymbol{\nabla} N_I}\,.\,\tau\right)\ \otimes\left(\overline{\boldsymbol{\nabla} N_J} - \boldsymbol{\nabla} N_I\right)$$

$$+ \frac{1}{3}\left(\overline{\boldsymbol{\nabla} N_I} - \boldsymbol{\nabla} N_I\right)\ \otimes\ \left(\boldsymbol{\nabla} N_J\,.\,\boldsymbol{\tau}\right)$$

$$+ \frac{\tau_{kk}}{9}\left(\overline{\boldsymbol{\nabla} N_I} - \boldsymbol{\nabla} N_I\right)\ \otimes\ \left(\overline{\boldsymbol{\nabla} N_J} - \boldsymbol{\nabla} N_J\right)\ ]_{ab}$$

(99)

The third term becomes

$$\bar{\mathcal{B}}^I_{ija}\,\tau_{ik}\,\bar{\mathcal{B}}^J_{jkb} = [\ N_{I,j}\,\delta_{ia} + \tfrac{1}{3}\left(\bar{N}_{I,a} - N_{I,a}\right)\delta_{ij}\ ]\,\tau_{ik}\,[\ N_{J,k}\,\delta_{ib} + \tfrac{1}{3}\left(\bar{N}_{J,b} - N_{J,b}\right)\delta_{jk}]$$

$$= N_{I,j}\,\tau_{ik}\,N_{J,k}\,\delta_{jb}\,\delta_{ia} + N_{I,j}\,\delta_{ia}\,\tau_{ik}\ \tfrac{1}{3}\left(\bar{N}_{J,b} - N_{J,b}\right)\delta_{jk}$$

$$+ \tfrac{1}{3}\left(\bar{N}_{I,a} - N_{I,a}\right)\delta_{ij}\,\tau_{ik}\,N_{J,k}\,\delta_{jb}$$

$$+\frac{1}{9}\left(\bar{N}_{I,a}-N_{I,a}\right)\delta_{ij}\;\tau_{kj}\left(\bar{N}_{J,b}-N_{J,b}\right)\delta_{jk}$$

$$=N_{I,b}\,\tau_{ak}\,N_{J,k}+N_{I,k}\;\tau_{ka}\,\frac{1}{3}\left(\bar{N}_{J,b}-N_{J,b}\right)$$

$$+\frac{1}{3}\left(\bar{N}_{I,a}-N_{I,a}\right)\tau_{bk}\,N_{J,k}$$

$$+\frac{1}{9}\left(\bar{N}_{I,a}-N_{I,a}\right)\tau_{kk}\left(\bar{N}_{J,b}-N_{J,b}\right)$$

$$=\left[\;(\boldsymbol{\nabla}N_J\,.\tau)\;\otimes\;\boldsymbol{\nabla}N_I+\frac{1}{3}\,(\,\overline{\boldsymbol{\nabla}N_I}\,.\tau)\;\otimes(\,\overline{\boldsymbol{\nabla}N_J}\;-\;\boldsymbol{\nabla}N_I)\right.$$

$$+\frac{1}{3}\,(\,\overline{\boldsymbol{\nabla}N_I}-\boldsymbol{\nabla}N_I)\;\otimes\;\left(\boldsymbol{\nabla}N_J\,.\tau\right)$$

$$\left.+\frac{\tau_{kk}}{9}\,(\,\overline{\boldsymbol{\nabla}N_I}-\boldsymbol{\nabla}N_I\,)\;\otimes\;\left(\,\overline{\boldsymbol{\nabla}N_J}-\boldsymbol{\nabla}N_J\right)\right]_{ab}$$

(100)

Next we evaluate

$$\left(\dot{\bar{\boldsymbol{\mathcal{B}}}}_I\right)_{ija}\;\tau_{ij}=\left[-\delta_{ia}\,N_{J,j}\,N_{I,b}\,\dot{d}_{Jb}+\frac{1}{3}\left(\frac{\partial\bar{N}_{I,a}}{\partial d_{Jb}}+\;N_{I,k}\,B_{kab}\right)\delta_{ij}\,\dot{d}_{Jb}\right]\tau_{ij}=$$

$$=\left[-\tau_{aj}\,N_{J,j}\,N_{I,b}\;+\frac{\tau_{jj}}{3}\left(\frac{\partial\bar{N}_{I,a}}{\partial d_{Jb}}+\;N_{I,k}\,N_{J,a}\,\delta_{kb}\right)\right]\dot{d}_{Jb}$$

$$=\left[-\tau_{aj}\,N_{J,j}\,N_{I,b}\;+\frac{\tau_{jj}}{3}\;\frac{\partial\bar{N}_{I,a}}{\partial d_{Jb}}+\frac{\tau_{jj}}{3}\,N_{I,b}\,N_{J,a}\right]\dot{d}_{Jb}$$

$$=\left[-(\boldsymbol{\nabla}N_J\,.\tau)\;\otimes\;\boldsymbol{\nabla}N_J+\frac{\tau_{jj}}{3}\frac{\mathrm{d}\overline{\boldsymbol{\nabla}N_I}}{\mathrm{d}\boldsymbol{d}_J}+\frac{\tau_{jj}}{3}\;\;\boldsymbol{\nabla}N_J\;\otimes\;\boldsymbol{\nabla}N_I\,\right]_{ab}\;\dot{d}_{Jb}$$

(101)

Adding up all these quantities, we find that

$$\frac{d}{dt}\,(\,\bar{\boldsymbol{\mathcal{B}}}_I^T\!:\tau)=\;[\,\bar{\boldsymbol{\mathcal{B}}}_I^T\,[\mathbb{C}^\tau]\;\bar{\boldsymbol{\mathcal{B}}}_J+\left(\,\boldsymbol{\nabla}N_I\,.\tau\,.\boldsymbol{\nabla}N_J\,\right)\mathbf{1}$$

$$+\frac{2}{3}\,(\overline{\boldsymbol{\nabla} N_I}\,.\,\tau)\otimes\left(\overline{\boldsymbol{\nabla} N_J}-\boldsymbol{\nabla} N_J\right)+\frac{2}{3}\,(\overline{\boldsymbol{\nabla} N_I}-\boldsymbol{\nabla} N_I)\otimes(\overline{\boldsymbol{\nabla} N_I}\,.\,\tau)$$

$$+\frac{2\tau_{kk}}{9}\,(\overline{\boldsymbol{\nabla} N_I}-\boldsymbol{\nabla} N_I)\otimes\left(\overline{\boldsymbol{\nabla} N_J}-\boldsymbol{\nabla} N_J\right)$$

$$+\frac{\tau_{kk}}{3}\left(\boldsymbol{\nabla} N_J\otimes\boldsymbol{\nabla} N_I+\frac{\mathrm{d}\overline{\boldsymbol{\nabla} N_I}}{\mathrm{d}\boldsymbol{d}_J}\right)]\,\dot{\boldsymbol{d}}_J \qquad (102)$$

And hence the nodal sub-matrices of the element stiffness matrix may be written

$$\boldsymbol{K}_{IJ}^{e}=\int_{\Omega_0{}^e}\overline{\boldsymbol{B}}_I^T[\mathbb{C}^\tau]\overline{\boldsymbol{B}}_J+\left(\boldsymbol{\nabla} N_I\cdot\boldsymbol{\tau}\cdot\boldsymbol{\nabla} N_J\right)1$$

$$+\frac{2}{3}(\boldsymbol{\nabla} N_I\cdot\boldsymbol{\tau})\otimes\left(\overline{\boldsymbol{\nabla} N_J}-\boldsymbol{\nabla} N_J\right)+\frac{2}{3}(\overline{\boldsymbol{\nabla} N_I}-\boldsymbol{\nabla} N_I)\otimes\left(\boldsymbol{\nabla} N_J\cdot\boldsymbol{\tau}\right)$$

$$+\frac{2\tau_{kk}}{9}(\overline{\boldsymbol{\nabla} N_I}-\boldsymbol{\nabla} N_I)\otimes\left(\overline{\boldsymbol{\nabla} N_J}-\boldsymbol{\nabla} N_J\right)+\frac{\tau_{kk}}{3}\left(\boldsymbol{\nabla} N_J\otimes\boldsymbol{\nabla} N_I+\frac{d\overline{\boldsymbol{\nabla} N_I}}{d\boldsymbol{d}_J}\right)d\Omega_0 \qquad (103)$$

The first term is the common "material stiffness" with the modified $\boldsymbol{B}$ matrix, and the second term the standard geometric stiffness. The remaining terms arise from the modifications to the derivatives introduced by modifying the $\boldsymbol{B}$ matrix. The final term, of course, depends on the form of $\overline{\boldsymbol{\nabla} N_J}$. For the Jacobian averaged over the reference configuration

$$\dot{\overline{\boldsymbol{\nabla} N_I}}=\frac{d}{dt}\,\frac{\int_{\Omega_0{}^e}J\,\boldsymbol{\nabla} N_I\,d\Omega_0}{\int_{\Omega_0{}^e}J\,d\Omega_0}$$

$$=\frac{\int_{\Omega_0{}^e}\dot{J}\,\boldsymbol{\nabla} N_I+J\,\frac{d\boldsymbol{\nabla} N_I}{dt}\,d\Omega_0}{\int_{\Omega_0{}^e}J\,d\Omega_0}-\frac{\int_{\Omega_0{}^e}J\,\boldsymbol{\nabla} N_I\,d\Omega_0\int_{\Omega_0{}^e}\dot{J}\,d\Omega_0}{\left(\int_{\Omega_0{}^e}J\,d\Omega_0\right)^2}$$

$$=\frac{\int_{\Omega_0{}^e}J\,tr\,(\boldsymbol{l})\,\boldsymbol{\nabla} N_I+J\,\boldsymbol{\nabla} N_I.\boldsymbol{l}\,d\Omega_0}{\int_{\Omega_0{}^e}J\,d\Omega_0}-\frac{\int_{\Omega_0{}^e}J\,\boldsymbol{\nabla} N_I\,d\Omega_0\int_{\Omega_0{}^e}J\,tr\,(\boldsymbol{l})\,d\Omega_0}{\left(\int_{\Omega_0{}^e}J\,d\Omega_0\right)^2}$$

$$= \frac{\int_{\Omega_0{}^e} J\,(\boldsymbol{\nabla} N_J.\dot{\boldsymbol{d}}_J)\boldsymbol{\nabla} N_I - J\,\boldsymbol{\nabla} N_I\,.\,(\dot{\boldsymbol{d}}_J \otimes \boldsymbol{\nabla} N_J)\,d\Omega_0}{\int_{\Omega_0{}^e} J\,d\Omega_0}$$

$$- \frac{\int_{\Omega_0{}^e} J\,\boldsymbol{\nabla} N_I\,d\Omega_0 \int_{\Omega_0{}^e} J\,(\boldsymbol{\nabla} N_J.\dot{\boldsymbol{d}}_J)\,d\Omega_0}{(\int_{\Omega_0{}^e} J\,d\Omega_0)^2}$$

$$= (\frac{\int_{\Omega_0{}^e} J\,(\boldsymbol{\nabla} N_I \otimes \boldsymbol{\nabla} N_J - \boldsymbol{\nabla} N_J \otimes \boldsymbol{\nabla} N_I)\,d\Omega_0}{\int_{\Omega_0{}^e} J\,d\Omega_0}$$

$$- \frac{\int_{\Omega_0{}^e} J\,\boldsymbol{\nabla} N_I\,d\Omega_0 \otimes \int_{\Omega_0{}^e} J\,\boldsymbol{\nabla} N_J\,d\Omega_0}{\left(\int_{\Omega_0{}^e} J\,d\Omega_0\right)\left(\int_{\Omega_0{}^e} J\,d\Omega_0\right)})\,\dot{\boldsymbol{d}}_J$$

$$= \left(\frac{\int_{\Omega_0{}^e} J\,(\boldsymbol{\nabla} N_I \otimes \boldsymbol{\nabla} N_J - \boldsymbol{\nabla} N_J \otimes \boldsymbol{\nabla} N_I)\,d\Omega_0}{\int_{\Omega_0{}^e} J\,d\Omega_0} - \overline{\boldsymbol{\nabla} N_I} \otimes \overline{\boldsymbol{\nabla} N_J}\right)\dot{\boldsymbol{d}}_J$$

(104)

Therefore,

$$\frac{d\overline{\boldsymbol{\nabla} N_I}}{d\boldsymbol{d}_J} = \frac{\int_{\Omega_0{}^e} J\,(\boldsymbol{\nabla} N_I \otimes \boldsymbol{\nabla} N_J - \boldsymbol{\nabla} N_J \otimes \boldsymbol{\nabla} N_I)\,d\Omega_0}{\int_{\Omega_0{}^e} J\,d\Omega_0} - \overline{\boldsymbol{\nabla} N_I} \otimes \overline{\boldsymbol{\nabla} N_J}$$

(105)

The process for the Jacobian averaged in the current configuration is the same, though the calculations are more tedious. The resulting derivative in the current configuration may be calculated as

$$\frac{d\overline{\boldsymbol{\nabla} N_I}}{d\boldsymbol{d}_J} = \frac{4\int_{\Omega_0{}^e} J^2\,\boldsymbol{\nabla} N_I \otimes \boldsymbol{\nabla} N_J\,d\Omega_0}{\int_{\Omega_0{}^e} J^2\,d\Omega_0} - \frac{2\int_{\Omega_0{}^e} J^2\,\boldsymbol{\nabla} N_J \otimes \boldsymbol{\nabla} N_I\,d\Omega_0}{\int_{\Omega_0{}^e} J^2\,d\Omega_0}$$

$$- \frac{4\left(\int_{\Omega_0{}^e} J^2\,\boldsymbol{\nabla} N_I\,d\Omega_0\right)\otimes\left(\int_{\Omega_0{}^e} J^2\,\boldsymbol{\nabla} N_J\,d\Omega_0\right)}{\int_{\Omega_0{}^e} J^2\,d\Omega_0} - \frac{2\int_{\Omega_0{}^e} J\,\boldsymbol{\nabla} N_I \otimes \boldsymbol{\nabla} N_J\,d\Omega_0}{\int_{\Omega_0{}^e} J\,d\Omega_0}$$

$$+ \frac{\int_{\Omega_0{}^e} J\,\boldsymbol{\nabla} N_J \otimes \boldsymbol{\nabla} N_I\,d\Omega_0}{\int_{\Omega_0{}^e} J\,d\Omega_0} - \frac{\left(\int_{\Omega_0{}^e} J\,\boldsymbol{\nabla} N_I\,d\Omega_0\right)\otimes\left(\int_{\Omega_0{}^e} J\,\boldsymbol{\nabla} N_J\,d\Omega_0\right)}{(\int_{\Omega_0{}^e} J\,d\Omega_0)^2}$$

(106)

6 References

[1] J. M. Collinson, “Corneal Development, Limbal Stem Cell Function, and Corneal Epithelial Cell Migration in the Pax6+/- Mouse,” *Invest. Ophthalmol. Vis. Sci.*, vol. 45, no. 4, pp. 1101–1108, Apr. 2004.

[2] S. Iannaccone, Y. Zhou, D. Walterhouse, G. Taborn, G. Landini, and P. Iannaccone, “Three dimensional visualization and fractal analysis of mosaic patches in rat chimeras: cell assortment in liver, adrenal cortex and cornea.,” *PLoS One*, vol. 7, no. 2, p. e31609, Jan. 2012.

[3] D. W. DelMonte and T. Kim, “Anatomy and physiology of the cornea,” *J. Cataract Refract. Surg.*, vol. 37, no. 3, pp. 588–598, 2011.

[4] S. Hayes, C. Boote, J. Lewis, J. Sheppard, M. Abahussin, A. J. Quantock, C. Purslow, M. Votruba, and K. M. Meek, “Comparative study of fibrillar collagen arrangement in the corneas of primates and other mammals.,” *Anat. Rec. (Hoboken).*, vol. 290, no. 12, pp. 1542–50, Dec. 2007.

[5] J. Sheppard, S. Hayes, C. Boote, M. Votruba, and K. M. Meek, “Changes in corneal collagen architecture during mouse postnatal development.,” *Invest. Ophthalmol. Vis. Sci.*, vol. 51, no. 6, pp. 2936–42, Jun. 2010.

[6] Y. Mandel, S. Laufer, and B. Rubinsky, “Measurement of corneal endothelial impedance with non-invasive external electrodes–A theoretical study,” *Med. Eng. Phys.*, vol. 34, no. 2, pp. 195–201, 2012.

[7] N. Lagali, J. Germundsson, and P. Fagerholm, “The role of Bowman’s layer in corneal regeneration after phototherapeutic keratectomy: a prospective study using in vivo confocal microscopy.,” *Invest. Ophthalmol. Vis. Sci.*, vol. 50, no. 9, pp. 4192–8, Sep. 2009.

[8] P. Iannaccone, “The study of mammalian organogenesis by mosaic pattern analysis,” *Cell Differ.*, vol. 21, no. 2, pp. 79–91, 1987.

[9] G. Landini and P. M. Iannacconne, “Modeling of mosaic patterns in chimeric liver and adrenal cortex: algorithmic organogenesis?,” *J. Fed. Am. Soc. Exp. Biol.*, vol. 14, no. 5, pp. 823–827, Apr. 2000.

[10] C. D. F. J. Rhee, T. Mohammad Nejad, O. Comets, S. Flannery, E.B. Gulsoy, P. Iannaccone, “The golden spiral in abduction of mouse corneal behaviors.”

[11] A. Albanese, R. Urso, L. Bianciardi, M. Rigato, and E. Battisti, “Keratoconus, cross-link-induction, comparison between fitting exponential function and a fitting equation obtained by a mathematical model,” *Biomed. Pharmacother.*, vol. 63, no. 9, pp. 693–696, 2009.

[12] A. Pandolfi and G. A. Holzapfel, “Three-dimensional modeling and computational analysis of the human cornea considering distributed collagen fibril orientations.,” *J. Biomech. Eng.*, vol. 130, no. 6, p. 061006, Dec. 2008.

[13] D. M. Maurice, “The Cornea and Sclera,” in *The eye 1*, vol. 489–600, 1984, pp. 1–158.

[14] J. S. Graham, A. N. Vomund, C. L. Phillips, and M. Grandbois, “Structural changes in human type I collagen fibrils investigated by force spectroscopy,” *Exp. Cell Res.*, vol. 299, no. 2, pp. 335–342, 2004.

[15] M. Alastrué, V. Calvo, B. Peña, E. Doblaré, “Biomechanical modeling of refractive corneal surgery,” no. 60, pp. 128–150, 2006.

[16] P. M. Pinsky, D. van der Heide, and D. Chernyak, “Computational modeling of mechanical anisotropy in the cornea and sclera,” *J. Cataract Refract. Surg.*, vol. 31, no. 1, pp. 136–145, 2005.

[17] K. M. Meek, T. Blamires, G. F. Elliott, T. J. Gyi, and C. Nave, “The organisation of collagen fibrils in the human corneal stroma: a synchrotron X-ray diffraction study,” *Curr. Eye Res.*, vol. 6, no. 7, pp. 841–846, 1987.

[18] K. M. Meek and R. H. Newton, “Organization of collagen fibrils in the corneal stroma in relation to mechanical properties and surgical practice.,” *J. Refract. Surg. (Thorofare, NJ 1995)*, vol. 15, no. 6, p. 695, 1999.

[19] A. Daxer and P. Fratzl, “Collagen fibril orientation in the human corneal stroma and its implication in keratoconus.,” *Invest. Ophthalmol. Vis. Sci.*, vol. 38, no. 1, pp. 121–129, 1997.

[20] A. Pandolfi and F. Manganiello, “A model for the human cornea: constitutive formulation and numerical analysis.,” *Biomech. Model. Mechanobiol.*, vol. 5, no. 4, pp. 237–46, Nov. 2006.

[21] L. A. Carvalho, M. Prado, R. H. Cunha, A. C. Neto, A. P. Jr, P. Schor, and W. Chamon, “Keratoconus prediction using a finite element model of the cornea with local biomechanical properties,” *Arq. Bras. Oftalmol.*, vol. 72, no. 2, pp. 139–145, 2009.

[22] A. Gefen, R. Shalom, D. Elad, and Y. Mandel, “Biomechanical analysis of the keratoconic cornea.,” *J. Mech. Behav. Biomed. Mater.*, vol. 2, no. 3, pp. 224–36, Jul. 2009.

[23] A. Pandolfi, G. Fotia, and F. Manganiello, “Finite element simulations of laser refractive corneal surgery,” *Eng. Comput.*, vol. 25, no. 1, pp. 15–24, 2009.

[24] A. S. Roy and W. J. Dupps, “Effects of altered corneal stiffness on native and postoperative LASIK corneal biomechanical behavior: A whole-eye finite element analysis.,” *J. Refract. Surg. (Thorofare, NJ 1995)*, vol. 25, no. 10, p. 875, 2009.

[25] S. J. Mousavi, N. Nassiri, N. Masoumi, N. Nassiri, M. Majdi-N, S. Farzaneh, A. R. Djalilian, and G. A. Peyman, "Finite Element Analysis of Blunt Foreign Body Impact on the Cornea After PRK and LASIK," *J. Refract. Surg.*, vol. 28, no. 1, pp. 59–64, 2012.

[26] A. S. Roy and W. J. Dupps, "Patient-specific computational modeling of keratoconus progression and differential responses to collagen cross-linking," *Invest. Ophthalmol. Vis. Sci.*, vol. 52, no. 12, pp. 9174–9187, 2011.

[27] M. Shafahi and K. Vafai, "Human eye response to thermal disturbances," *J. Heat Transfer*, vol. 133, no. 1, p. 11009, 2011.

[28] A. Papaioannou and T. Samaras, "Numerical model of heat transfer in the rabbit eye exposed to 60-GHz millimeter wave radiation," *Biomed. Eng. IEEE Trans.*, vol. 58, no. 9, pp. 2582–2588, 2011.

[29] B. Jo and A. Aksan, "Prediction of the extent of thermal damage in the cornea during conductive keratoplasty," *J. Therm. Biol.*, vol. 35, no. 4, pp. 167–174, 2010.

[30] A. Guimera, A. Ivorra, G. Gabriel, and R. Villa, "Non-invasive assessment of corneal endothelial permeability by means of electrical impedance measurements," *Med. Eng. Phys.*, vol. 32, no. 10, pp. 1107–1115, 2010.

[31] L. Li and P. M. Pinsky, "A nonlinear macroscopic multi-phasic model for describing interactions between solid, fluid and ionic species in biological tissue materials," *Philos. Mag.*, vol. 91, no. 2, pp. 300–314, 2011.

[32] K. Anderson, A. El-Sheikh, and T. Newson, "Application of structural analysis to the mechanical behaviour of the cornea," *J. R. Soc. Interface*, vol. 1, no. 1, pp. 3–15, 2004.

[33] H. C. Howland, R. H. Rand, and S. R. Lubkin, "A thin-shell model of the cornea and its application to corneal surgery," *Refract Corneal Surg*, vol. 8, pp. 183–186, 1992.

[34] P. M. Pinsky and D. V Datye, "A microstructurally-based finite element model of the incised human cornea," *J. Biomech.*, vol. 24, no. 10, pp. 907–922, 1991.

[35] L. Li and B. Tighe, "The anisotropic material constitutive models for the human cornea," *J. Struct. Biol.*, vol. 153, no. 3, pp. 223–230, 2006.

[36] A. Elsheikh and D. Wang, "Numerical modelling of corneal biomechanical behaviour," *Comput. Methods Biomech. Biomed. Engin.*, vol. 10, no. 2, pp. 85–95, 2007.

[37] V. der H. G. L. Dubbelman M Sicam VA, "The shape of the anterior and posterior surface of the aging human cornea," vol. 46(6–7):99, 2006.

[38] D. A. Hoeltzel, P. Altman, K. Buzard, and K. Choe, “Strip extensiometry for comparison of the mechanical response of bovine, rabbit, and human corneas.,” *J. Biomech. Eng.*, vol. 114, no. 2, p. 202, 1992.

[39] T. D. Nguyen, R. E. Jones, and B. L. Boyce, “A nonlinear anisotropic viscoelastic model for the tensile behavior of the corneal stroma.,” *J. Biomech. Eng.*, vol. 130, no. 4, p. 41020, 2008.

[40] T. D. Nguyen and B. L. Boyce, “An inverse finite element method for determining the anisotropic properties of the cornea,” *Biomech. Model. Mechanobiol.*, vol. 10, no. 3, pp. 323–337, 2011.

[41] K. A. Buzard, “Introduction to biomechanics of the cornea.,” *Refract. Corneal Surg.*, vol. 8, no. 2, p. 127, 1992.

[42] S. Salimi, S. S. Park, and T. Freiheit, “Dynamic Response of Intraocular Pressure and Biomechanical Effects of the Eye Considering Fluid-Structure Interaction,” *J. Biomech. Eng.*, vol. 133, no. 9, 2011.

[43] T. J. R. Hughes, “Generalization of selective integration procedures to anisotropic and non-linear media,” *Int. J. Numer. Methods Eng.*, vol. 15, no. 9, pp. 1413–1418, Sep. 1980.

[44] E. Uchio, S. Ohno, J. Kudoh, K. Aoki, and L. T. Kisielewicz, “Simulation model of an eyeball based on finite element analysis on a supercomputer,” *Br. J. Ophthalmol.*, vol. 83, no. 10, pp. 1106–1111, 1999.

[45] R. Amini and V. H. Barocas, “Anterior chamber angle opening during corneoscleral indentation: the mechanism of whole eye globe deformation and the importance of the limbus,” *Invest. Ophthalmol. Vis. Sci.*, vol. 50, no. 11, pp. 5288–5294, 2009.

[46] A. Elsheikh, B. Geraghty, P. Rama, M. Campanelli, and K. M. Meek, “Characterization of age-related variation in corneal biomechanical properties,” *J. R. Soc. Interface*, vol. 7, no. 51, pp. 1475–1485, 2010.

[47] M. Fraldi, A. Cutolo, L. Esposito, and F. Guarracino, “The role of viscoelasticity and stress gradients on the outcome of conductive keratoplasty,” *Biomech. Model. Mechanobiol.*, vol. 10, no. 3, pp. 397–412, 2011.

[48] R. P. Vito, T. J. Shin, and B. E. McCarey, “A mechanical model of the cornea: the effects of physiological and surgical factors on radial keratotomy surgery,” *Refract. Corneal Surg.*, vol. 5, no. 2, pp. 82–88, 1989.

[49] M. R. Bryant, S. A. Velinsky, M. E. Plesha, and G. P. Clarke, “Computer-aided surgical design in refractive keratotomy,” *Eye Contact Lens*, vol. 13, no. 4, pp. 238–242, 1987.

[50] K. D. Hanna, F. E. Jouve, and G. O. W. 3rd, “Preliminary computer simulation of the effects of radial keratotomy,” *Arch. Ophthalmol.*, vol. 107, no. 6, pp. 911–918, Jun. 1989.

[51] S. A. Velinsky and M. R. Bryant, “On the computer-aided and optimal design of keratorefractive surgery,” *Refract. Corneal Surg.*, vol. 8, no. 2, pp. 173–182, 1992.

[52] S. Niroomandi, I. Alfaro, D. Gonzalez, E. Cueto, and F. Chinesta, “Real-time simulation of surgery by reduced-order modeling and X-FEM techniques,” *Int. j. numer. method. biomed. eng.*, vol. 28, no. 5, pp. 574–588, 2012.

[53] M. R. Bryant and P. J. McDonnell, “Constitutive laws for biomechanical modeling of refractive surgery.,” *J. Biomech. Eng.*, vol. 118, no. 4, pp. 473–481, 1996.

[54] J. A. Cristóbal, M. A. del Buey, F. J. Ascaso, E. Lanchares, B. Calvo, and M. Doblaré, “Effect of limbal relaxing incisions during phacoemulsification surgery based on nomogram review and numerical simulation,” *Cornea*, vol. 28, no. 9, pp. 1042–1049, 2009.

[55] L. Yoo, J. Reed, A. Shin, J. Kung, J. K. Gimzewski, V. Poukens, R. A. Goldberg, R. Mancini, M. Taban, and R. Moy, “Characterization of ocular tissues using microindentation and hertzian viscoelastic models,” *Invest. Ophthalmol. Vis. Sci.*, vol. 52, no. 6, pp. 3475–3482, 2011.

[56] G. Wollensak, E. Spoerl, and T. Seiler, “Stress-strain measurements of human and porcine corneas after riboflavin–ultraviolet-A-induced cross-linking,” *J. Cataract Refract. Surg.*, vol. 29, no. 9, pp. 1780–1785, 2003.

[57] Y. Zeng, J. Yang, K. Huang, Z. Lee, and X. Lee, “A comparison of biomechanical properties between human and porcine cornea,” *J. Biomech.*, vol. 34, no. 4, pp. 533–537, 2001.

[58] M. Kohlhaas, E. Spoerl, T. Schilde, G. Unger, C. Wittig, and L. E. Pillunat, “Biomechanical evidence of the distribution of cross-links in corneastreated with riboflavin and ultraviolet A light,” *J. Cataract Refract. Surg.*, vol. 32, no. 2, pp. 279–283, 2006.

[59] A. Elsheikh, D. Wang, and D. Pye, “Determination of the modulus of elasticity of the human cornea,” *J. Refract. Surg. (Thorofare, N.J. 1995)*, vol. 23, no. 8, pp. 808–818, Oct. 2007.

[60] S. J. Petsche, D. Chernyak, J. Martiz, M. E. Levenston, and P. M. Pinsky, “Depth-dependent transverse shear properties of the human corneal stroma.,” *Invest. Ophthalmol. Vis. Sci.*, vol. 53, no. 2, pp. 873–80, Feb. 2012.

[61] T. Belytschko, H. Chen, J. Xu, and G. Zi, “Dynamic crack propagation based on loss of hyperbolicity and a new discontinuous enrichment,” *Int. J. Numer. Methods Eng.*, vol. 58, no. 12, pp. 1873–1905, 2003.

[62] A. A. H. Sayed, N. H. Solouma, A. A. El-Berry, and Y. M. Kadah, “Finite element models for computer simulation of intrastromal photorefractive Keratectomy,” *J. Mech. Med. Biol.*, vol. 11, no. 05, pp. 1255–1270, 2011.

[63] C. D. Foster, D. Gongal, T. Begaj, and M. Luo, “Embedded collagen deformation models for computational modeling of healthy, kerataconic and crosslinked corneas,” May 2013.

[64] J. D. Stitzel, S. M. Duma, J. M. Cormier, and I. P. Herring, “A nonlinear finite element model of the eye with experimental validation for the prediction of globe rupture,” in *SAE Conference Proceedings P*, 2002, pp. 81–102.

[65] A. A. Weaver, E. A. Kennedy, S. M. Duma, and J. D. Stitzel, “Evaluation of different projectiles in matched experimental eye impact simulations,” *J. Biomech. Eng.*, vol. 133, no. 3, p. 31002, Mar. 2011.

[66] W. Gray, W. E. Sponsel, F. W. Scribbick, A. R. Stern, C. E. Weiss, S. L. Groth, and J. D. Walker, “Numerical modeling of paintball impact ocular trauma: identification of progressive injury mechanisms,” *Invest. Ophthalmol. Vis. Sci.*, vol. 52, no. 10, pp. 7506–7513, 2011.

[67] J. Ghaboussi, T.-H. Kwon, D. A. Pecknold, and Y. Hashash, “Accurate intraocular pressure prediction from applanation response data using genetic algorithm and neural networks,” *J. Biomech.*, vol. 42, no. 14, pp. 2301–2306, 2009.

[68] T. J. R. Hughes, *The Finite Element Method*. Prentice-Hall: New Jersey, 1987.

[69] D. P. Flanagan and T. Belytschko, “A uniform strain hexahedron and quadrilateral with orthogonal hourglass control,” *Int. J. Numer. Methods Eng.*, vol. 17, no. 5, pp. 679–706, 1981.

[70] T. Belytschko, J. S. J. Ong, W. K. Liu, and J. M. Kennedy, “Hourglass control in linear and nonlinear problems,” *Comput. Methods Appl. Mech. Eng.*, vol. 43, no. 3, pp. 251–276, 1984.

[71] S. Reese, M. Kussner, and B. D. Reddy, “A new stabilization technique for finite elements in non-linear elasticity,” *Int. J. Numer. Methods Eng.*, vol. 44, no. 11, pp. 1617–1652, Apr. 1999.

[72] S. Reese, P. Wriggers, and B. D. Reddy, “A new locking-free brick element technique for large deformation problems in elasticity,” *Comput. Struct.*, vol. 75, no. 3, pp. 291–304, Apr. 2000.

[73] T. Sussman and K.-J. Bathe, “A finite element formulation for nonlinear incompressible elastic and inelastic analysis,” *Comput. Struct.*, vol. 26, no. 1–2, pp. 357–409, Jan. 1987.

[74] E. P. Kasper and R. L. Taylor, “A mixed-enhanced strain method Part I: Geometrically linear problems,” *Comput. Struct.*, vol. 75, no. 3, pp. 237–250, Apr. 2000.

[75] E. P. Kasper and R. L. Taylor, “A mixed-enhanced strain method Part II: Geometrically nonlinear problems,” *Comput. Struct.*, vol. 75, no. 3, pp. 237–250, Apr. 2000.

[76] J. C. Simo, R. L. Taylor, and K. S. Pister, “Variational and projection methods for the volume constraint in finite deformation elasto-plasticity,” *Comput. Methods Appl. Mech. Eng.*, vol. 51, no. 1–3, pp. 177–208, 1985.

[77] J. C. Simo and M. S. Rifai, “A class of mixed assumed strain methods and the method of incompatible modes,” *Int. J. Numer. Methods Eng.*, vol. 29, no. 8, pp. 1595–1638, Jun. 1990.

[78] A. Masud and K. M. Xia, “A stabilized mixed finite element method for nearly incompressible elasticity,” *J. Appl. Mech. ASME*, vol. 72, no. 5, pp. 711–720, Sep. 2005.

[79] A. Masud and K. M. Xia, “A variational multiscale method for inelasticity: Application to superelasticity in shape memory alloys,” *Comput. Methods Appl. Mech. Eng.*, vol. 195, no. 33–36, pp. 4512–4531, 2006.

[80] K. M. Xia and A. Masud, “A stabilized finite element formulation for finite deformation elastoplasticity in geomechanics,” *Comput. Geotech.*, vol. 36, no. 3, pp. 396–405, Apr. 2009.

[81] B. Ramesh and A. M. Maniatty, “Stabilized finite element formulation for elastic-plastic finite deformations,” *Comput. Methods Appl. Mech. Eng.*, vol. 194, no. 6–8, pp. 775–800, 2005.

[82] F. Brezzi and M. Fortin, *Mixed and Hybrid Finite Element Methods*. Springer: Berlin, Heidelerg, New York, 1991.

[83] B. Szabo and I. Babuska, *Finite Element Analysis*. Wiley, New York, 1991.

[84] B. Moran, M. Ortiz, and C. F. Shih, “Formulation of implicit finite-element methods for multiplicative finite deformation plasticity,” *Int. J. Numer. Methods Eng.*, vol. 29, no. 3, pp. 483–514, Mar. 1990.

[85] E. A. de Souza Neto, D. Peric, M. Dutko, and D. R. J. Owen, “Design of simple low order finite elements for large strain analysis of nearly incompressible solids,” *Int. J. Solids Struct.*, vol. 33, pp. 3277–3296, 1996.

[86] J. C. Nagtegaal, D. M. Parks, and J. R. Rice, “On numerically accurate finite element solutions in the fully plastic range,” *Comput. Methods Appl. Mech. Eng.*, vol. 4, no. 2, pp. 153–177, 1974.

[87] K. M. Mathisen, K. M. Okstad, T. Kvamsdal, and S. B. Raknes, “Isogeometric analysis of finite deformation nearly incompressible solids,” *J. Struct. Mech.*, vol. 44, no. 3, pp. 260–278, 2011.

[88] E. A. de Souza Neto, F. M. A. Pires, and D. R. J. Owen, “F-bar-based linear triangles and tetrahedra for finite strain analysis of nearly incompressible solids. Part I: formulation and benchmarking,” *Int. J. Numer. Methods Eng.*, vol. 62, no. 3, pp. 353–383, Jan. 2005.

[89] T. Elguedj, Y. Bazilevs, V. M. Calo, and T. J. R. Hughes, “F-bar projection method for finite deformation elasticity and plasticity using NURBS based isogeometric analysis,” *Int. J. Mater. Form.*, vol. 1, no. 1, pp. 1091–1094, Apr. 2008.

[90] T. Belytschko, C. S. Tsay, and W. K. Liu, “A stabilization matrix for the bilinear mindlin plate element,” *Comput. Methods Appl. Mech. Eng.*, vol. 29, no. 3, pp. 313–327, Dec. 1981.

[91] S. Doll, K. Schweizerhof, R. Hauptmann, and C. Freischläger, “On volumetric locking of low-order solid and solid-shell elements for finite elastoviscoplastic deformations and selective reduced integration,” *Eng. Comput.*, vol. 17, no. 7, pp. 874–902, Jan. 2000.

[92] T. Belytschko, W. K. Liu, and B. Moran, *Nonlinear Finite Elements for Continua and Structures*. John Wiley & Sons, 2000.

[93] H. Aghamohammadzadeh, R. H. Newton, and K. M. Meek, “X-Ray Scattering Used to Map the Preferred Collagen Orientation in the Human Cornea and Limbus,” *Structure*, vol. 12, no. 2, pp. 249–256, 2004.

[94] T. Mohammad Nejad, C. D. Foster, and D. Gongal, “Finite Element Modeling of Cornea Mechanics: a Review,” *Arq. Bras. Oftalmol.*

[95] R. S. Prather, L. J. Hagemann, and N. L. First, “Preimplantation mammalian aggregation and injection chimeras.,” *Gamete Res.*, vol. 22, no. 2, pp. 233–47, Feb. 1989.

[96] L. Dvorscak and C. F. Marfurt, “Age-related changes in rat corneal epithelial nerve density.,” *Invest. Ophthalmol. Vis. Sci.*, vol. 49, no. 3, pp. 910–6, Mar. 2008.

[97] C. L. Cabrera, L. A. Wagner, M. A. Schork, D. F. Bohrand, and B. E. Cohan, “Intraocular pressure measurement in the conscious rat,” *Acta Ophthalmol. Scand.*, vol. 77, no. 1, pp. 33–36, Feb. 1999.

[98] G. Latour, I. Gusachenko, L. Kowalczuk, I. Lamarre, and M.-C. Schanne-Klein, “In vivo structural imaging of the cornea by polarization-resolved second harmonic microscopy.,” *Biomed. Opt. Express*, vol. 3, no. 1, pp. 1–15, Jan. 2012.

[99] M. J. A. Girard, A. Dahlmann-Noor, S. Rayapureddi, J. A. Bechara, B. M. E. Bertin, H. Jones, J. Albon, P. T. Khaw, and C. R. Ethier, “Quantitative mapping of scleral fiber orientation in normal rat eyes.,” *Invest. Ophthalmol. Vis. Sci.*, vol. 52, no. 13, pp. 9684–93, Dec. 2011.

[100] C. D. Foster, R. I. Borja, and R. A. Regueiro, “Embedded strong discontinuity finite elements for fractured geomaterials with variable friction,” *Int. J. Numer. Methods Eng.*, vol. 72, no. 5, pp. 549–581, Oct. 2007.

[101] C. D. Foster and T. Mohammad Nejad, “Numerical modeling of poromechanics in continuous and localized regions,” in in *Multiscale and Multiphysics Processes in Geomechanics*, Springer, 2011, pp. 141–144.

[102] R. A. Foty and M. S. Steinberg, “The differential adhesion hypothesis: a direct evaluation,” *Dev. Biol.*, vol. 278, no. 1, pp. 255–263, 2005.

[103] C. Wiebe and G. W. Brodland, “Tensile properties of embryonic epithelia measured using a novel instrument,” *J. Biomech.*, vol. 38, no. 10, pp. 2087–2094, 2005.

7 VITA

TALISA MOHAMMAD NEJAD

EDUCATION

UNIVERSITY OF ILLINOIS AT CHICAGO (UIC) Chicago, IL
PhD in Civil Engineering May 2014

SHARIF UNIVERSITY OF TECHNOLOGY (SUT) Tehran, Iran
Bachelor of Science in Civil Engineering July 2009

PUBLICATIONS

- T. Mohammad Nejad, S. Iannaccone, W. Rutherford, P.M. Iannaccone and C.D. Foster. "Mechanics and Spiral Formation in the Rat Cornea." Biomechanics and Modeling in Mechanobiology (Manuscript under review)
- C. D. Foster, T. Mohammad Nejad, "Trilinear Hexahedra with Integral-Averaged Volumes for Nearly Incompressible Nonlinear Deformation", *Finite Elements in Analysis and Design* (Manuscript under review)
- T. Mohammad Nejad, C. D. Foster, D. Gongal, "Finite Element Modeling of Cornea Mechanics: a Review", *ABO*
- J. Rhee, T. Mohammad Nejad, O. Comets, S. Flannery, E. B. Gulsoy, P. Iannaccone, C. D. Foster, "The golden spiral in abduction of mouse corneal behaviors", *Complexity* (Manuscript under review)
- C. D. Foster, T. Mohammad Nejad, "Embedded discontinuity finite element modeling of fluid flow in fractured porous media", *Acta Geotechnica*
- C.D. Foster, T. Mohammad Nejad, "Numerical Modeling of Poromechanics in Continuous and Localized Regions", *Springer Berlin Heidelberg*, 2011
- C. D. Foster, T. Mohammad Nejad, J. Rhee, P. Iannaccone, S. Iannaccone, "Anisotropic finite element modeling of the mouse cornea to investigate spiral pattern in the mouse cornea, 12th U.S. National Congress on Computational Mechanics USNCCM12, 22-25 July 2013, Raleigh, NC
- T. Mohammad Nejad, C. D. Foster, "Three-dimensional FE modeling of the mouse cornea to explain spiraling on epithelium", Engineering Mechanics Institute Conference, 4-7 August 2013, Evanston, IL

HONORS & AWARDS

- Awarded first place in the poster competition in Engineering Mechanics Institute Conference (EMI), August 2013
- Awarded first place in Christopher B. and Susan Burke Civil Engineering graduate Student Award, In Recognition of Exceptional Academic Achievement, April 2013

TEACHING EXPERIENCE

Department of Civil and Materials Engineering, UIC Chicago, IL
Graduate Teaching Assistant (Soil Mechanics) Jan-May 2010, Jan 2013-May 2013
Graduate Teaching Assistant (Finite Element Analysis) Aug-Dec 2012, Aug-Dec 2013

Updated on
September 20, 2013

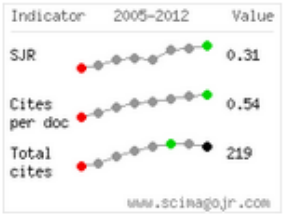

Arquivos Brasileiros de Oftalmologia

Publication of
Conselho Brasileiro de Oftalmologia
Print version ISSN 0004-2749

Mission

To register the scientific output in Ophthalmology, to promote the study, enhancement, and actualization of the professionals of the specialty.

Former Title:

Revista de Oftalmologia de São Paulo

Conselho Brasileiro de Oftalmologia
Rua Casa do Ator, 1117 - cj.21
04546-004 São Paulo SP Brazil
Tel: 55 11 - 3266-4000
Fax: 55 11- 3171-0953
eMail
abo@cbo.com.br